Ions and Electrons Interacting with Ultracold Atoms
-
Novel Approaches Based on Rydberg Excitations

Von der Fakultät Mathematik und Physik der Universität Stuttgart zur Erlangung der Würde eines Doktors der Naturwissenschaften (Dr. rer. nat.) genehmigte Abhandlung.

vorgelegt von

Kathrin Sophie Kleinbach

aus Ludwigsburg

Hauptberichter:	Prof. Dr. Tilman Pfau
Mitberichter:	Prof. Dr. Peter Michler
Mitberichter:	Prof. Dr. Georg Raithel
Prüfungsvorsitzende:	Prof. Dr. Maria Daghofer
Tag der mündlichen Prüfung:	16.07.2018

5. Physikalisches Institut
Universität Stuttgart
2018

List of publications

[1] Kleinbach, K. S., Engel, F., Dieterle, T., Löw, R., Pfau, T. & Meinert, F. "Ionic Impurity in a Bose-Einstein Condensate at Submicrokelvin Temperatures". Phys. Rev. Lett. **120,** 193401 (2018).

[2] Kleinbach, K. S., Meinert, F., Engel, F., Kwon, W. J., Löw, R., Pfau, T. & Raithel, G. "Photoassociation of Trilobite Rydberg Molecules via Resonant Spin-Orbit Coupling". Phys. Rev. Lett. **118,** 223001 (2017).

[3] Liebisch, T. C. *et al.* "Controlling Rydberg atom excitations in dense background gases". J. Phys. B **49,** 182001 (2016).

[4] Schlagmüller, M., Liebisch, T. C., Engel, F., Kleinbach, K. S., Böttcher, F., Hermann, U., Westphal, K. M., Gaj, A., Löw, R., Hofferberth, S., Pfau, T., Pérez-Ríos, J. & Greene, C. H. "Ultracold Chemical Reactions of a Single Rydberg Atom in a Dense Gas". Phys. Rev. X **6,** 031020 (2016).

[5] Böttcher, F., Gaj, A., Westphal, K. M., Schlagmüller, M., Kleinbach, K. S., Löw, R., Liebisch, T. C., Pfau, T. & Hofferberth, S. "Observation of mixed singlet-triplet Rb_2 Rydberg molecules". Phys. Rev. A **93,** 032512 (2016).

[6] Schlagmüller, M., Liebisch, T. C., Nguyen, H., Lochead, G., Engel, F., Böttcher, F., Westphal, K. M., Kleinbach, K. S., Löw, R., Hofferberth, S., Pfau, T., Pérez-Ríos, J. & Greene, C. H. "Probing an Electron Scattering Resonance using Rydberg Molecules within a Dense and Ultracold Gas". Phys. Rev. Lett. **116,** 053001 (2016).

Zusammenfassung

Die Entwicklung der Quantenmechanik im frühen zwanzigsten Jahrhundert war ein Meilenstein in der Physik und begründet das heutige Verständnis der Struktur von Materie. Abgesehen von Max Planck's Untersuchungen der Schwarzkörperstrahlung war die Beobachtung von diskreten Absorptionslinien im Spektrum des Sonnenlichts [7–9] ein wesentlicher Auslöser für die Formulierung der Quantenmechanik. Diese Beobachtung führte zum Bohr-Sommerfeld-Atommodell der quantisierten Energieniveaus von Elektronen im Atom [10, 11], welches eine Abnahme der Bindungsenergie des Elektrons gemäß n^{-2} vorhersagt. Hierbei bezeichnet n die Hauptquantenzahl des elektronischen Zustandes. Bereits dieses einfache Atommodell sagte voraus, dass Elektronen sich in sogenannten Rydberg-Zuständen, nämlich Zuständen mit sehr hoher Hauptquantenzahl befinden können. In Rydberg-Zuständen ist ein Elektron nur schwach an den Atomkern gebunden und der Radius des Elektronenorbits steigt proportional zu n^2. Der Orbit kann damit tausendfach größer sein als im elektronischen Grundzustand. Außerdem besitzt das Rydberg-Atom eine enorme Polarisierbarkeit, welche zu starken Wechselwirkungen zwischen Rydberg-Atomen führt, sowie einer Vielzahl weiterer ungewöhnlicher und extremer Eigenschaften [12].

Diese Eigenschaften machen Rydberg-Atome, insbesondere im Bereich der ultrakalten atomaren Gase, zum Gegenstand aktueller Forschung. In den letzten Jahrzehnten gab es immense Fortschritte auf diesem Gebiet, aufbauend auf der Entwicklung der Laserkühlung [13], die die Herstellung von ultrakalten Wolken bis hin zu Bose-Einstein Kondensaten (BEK) [14] und entarteten Fermi-Gasen [15, 16] ermöglicht. In diesen Experimenten können interne und externe Freiheitsgrade der Atome nahezu perfekt kontrolliert werden. Für solche ultrakalten Wolken wurde vorhergesagt, dass die starken und langreichweitigen Wechselwirkungen zwischen Rydberg-Atomen [12, 17] für Protokolle der Quanteninformationsverarbeitung genutzt werden können [18–20]. Einzelne Quantengatteroperationen wurden bereits experimentell erforscht [21–23]. Die Wechselwirkungen führen zu großen optischen Nichtlinearitäten im Medium, welche genutzt werden können, um das Lichtfeld zu manipulieren [24], was sogar auf dem Einzelphotonenlevel möglich ist [25]. Darüber hinaus, können Rydberg-Rydberg-Wechselwirkungen für die Quantensimulation von Ising-Spinmodellen eingesetzt werden [26]. Deren experimentelle Umsetzung wurde in ein und zwei Dimensionen mit Hilfe von optischen Pinzetten realisiert [27, 28], sowie in optischen Gittern mit Hilfe der Quantengas-Mikroskopie [29]. Atomen im elektronischen Grundzustand kann Rydberg-Charakter beigemischt werden, wodurch sich die ungewöhnlichen Eigenschaften der Rydberg-Atome teilweise auf sie übertragen [30, 31], die Experimente aber auf längeren Zeitskalen durchgeführt werden können. Darüber hinaus können Rydberg-Atome als Quantensensor eingesetzt werden, wie etwa als empfindliche Sonde für elektrische Felder [32]. Des Weiteren dienen Rydberg-Atome der Untersuchung von ultrakalten Plasmen, da die Stoßionisation von Rydberg-Atomen zur Plasmabildung führen kann [33–35].

Alle bisher aufgelisteten Experimente wurden in verdünnten atomaren Gasen durchgeführt. In dieser Doktorarbeit wird hingegen ein System deutlich höherer Dichte behandelt. Genauer gesagt, behandelt sie ein Dichteregime, in dem sich benachbarte Grundzustandsatome bereits innerhalb des Rydberg-Orbits befinden. Je nach Dichte und Größe des Rydberg-Atoms können dies einzelne Atome sein, aber auch Systeme mit zehntausenden Atomen sind möglich. In diesem Regime wechselwirken sowohl das Rydberg-Elektron als auch der ionische Kern mit den Atomen. Beide Aspekte werden in dieser Doktorarbeit thematisiert: Zum ersten Mal konnte die Ion-Atom-Wechselwirkung zwischen dem ionischen Kern des Rydberg-Atoms und neutralen Atomen beobachtet werden. Dieser alternative Ansatz für die Untersuchung von Ion-Atom-Wechselwirkung wurde in einem Temperaturbereich durchgeführt, welcher Größenordnungen niedriger ist als in gewöhnlichen Ion-Atom-Hybridexperimenten, wodurch unser Experiment dem Temperaturlimit für Quanten-Streuexperimente vergleichsweise nahe kommt. Die Elektron-Atom-Wechselwirkung kann zur Bildung von ultralangreichweitigen Rydberg-Molekülen führen und in dieser Arbeit, wurden spezielle Rydberg-Moleküle mit großem elektrischen Dipolmoment untersucht. Um die Resultate mit theoretischen Vorhersagen vergleichen zu können, wurde die Elektron-Atom-Wechselwirkung in einem komplexen Modell berechnet, wobei Spin-Kopplungen für Elektron und Atom berücksichtigt werden.

Die theoretischen Grundlagen für die experimentellen Ergebnisse, die in

Kapitel 5 und 6 behandelt werden, beruhen auf dem Verständnis der Wechselwirkung eines einzelnen Atoms mit einem Rydberg-Atom. Die berechneten Born-Oppenheimer-Potenzialkurven für diese Wechselwirkung sind abstandsabhängig und beinhalten den Beitrag des Rydberg-Elektrons und des ionischen Kerns. Wie in Kapitel 3 ausgeführt, kann die Ion-Atom-Wechselwirkung mit Hilfe eines klassischen Polarisationspotenzials beschrieben werden. Im Gegensatz dazu wird die Elektron-Atom-Wechselwirkung quantenmechanisch behandelt. Es wird eine Kontaktwechselwirkung angenommen [36, 37], wobei sowohl s- als auch p-Wellen-Streuung im Singulett- und Triplett-Streukanal beitragen. Dafür müssen alle relevanten Spin-Freiheitsgrade für das Rydberg-Elektron und das neutrale Atom einbezogen werden. Unter Berücksichtigung dieser Terme können die Wechselwirkungspotenziale numerisch berechnet werden.

Im Jahr 2000 fand C. Greene et al. [36, 37] heraus, dass Molekülzustände in diesen Potenzialen gebunden sein können und sagte damit die Existenz von ultra-langreichweitigen Rydberg-Molekülen im Kontext der dichten ultrakalten Gase voraus. Diese Moleküle sind durch die Elektron-Atom-Streuung des quasi-freien Rydberg-Elektrons mit dem Nachbaratom schwach gebunden. Solche ultra-langreichweitigen Rydberg-Moleküle wurden 2009 erstmal von V. Bendkowsky et al. [38] nachgewiesen, was zahlreiche Forschungsarbeiten zu diesen Molekülen initiierte. Es wurden Arbeiten zu mehratomigen Rydberg-Molekülen durchgeführt [39] bis hin zum Übergang zur Vielteilchenphysik [40]. Außerdem gibt es Untersuchungen des elektrischen Dipolmoment der Rydberg-Moleküle im S-Zustand [41] und der Bildung exotischer Rydberg-Moleküle mit enorm großem elektrischen Dipolmoment [42, 43]. Darüber hinaus wurde die Spin-Kopplung in Rydberg-Molekülen untersucht [44, 45], sowie die Hybridisierung verschiedener Molekülzustände [46]. Mögliche Anwendungen wurden in Form von induzierten Spin-Flips [47] und optischen Feshbach-Resonanzen demonstriert [48].

Eine spezielle Klasse von ultra-langreichweitigen Rydberg-Molekülen, sogenannte Trilobit-Rydberg-Moleküle, bilden sich für (fast) entartete wasserstoffartige Energieniveaus. Sie zeichnen sich durch eine charakteristische Verteilung der Elektronenaufenthaltswahrscheinlichkeit aus, welche durch die konstruktive Interferenz verschiedener Rydberg-Orbitale am Ort des neutralen Atoms geformt wird [36]. Es wird Trilobit-Molekül genannt, da die Form der Elektronenaufenthaltswahrscheinlichkeit der Form eines Trilobit-Fossils ähnelt. Die erhöhte Konzentration der Elektronenaufenthaltswahrscheinlichkeit am Ort des Atoms führt zu einem immensen elektrischen Dipolmoment. Ein elektrisches Dipolmoment in einem homonuklearen Molekül ist höchst ungewöhnlich, da hierfür die Symmetrie zwischen den beiden Atomen gebrochen werden muss. Systeme mit einem elektrischen Dipolmoment sind interessant, da sie stark untereinander wechselwirken und möglicherweise zur Untersuchung dipolarer Störstellen in einem Hintergrundgas genutzt werden können [49, 50]. Des Weiteren könnten Ketten oder Felder solcher polarer Moleküle verwendet werden, um die anisotrope langreichweitige Wechselwirkung für wenige Teilchen oder im Vielteilchensystem zu erforschen [51]. Zustände mit noch höherem elektrischen Dipolmoment werden für den Fall vorhergesagt, dass sich zahlreiche Atome im in der Rydberg-Elektronenwellenfunktion befinden [52]. Die Experimente in dieser Arbeit werden hingegen in einem Dichteregime durchgeführt, für welches sich nur ein (oder wenige) Nachbaratome im Rydberg-Orbit aufhalten. Charakteristisch für Trilobit-Rydberg-Moleküle sind elektronische Zustände mit hoher Drehimpulsquantenzahl L, weswegen sie sich schwer photoassoziieren lassen. Aufgrund der Dipolauswahlregeln kann mit ein- oder zwei-Photonenübergängen nicht an diese Zustände gekoppelt werden. Im Jahr 2015 zeigten D. Booth et al. [42], dass Photoassoziation von Trilobit-Rydberg-Molekülen in Zäsium möglich ist, da für dieses spezielle Element der nicht-ganzzahlige Teil des Quantendefekts so klein ist, dass dem Trilobit-Rydberg-Molekül S-Charakter beigemischt ist.

In dieser Arbeit wird ein allgemeiner Weg aufgezeigt, wie Trilobit-Moleküle verschiedener chemischer Elemente photo-assoziiert werden können. In Kapitel 5 dieser Arbeit, welches auf Quelle [2] basiert, wird diese neue Herangehensweise vorgestellt, die es erlaubt dem Trilobit-Rydberg-Molekül S-Charakter beizumischen. Dafür werden die bereits erwähnten Spin-Kopplungseffekte des Elektron-Atom-Streuprozesses ausgenutzt. Es werden Photoassoziationsspektren präsentiert, aus denen die molekularen Bindungsenergien entnommen werden. Diese werden mit theoretischen Vorhersagen verglichen und das große elektrische Dipolmoment des erzeugten Trilobit-Rydberg-Moleküls von >100 Debye wird bestimmt.

Anschließend wendet sich die Arbeit einem noch höheren Dichteregime zu, für welches sich zahlreiche Atome innerhalb des Rydberg-Orbits befinden. Untersuchungen von Rydberg-Atomen in solch hohen Dichten haben eine lange Tradition: Bereits 1934 publizierten die Arbeitsgruppen E. Amaldi et al. [53] und C. Füchtbauer et al. [54] unabhängig von einander Rydberg-Spektren, die in Dampfzellen aufgenommen wurden, welche mit einem Puffergas befüllt waren. Sie beobachteten sowohl die Verbreiterung als auch die Verschiebung der Spektrallinien. Diese Beobachtungen motivierten E. Fermi eine quantenmechanische Beschreibung des Streuprozesses zu erarbeiten [55], welche auch die Grundlage für das oben beschriebene Modell zur Elektron-Atom-Streuung bildet. Darüberhinaus wird Fermi's Konzept des Pseudopotenzials und der Streulänge heutzutage oft für die Beschreibung der Wechselwirkung zwischen neutralen Atomen, Molekülen, geladenen Teilchen, etc. eingesetzt, solange die Kollisionsenergie niedrig und die genaue Form des Wechselwirkungspotenzials nicht relevant ist.

Im Gegensatz zu Experimenten in heißen Dampfzellen 1934, ermöglichen Experimente in Bose-Einstein-Kondensaten hoher Dichte die Wechselwirkung viel präziser zu erforschen. So konnte etwa die Kopplung des Rydberg-Elektrons an Phononen im Kondensat untersucht werden [56] und der Einfluss der Elektron-Atom p-Wellen-Streuresonanz wurde aufgezeigt [6]. Zudem kann die Wechselwirkung der Rydberg-Störstelle im BEK als ein exotisches Polaron interpretiert werden [49, 57] und sowohl die Lebensdauer der Störstelle als auch durch die Störstelle auftretende ultrakalte chemische Reaktionen untersucht werden [4].

Wird ein Rydberg-Atom in einem BEK angeregt so halten sich, je nach Größe des Rydberg-Atoms, bis zu mehreren zehntausend Atomen im Rydberg-Orbit auf. Üblicherweise tritt die Elektron-Atom-Wechselwirkung als dominanter Prozess auf, sobald sich Atome im Rydberg-Orbit befinden. Der ionische Kern des Rydberg-Atoms wechselwirkt ebenfalls mit den Atomen, was erstmals in dieser Arbeit beobachtet werden konnte. Um den Einfluss der Ion-Atom-Wechselwirkung des Rydberg-Kerns mit dem BEK aufzudecken, muss die typischerweise dominante Elektron-Atom-Wechselwirkung unterdrückt werden. Dafür werden Rydberg-Zustände angeregt, deren Orbitalgröße die Ausdehnung des präparierten Mikro-BEKs übersteigt. Aufgrund des reduzierten Überlapps des Elektronenorbitals mit dem BEK nimmt die Elekton-Atom-Wechselwirkung ab. Gleichzeitig stellt die hohe Dichte im BEK einen kleinen Abstand zum nächsten Nachbaratom sicher, wodurch sich eine signifikante Ion-Atom-Wechselwirkung einstellt. Der Einfluss der Ion-Atom-Wechselwirkung wird durch den Vergleich zwischen der Form der Spektrallinie der Rydberg-Anregung und einem theoretischen Modell deutlich. In diesem Experiment schirmt das Elektron, ähnlich einem Faraday'schen Käfig, externe elektrische Felder effektiv ab, sodass das Ion im BEK nicht von ihnen beschleunigt wird.

Generell ist die Erforschung der Ion-Atom-Wechselwirkung im Regime der Quantenstreuung von großer Relevanz: Die Streueigenschaften können wertvolle Informationen über die Molekülpotenziale liefern und Streuresonanzen könnten die Wechselwirkung regelbar machen [58–60]. Sowohl ultrakalte Quantenchemie [61–64], als auch Störstellenphysik geladener Teilchen [65–67] und Quantensimulation [68–70] könnten erforscht werden. Aufgrund des größeren Massenverhältnisses im Ion-Atom-System im Vergleich zum Elektron-Atom-System werden deutlich niedrigere Temperaturen benötigt, um das Regime der Quantenstreuung zu erreichen. Diese Anforderungen sind aufgrund des anderen Wechselwirkungspotenzials auch strikter als für Atom-Atom-Wechselwirkung. Beispielsweise liegt für die Wechselwirkung eines Rubidium-87 Ions mit einem neutralen Rubidium-87 Atom diese Grenztemperatur bei nur 79 nK. Es wurden bereits Experimente durchgeführt, die einzelne kalte Ionen mit einer kalten atomaren Wolke kombinieren [61, 64, 71, 72], einschließlich Untersuchungen von einzelnen Ionen in einem BEK [73]. In solchen Hybridsystemen wird das Ion in einer Paulfalle gefangen. Diese Experimente sind durch die Mikrobewegung des Ions, verursacht durch die angelegten Wechselfelder der Falle, jedoch typischerweise auf den Millikelvin-Temperaturbereich limitiert [74]. Obwohl das optische Fangen von Ionen kürzlich gezeigt wurde [75, 76], gibt es bislang kein Hybridsystem mit einer optischen Ionenfalle. Somit ist die Erforschung des ionischen Kerns eines Rydberg-Atoms vielversprechend, da das Atom zu Beginn des Experiments auf BEK-Temperatur gekühlt wird. In unseren Experimenten, die in Kapitel 6 (aufbauend auf Quelle [1]) presentiert werden, kann die Ion-Atom-Wechselwirkung bei Submikrokelvin-Temperatur erforscht werden. Dies gilt auch unter Berücksichtigung der Rückstoßenergie durch die Anregung. Die Temperatur, die in diesem Experiment erreicht wird, liegt etwa drei Größenordnung niedriger als in Experimenten mit Paulfallen und nur noch eine Größenordnung über dem Temperaturlimit für quantenmechanische s-Wellen-Streuung in Rubidium-87.

Contents

1

Introduction

The rise of quantum mechanics in the beginning of the 20th century was a milestone in physics as it forms the basis for our today's understanding of the structure of matter. Besides Max Planck's research on the black-body radiation, one of the triggers that led to its development was the detection of discrete absorption lines in the solar spectrum [7–9]. This observation motivated the Bohr-Sommerfeld atomic model of quantized energy levels for electrons in an atom [10, 11], which predicts the electron binding energy to decrease according to n^{-2}. Here, n labels the principal quantum number of the electronic state. Even this simple model predicts that Rydberg states, which are electronic states of very high principal quantum number, can exist. For Rydberg states the electron is loosely bound to the nucleus and the electron orbit radius increases proportional to n^2. It can be thousand fold larger than for the electronic ground state. Additionally, the atom obtains a huge polarizability leading to extraordinary mutual interactions, and a plethora of further remarkable properties [12].

Nowadays, these properties make Rydberg atoms specifically interesting in the context of ultracold atomic gases. In the last decades, enormous progress has been made in this field, triggered by the developement of laser cooling [13], allowing for the preparation of ultracold clouds or even Bose-Einstein condensates (BEC) [14] and degenerate Fermi gases [15, 16]. This enables unprecedented control of the internal and external degrees of freedom of the atoms. When preparing such an environment, the strong and long-range interactions between Rydberg atoms [12, 17] have been proposed to be applicable for quantum information processing protocols [18, 19] (reviewed in Ref. [20]). Single gate operations have been experimentally investigated [21–23]. The interactions also introduce large optical non-linearities in the medium, that can be applied to manipulate the light field [24] even on the single photon level [25]. Moreover, Rydberg-Rydberg interactions can be employed for quantum simulation of Ising spin models [26], which was experimentally realized in one and two dimensions using atoms trapped in optical tweezers [27, 28] or in optical lattices with the help of quantum gas microscopy [29]. Ground state atoms can be dressed with Rydberg-character, inheriting some of the Rydberg state's extraordinary properties [30, 31] and aiming for experiments that reach motional timescales. Moreover, Rydberg atoms can serve as a quantum sensor e.g. a sensitive electric field probe [32]. Additionally, Rydberg atoms serve for the investigation of ultracold plasmas, due to the fact that the collisional ionization of Rydberg atoms can lead to plasma formation [33–35].

All of the experiments listed above are performed in dilute atomic clouds. In this thesis, a different regime of much higher atomic density is investigated. Specifically, we consider a density regime where neighboring atoms are located within the Rydberg orbit. Depending on the density and the size of the Rydberg orbit, one, a few or even up to tenthousand atoms are within the Rydberg atom. In this regime, both the Rydberg electron and the ionic core interact with these atoms. Both aspects are addressed in this work: For the first time, the ion-atom interaction between the Rydberg ionic core and neutral atoms could be observed. This alternative approach to study ion-atom interaction is performed in a temperature regime orders of magnitude lower compared to conventional ion-atom hybrid experiments, bringing our experiment comparatively close to the quantum scattering limit. The electron-atom interaction can lead to the formation of ultralong-range Rydberg molecules and in this thesis a special class of Rydberg molecules with a huge electric dipole moment was investigated. For comparison to theory, the electron-atom interaction was modeled in a sophisticated manner, including spin-couplings between the electron and the atom.

The theoretical description for all conducted experiments presented in chapter 5 and 6 depends on the understanding of the interaction of a single atom with a Rydberg atom. These Born-Oppenheimer potential energy curves are composed of a contribution of the Rydberg electron and a contribution of the ionic core, which both depend on the internuclear separation. As detailed in chapter 3, the ion-atom interaction can be described by a classical polarization potential. In contrast, the electron-neutral interaction is treated quantum mechanically within a pseudopotential approach [36, 37], where both s- and p-wave scattering contribute for the singlet and triplet scattering channel. Therefore, for both the Rydberg electron and the neutral atom relevant spin degrees of freedom have to be considered. Taking all these terms into account, the interaction potentials are calculated numerically.

C. Greene et al. [36, 37] realized in 2000 that such potential energy curves can support bound molecular states and predicted the existence of ultralong-range Rydberg molecules in an ultracold gas. These molecules are weakly bound by electron-atom scattering of the quasi-free Rydberg electron with a neutral neighboring atom residing in the Rydberg orbit. Such ultralong-range Rydberg molecules were first experimentally observed in 2009 by V. Bendkowsky et al. [38] triggering extensive research in this field. This includes the study of polyatomic Rydberg molecules [39] up to the crossover from few- to many-body physics [40], studies on the electric dipole moment of S-type Rydberg molecules [41], the formation of exotic Rydberg molecules with large electric dipole moment [42, 43], investigations on spin couplings in Rydberg molecules [44, 45] as well as hybridization of Rydberg molecular states [46] and the application of Rydberg molecules to induce remote spin flips [47] or optical Feshbach resonances [48].

A special class of ultralong-range Rydberg molecules, so-called Trilobite Rydberg molecules, are formed for (almost) degenerate hydrogenlike energy levels and have a characteristic electron density distribution, which is shaped by constructive interference of different Rydberg orbitals at the position of the neutral atom [36]. It is named Trilobite Rydberg molecule as the shape of its electron orbital resembles the shape of the trilobite fossil. The concentration of the electron probability density at the position of the neutral atom leads to a huge electric dipole moment. An electric dipole moment for a homonuclear molecule is very exceptional, as the symmetry between the two atoms needs to be broken. Since systems with a large electric dipole moment interact strongly with each other they are of great interest and could possibly form dipolar impurities in an ultracold gas [49, 50]. Moreover, chains or arrays of such highly polar molecules could be applied to engineer anisotropic long-range interacting few- to many-body systems [51]. States of even increased electric dipole moment are expected if Trilobite molecules are formed with numerous atoms within the Rydberg electron wavefunction [52]. In this work, a density regime is chosen, where only one or few neighboring atoms are within the Rydberg orbit. Since Trilobite Rydberg molecules are formed by high angular momentum states, photo-association of Trilobite molecules is generally hindered as there is no coupling to high-L Rydberg states by one- or two-photon excitation due to dipole selection rules. This hurdle can be overcome for the specific case of cesium, for which the Trilobite Rydberg molecule potential inherits some S-character due to the small non-integer part of the quantum defect. This allows for photo-association as demonstrated by D. Booth et al. [42] in 2015.

In this thesis, a general pathway to photo-associate Trilobite Rydberg molecules is demonstrated, applicable to many species. Chapter 5, which is based on Ref. [2], presents the novel approach to admix S-character to the Trilobite Born-Oppenheimer potential energy curve. Therefore, we make use of the aforementioned spin-couplings in the electron-atom scattering process. Photo-association spectra are recorded, the molecular binding energies are extracted and compared to theoretical predictions. Additionally, the dipole moment of the created Trilobite Rydberg molecule is determined.

We then turn to a regime of even higher atomic density, for which numerous atoms are within the Rydberg orbit. The study of Rydberg atoms in an environment of such high density has a long history: Already in 1934 both E. Amaldi et al. [53] and C. Füchtbauer et al. [54] independently published Rydberg spectra recorded in a hot atomic vapor cell filled with a buffer gas. They both observed frequency broadenings and line shifts of the Rydberg spectroscopy lines. The observations of this density shift motivated E. Fermi [55] to work out a quantum mechanical description of the scattering process, which forms the basis for the electron-atom scattering model introduced above. Moreover, Fermi's concept of the pseudopotential and the scattering length is widely applied today in physics to describe the interaction between neutral atoms, molecules, charged particles, etc. as long as the collision energies are low and the exact shape of the interaction potential is not relevant. In contrast to the high density experiments in hot vapor cells in 1934, experiments in high density Bose-Einstein condensates allow to investigate the interaction in much more detail. Coupling of the Rydberg electron to phonons in the condensate could be observed [56] and the role of the electron-atom p-wave scattering resonance was revealed [6]. Furthermore, the interaction of the Rydberg impurity with the BEC can be interpreted as an exotic polaron [49, 57] and the impurity lifetime as well as ultracold chemical reactions can be investigated [4].

When a Rydberg atom is excited in a high density BEC, several tenthousands of atoms can be located inside its orbit, depending on the size of the Rydberg atom. The electron-atom interaction is typically the dominant process as soon as neutral atoms are located inside the Rydberg orbit and is investigated in the aforementioned experiments. However, the ionic core of the Rydberg atom interacts with the neutral atoms as well, which is explored for the first time in this thesis. In order to unravel the role of the ion-atom interaction for the Rydberg nucleus in the BEC, the typically dominant electron-atom interaction needs to be suppressed. Therefore, Rydberg states are excited with orbitals exceeding the size of our micro-BEC. Due to the decreased overlap between the electron orbital and the BEC, the electron-atom interaction reduces. At the same time, the high density in the BEC provides a small nearest neighbor spacing, leading to significant ion-atom interaction. The ion-atom interaction can be revealed by comparison of the spectral line shape of the Rydberg excitation to a theoretical model. In this experiment, the electron intrinsically provides an effective shield against external electric fields to prevent acceleration of the ionic core in the BEC.

Generally, the study of ion-atom interaction in the quantum scattering regime is of great interest: The scattering properties can reveal valuable information about the molecular potentials and scattering resonances could make interactions tuneable [58–60]. Ultracold quantum chemistry [61–64] could be studied as well as impurity physics with charged particles [65–67] and quantum simulation [68–70]. Owing to the larger mass ratio in the ion-atom system in comparison to the electron-atom system, considerably colder temperatures are required to enter the quantum scattering regime. These requirements are also much more stringent than for atom-atom interaction, due to the different interaction potential. For example, the temperature limit for the scattering of a Rubidium-87 ion with a Rubidium-87 atom amounts to only 79 nK. Experiments of cold single ions combined with cold atomic clouds have been performed [61, 64, 71, 72], including studies of single ions in a BEC [73]. In such hybrid systems the ion is trapped in a Paul trap. These experiments are typically limited to the millikelvin temperature range owing to the micromotion of the ion in the radiofrequency field of the trap [74]. Although optical trapping of ions has been recently presented [75, 76], there are no hybrid systems with an optical ion trap, yet. The study of the ionic core of a Rydberg atom with neutral atoms is hence promising, as the atom is initially cooled to BEC temperature. In our experiments, presented in chapter 6 of this work (based on Ref. [1]), the ionic core can be studied at submicrokelvin temperature after Rydberg excitation. This even holds when taking the excitation recoil into account. The temperature is about three orders of magnitude lower in comparison to experiments with Paul traps and only one order of magnitude above the s-wave scattering temperature limit for Rubidium-87.

2

Rydberg atoms

When one or several of the valence electrons of an atom are excited into an energetically high-lying electronic state, it is called a Rydberg atom. These Rydberg atoms show remarkable properties such as a large size and high polarizability in comparison to ground-state atoms. In this thesis, Rydberg atoms are studied in an environment where they form molecules with neighboring neutral ground-state atoms or even interact with several thousands of them. In order to understand the behavior and interaction of Rydberg atoms in such a dense background gas, the basic properties of a bare Rydberg atom need to be understood first.

In this chapter properties of Rydberg atoms such as the energy level structure and the Rydberg electron wave function are introduced, forming the basis for the discussion of the behavior in external electric and magnetic fields. Rydberg atoms with one photo-excited Rydberg electron are discussed at the example of Rubidium-87, which is the element studied in our experiments.

2.1 Rydberg electron energy levels

Already at the beginning of the 18th century people studied distinct absorption lines in the spectrum of the sun using prisms. Wollaston reported the first few of these lines in 1802 [7] and in 1814 Fraunhofer started more detailed studies on this topic [8]. In 1868 Ångström published a set of more than 1000 precise and systematic values of absorption lines [9]. After Balmer described the absorption lines of hydrogen [77] for the so-called Balmer-series, in 1890 Rydberg generalized the formula. He calculated the photon frequency ν for the absorption lines according to [78]

$$\nu = R_\infty \left(\frac{1}{n_1^2} - \frac{1}{n_2^2} \right), \tag{2.1}$$

with the fundamental physical constant R_∞ nowadays known as the Rydberg constant. Here, n_1 and n_2 are integer numbers, the interpretation of which was unclear at that time. The value of the Rydberg constant needs to be adapted for every element depending on its nuclear mass.

Niels Bohr invented his atomic theory in 1913, where he assumed that the electron orbits around the core on a circle with the length of the circle being a n-fold multiple of the de-Broglie wavelength $2\pi r = n\lambda_\mathrm{D}$. Assuming this together with the hypothesis that the coulomb force and the centripetal force acting on the electron should be equal, Bohr derived his formula for the electronic energy levels [10]

$$E_n = -R_\mathrm{y} \frac{Z^2}{n^2}, \tag{2.2}$$

with Z being the charge of the ionic core. Interpreting the Rydberg formula 2.1 as the energy difference between two energy levels for $Z = 1$, one finds that the Rydberg constant in energy units (labeled R_y) equals the famous binding energy of about 13.6 eV for the electronic ground state ($n = 1$) of the electron in the hydrogen atom. Changing to the system of atomic units, the energy is given in terms of one Hartree $E_\mathrm{h} = 4.359\,744\,650 \times 10^{-18}\,\mathrm{J} = 2R_\mathrm{y}$ and therefore $R_\mathrm{y} = 1/2$ in atomic units[1]. The energy levels are described by the principal quantum number $n = 1, 2, 3, \ldots$ and for energetically high levels the electrons binding energy decreases proportional to $-1/n^2$ approaching the ionization threshold.

---

[1] From now on, all formulas will be given in atomic units.

A second famous result of Bohr's atomic model is the formula for the electron orbit radius

$$r_n = \frac{n^2}{Z}, \tag{2.3}$$

given in terms of the atomic length scale unit, which is the Bohr radius $a_0 \approx 5 \times 10^{-11}$ m. Already this semi-classical theory predicts that Rydberg atoms have orbits which increase dramatically with n^2. For example, for $n = 140$ the radius exceeds 1 µm!

In order to extend Bohr's atomic model, Sommerfeld later on [11] suggested to allow for elliptic electron orbits and introduced the orbital angular momentum $\hat{L}$ of the electron. Its magnitude is given by the orbital angular momentum quantum number $L = 0, 1..., n$. According to the naming of the observed line spectra one still uses the names $S, P, D, F, ...$ for the $L = 0, 1, 2, 3, ...$ states. Additionally, Sommerfeld introduced the magnetic quantum number $m_L = -L, -(L-1), ..., (L-1), L$ corresponding to the projection of $\hat{L}$ onto a quantization axis. This results in $2L+1$ possible values of m_L. It turned out that Bohr's and Sommerfeld's formulas are correct to first order and the quantum numbers are meaningful in the framework of the full quantum-mechanical description which was developed later on.

However, the simple Bohr-Sommerfeld model didn't include the angular momentum $\hat{S}$ of the electron, which is called its spin, with the absolute value given by the spin quantum number S and the projection m_S along a quantization axis. This spin is connected to the magnetic moment μ_S of the electron. The spin and the orbital angular momentum of the electron couple and the coupled system is best described by the total electronic angular momentum $\hat{J} = \hat{L} + \hat{S}$ of the electron, resulting in quantum numbers J with $|L - S| < J < |L + S|$ and the projection m_J. The energy levels for different J are no longer degenerate, but split by the so-called fine structure splitting

$$\Delta E_{\mathrm{FS}} = a\ \hat{L} \cdot \hat{S}, \tag{2.4}$$

which appears due to the spin-orbit coupling with the coupling constant a. In the same way, the nuclear spin $\hat{I}$ couples with $\hat{J}$ to the total angular momentum $\hat{F} = \hat{I} + \hat{J}$ leading to an energy shift which is to first order given by [79]

$$\Delta E_{\mathrm{HFS}} = A_{\mathrm{HFS}}\ \hat{I} \cdot \hat{J} = \frac{A_{\mathrm{HFS}}}{2}[F(F+1) - I(I+1) - J(J+1)], \tag{2.5}$$

with the hyperfine structure constant A_{HFS} which decreases for larger n as the electron probability at the core decreases. For Rydberg states, the hyperfine interaction can be neglected, as their electron probability density close to the nucleus is small. Therefore, the Rydberg state is well characterized by the quantum numbers n, L, J, m_J.

For atoms other than hydrogen, once there is one electron excited to a Rydberg state it interacts with the remaining ionic core, which in contrast to the hydrogen core contains more than one proton. The nucleus has charge Z, but there are $Z-1$ remaining core electrons shielding its charge. Therefore, the effective charge of the nucleus is close to unity and the hydrogen treatment can be adapted with minor changes. In addition to the small change in the potential, the Rydberg electron slightly polarizes the remaining core electrons anisotropically, depending on L. The largest effect of the core being different to hydrogen is probed by the electronic states of low L whereas the high-L states are almost unperturbed. Therefore, the states with $L < 4$ split off significantly from the hydrogen-like manifold. When atoms are excited from the ground state into a Rydberg state, these low-L states can therefore be addressed separately by narrow-line laser excitation due to their particular splitting. The adapted formula for the energy levels

$$E_{nLJ} = -\frac{Z^2}{2(n-\delta_{nLJ})^2} \tag{2.6}$$

includes the quantum defects δ_{nLJ} which do not only depend on n and L but also on the total electronic angular momentum quantum number J. Remember that $R_{\mathrm{y}} = 1/2$ in atomic units.

One can define

$$n^* = n - \delta_{nLJ}, \tag{2.7}$$

which is called the effective principal quantum number of the electronic state as it inherits the role of the principal quantum number in the Bohr model. As mentioned before, only states with $L < 4$ possess significant quantum defects. The quantum defects can be quantified via tha Rydberg-Ritz formula [80–82]

$$\delta_{nLJ} = \delta_0 + \frac{\delta_2}{(n-\delta_0)^2} + \frac{\delta_4}{(n-\delta_0)^4} + \frac{\delta_6}{(n-\delta_0)^6} + ... \tag{2.8}$$

which is restricted to the first two terms for the calculations in this thesis. Using measured quantum defects for the energy level calculation, the fine-structure coupling is implicitly included.

Throughout this thesis, the values for the energy levels of Rubidium-87 used in calculations are taken from Refs. [79, 83, 84] for energetically low lying states. For the case of energetically higher levels with low L,

	δ_0	δ_2
$n\mathrm{S}_{1/2}$	3.1311807	0.1787
$n\mathrm{P}_{1/2}$	2.6548849	0.29
$n\mathrm{P}_{3/2}$	2.6416737	0.295
$n\mathrm{D}_{3/2}$	1.3480948	-0.6054
$n\mathrm{D}_{5/2}$	1.3464622	-0.594
$n\mathrm{F}_{5/2}$	0.0165192	-0.085
$n\mathrm{F}_{7/2}$	0.0165437	-0.086

Table 2.1: Quantum defects for ^{87}Rubidium [80–82]. The values for Rydberg-Ritz formula are given for the different nL_{m_L} Rydberg states with L up to 3.

Eq. 2.6 was used, with the measured Rydberg constant $R_\mathrm{y}(^{87}\mathrm{Rb}) = h \times 3289.821\,194\,66(2) \times 10^{12}$ Hz from Ref. [80] and the quantum defects given in Tab. 2.1.

For $L > 3$ the solution of the hydrogenic energy levels in Dirac theory is used, expanded in powers of the fine-structure constant α as in [85] and the correction due to the core polarizability is added according to [86], resulting in

$$E_{nLJ} \simeq R_\mathrm{y} \frac{Z^2}{n^2} \left[1 - \frac{Z^2 \alpha^2}{n^2} \left(\frac{3}{4} - \frac{n}{J + 1/2} \right) \right] - \frac{3\alpha_\mathrm{c}}{4n^3 L^5}. \tag{2.9}$$

The core polarizability of Rubidium-87 is $\alpha_\mathrm{c} = 5.9717 \times 10^{16}$ Hz or 9.076 a u [87].

2.2 Rydberg electron wave functions

The Bohr-Sommerfeld model delivers the binding energies E_n of the electronic levels. In order to gain knowledge and calculate further properties of Rydberg atoms, but at the same time get a pictorial understanding of the Rydberg states, in addition to the binding energies, the electronic wave functions $\Psi(\mathbf{r})$ are required. Therefore, the stationary Schrödinger equation

$$\begin{aligned} \hat{H}_0 \Psi(\mathbf{r}) &= (\hat{H}_\mathrm{kin} + \hat{H}_\mathrm{pot}) \Psi(\mathbf{r}) \\ &= \left(-\frac{\nabla^2}{2\mu} + V(r) \right) \Psi(\mathbf{r}) = E \Psi(\mathbf{r}) \end{aligned} \tag{2.10}$$

needs to be solved. In addition to the eigenenergies E_n which equal the values found by Bohr's formula, also the eigenfunctions for the electron at position

r and the ionic core at the origin have to be found. The Hamiltonian for the bare Rydberg atom $\hat{H}_0$ consists of a kinetic energy part $\hat{H}_{\text{kin}}$ and a potential energy part $\hat{H}_{\text{pot}}$, which is in this case the coulomb potential $V(r) = -1/r$ (where $r = |\mathbf{r}|$), centered at the origin, describing the interaction between the Rydberg electron and the ionic core. Here, $\mu = m_1 m_2/(m_1 + m_2)$ is the reduced mass of the two particles of mass m_1 and m_2. The calculation for the case of the hydrogen atom is presented in many textbooks on atomic physics, for example Refs. [85, 88]. For a spherically symmetric potential $V(r)$, it is useful to transform the Schrödinger equation to spherical coordinates

$$\left[-\frac{1}{2\mu r}\frac{d^2}{dr^2}r + \frac{\mathbf{L^2}}{2\mu r^2} + V(r)\right]\Psi(r,\theta,\phi) = E\Psi(r,\theta,\phi). \tag{2.11}$$

As only the angular momentum operator $\mathbf{L}$ acts on the angles θ and ϕ with respect to the quantization axis z, but the rest of the Hamiltonian only depends on r, the solutions for $\Psi(r,\theta,\phi)$ have to be eigenfunctions for $\mathbf{L^2}$ and L_z (which is the z-component of $\mathbf{L}$) as well. The fact, that $\mathbf{H}, \mathbf{L^2}$ and L_z have the same eigenfunctions is also manifested by their pairwise commutators all being zero. Laplace's spherical harmonics

$$Y_L^{m_L}(\theta,\phi) = \frac{1}{\sqrt{2\pi}}\sqrt{\frac{(2L+1)}{2}\frac{(L-m_L)!}{(L+m_L)!}}P_L^{m_L}(\cos\theta)e^{im_L\phi}, \tag{2.12}$$

with the associated Legendre polynomials $P_L^{m_L}$ are in fact eigenfunctions to the two operators $\mathbf{L^2}$ and L_z. Therefore, the solution for $\Psi(r,\theta,\phi)$ can be found by a separation ansatz

$$\Psi(\mathbf{r}) = \mathcal{R}(r)Y_L^{m_L}(\theta,\phi), \tag{2.13}$$

of a radial part $\mathcal{R}(r)$, which only depends on the separation r between the electron and the ionic core, and the angular part $Y_L^{m_L}(\theta,\phi)$.

When adapting this method for the hydrogen atom to alkali atoms, the angular part is unchanged and is still described by Laplace's spherical harmonics. In contrast, in order to find the radial part of $\Psi(\mathbf{r})$ for alkali atoms the potential needs to be modified to account for additional core electrons. The radial part of the Schrödinger equation reads

$$\left[-\frac{1}{2r}\frac{d^2}{dr^2}r + \frac{L(L+1)}{2r^2} + V_{\text{mod}}\right]\mathcal{R}(r) = ER(r) \tag{2.14}$$

and contains the centrifugal term plus the modified ion-electron interaction potential. The reduced mass drops out as $\mu \approx m_e$ which is 1 in atomic units.

For the modified ion-electron potential

$$V_{\mathrm{mod}}(r) = -\frac{Z_{\mathrm{eff}}(r)}{r} + V_{\mathrm{pol}} + V_{\mathrm{so}} \tag{2.15}$$

is used. The effective charge $Z_{\mathrm{eff}}(r)$ is described by

$$Z_{\mathrm{eff}}(r) = 1 + (z-1)e^{-a_1 r} - r(a_3 + a_4 r)e^{-a_2 r} \tag{2.16}$$

according to Ref. [87] with the a_i coefficients given therein. In addition to this effective charge of the ionic core, also the polarizability of the core is taken into account. The core gets polarizable due to the electrons in closed shells and contribution is [87]

$$V_{\mathrm{pol}} = -\frac{\alpha_{\mathrm{c}}}{2r^4}\left(1 - e^{(r/r_{\mathrm{c}})^6}\right) \tag{2.17}$$

where r_{c} is a cutoff radius as the polarizability of the inner electrons should play no role very close to the nucleus. The third part of equation 2.15 is the spin-orbit term which can be approximated by [89]

$$V_{\mathrm{so}} \simeq \frac{\alpha^2}{4r^3}\left(J(J+1) - L(L+1) - S(S+1)\right). \tag{2.18}$$

The radial part $\mathcal{R}(r)$ of the wave function is then calculated by solving the Schrödinger equation using the Numerov method on a quadratically scaled grid for r. The corresponding Numerov equation can be found in [86]. As the effective potential equation 2.15 is not very precise for small values of r, the radial starting point is chosen to be either $\sqrt[3]{\alpha_{\mathrm{c}}}$ or the classical inner turning point of the electron (especially for large L) depending on what is larger.

An exemplary result of this numerical calculation is presented in Fig. 2.1 for $n = 25$, where the absolute value of the weighted radial wave function is depicted. One can see, that the number of nodes in the wave function decreases by one for an increase in L by one. Additionally, the radial position of the outer most peak shifts to lower r the larger the angular momentum of the Rydberg state. The orbit size of a Rydberg S-state is therefore about twice (up to the non-integer part of the quantum defect) as large compared to the Rydberg state with maximum L. The peak position of the maximum-L orbit fits the Rydberg orbit size predicted by Bohr's model $r_{25} = 625\,\mathrm{a}_0$ (see Eq. 2.3). Furthermore, for increasing n by one and keeping $L = 0$ the number of nodes in the wave function increases by one as well.

To sum up, the electronic wave functions $\Psi(\mathbf{r}) = \mathcal{R}(r)Y_L^{m_L}(\theta,\phi)$ for the Rydberg electron are calculated by numerically solving the radial part of the

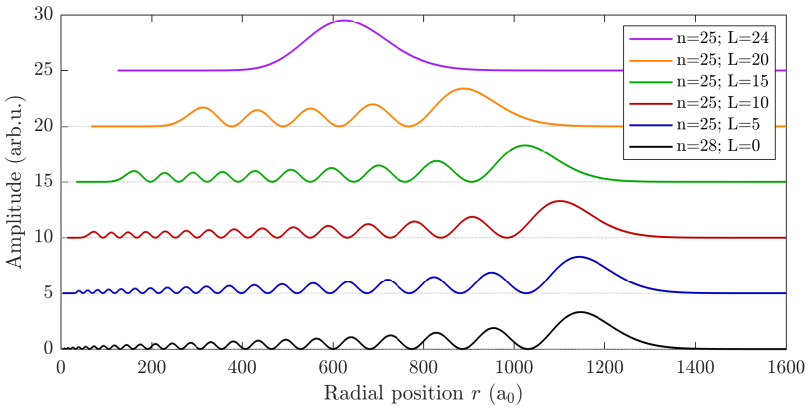

Fig. 2.1: Radial Rydberg wave functions as a function of the radial position r of the Rydberg electron. For $n = 25$ the absolute value of the weighted radial wave functions are shown for $L = 24, 20, 15, 10, 5$ and $m_J = L + 1/2$ corresponding to the curves in purple, orange, green, red, and blue. The radial wave function marked in black is calculated for $n = 28$, $L = 0\, m_L = 0.5$ which is the Rydberg S-state energetically closest to the $n = 25$ hydrogenic manifold. The curves are offset for better readability.

Schrödinger equation using an adapted ion-neutral interaction potential for alkali atoms in order to find the radial part $\mathcal{R}(r)$ of the wave function. The angular part $Y_L^{m_L}(\theta, \phi)$ is calculated analytically according to the Laplace spherical harmonic functions.

2.3 Rydberg atoms in static external fields

In this chapter the response of Rydberg atoms to external electric and magnetic fields is discussed. The Rydberg electron shows increased sensitivity to external electric fields for increasing n, magnitudes stronger than for deeply bound electrons. In contrast, the behavior in external magnetic fields can be treated analogously to ground state atoms in most cases. Merely, for very high n diamagnetic line shifts can start to play a role even at moderate field strength.

2.3.1 External electric fields

In contrast to deeply bound electrons, Rydberg electrons are located further away from the ionic core and are thus much more sensitive to external electric fields. Therefore, it is important to understand their response to electric fields as the controlled application of electric fields on field electrodes is a powerful tool to manipulate Rydberg atoms in a controlled fashion. Additionally, undesired influences by detrimental stray electric fields need to be understood in order to compensate such fields efficiently.

An atom placed in a static external electric field $\boldsymbol{\mathcal{E}}$ interacts with it according to

$$\hat{H}_{\mathcal{E}} = -\mathbf{d}\boldsymbol{\mathcal{E}}, \tag{2.19}$$

with the dipole operator $\mathbf{d}$ which is given in terms of the atomic unit electric dipole moment $ea_0 \approx 8.5 \times 10^{-30}\,\mathrm{Cm} \approx 2.54\,\mathrm{D}$ with the electron charge e. The atomic unit for the electric field $\boldsymbol{\mathcal{E}}$ is $e/(4\pi\varepsilon_0 a_0^2) \approx 5.1 \times 10^{11}\,\mathrm{V/m}$ with the dielectric constant ε_0.

In order to calculate the Stark shift caused by the static electric field, the level coupling due to the electric field

$$\left\langle \Psi_{nLm_L} \right| \mathbf{d}\boldsymbol{\mathcal{E}} \left| \Psi_{n'L'm'_L} \right\rangle \tag{2.20}$$

needs to be evaluated. In practical this is done for a truncated basis set including a state of interest and all states of a few neighboring principal quantum numbers, as those couple the strongest. The matrix $\hat{H}_0 + \hat{H}_{\mathcal{E}}$ is set up in this basis for each value of $\mathcal{E}$ and its full diagonalization delivers the new eigenenergies for the Rydberg states in the presence of the external electric field. The result of such a full diagonalization is presented in Fig. 2.2(a), where the Rydberg levels in the vicinity of the 71S state are shown as a function of applied external electric field. The Rydberg levels in the hydrogenic manifolds 68m and 69m show a linear Stark shift due to level mixing. However, if the level shift caused by the electric field is small with respect to the level spacing between neighboring levels, level mixing can be neglected and one can treat the problem perturbatively. This is typically the case for low-L Rydberg states of alkali atoms which are well isolated by their respective quantum defects.

In perturbation theory one finds

$$\Delta E_{\mathcal{E}} = -(d_0\mathcal{E}_z + \frac{\alpha}{2}\mathcal{E}_z^2 + O(\mathcal{E}^3)) \tag{2.21}$$

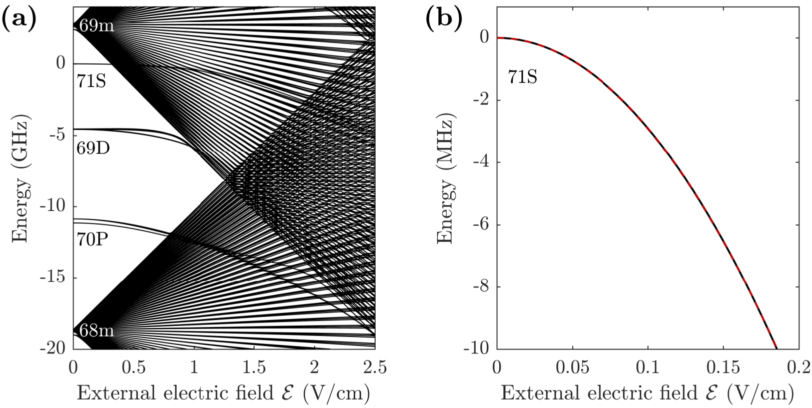

Fig. 2.2: Rydberg levels in an external electric field. (a) Overview of the Rydberg levels in the vicinity of the 71S state as a function of external electric field $\mathcal{E}$. Low-L states are explicitly labeled. The hydrogenic manifolds are referred to as m. (b) Zoom-in on the 71S state for low electric field values. The outcome of the full diagonalization (black solid) and the quadratic fit (red dashed) fall on top.

for an electric field along z. Here, d_0 is the dipole moment of the unperturbed Rydberg state which is zero as the dipole operator only couples states of opposite parity. Therefore, only the second order contributes and causes a quadratic Stark shift with the scalar polarizability α, which is

$$\alpha = \sum_{nL \neq n'L'} \frac{|\langle \Psi_{nL}| \, z \, |\Psi_{n'L'}\rangle|^2}{E_{nL} - E_{n'L'}}. \tag{2.22}$$

The polarizability α increases proportional to n^7 as larger Rydberg states are easier to polarize. This gets evident, considering that the relative spacing of the energy levels decreases $(E_{nL} - E_{n'L'}) \propto n^{-3}$ and the coupling raises $\langle \Psi_{nL}| \, z \, |\Psi_{n'L'}\rangle \propto n^2$. The quadratic behavior with respect to $\mathcal{E}$ can be seen in Fig. 2.2(b) where the energy of the 71S state is shown as a function of the external electric field in a range, for which the line shift is small in comparison to the spacing to neighboring energy levels. The quadratic fit for the perturbative treatment (red dashed) perfectly follows the outcome of the full diagonalization (black solid), which confirms that the perturbative treatment is valid.

If strong electric fields are applied, the Rydberg atom will be ionized. However, before ionization takes place the Rydberg state crosses many other states in the Stark map, coupling to some of them. Therefore, not only the binding energy of the Rydberg state is relevant to determine the ionization threshold voltage, but the ramp speed will influence whether Landau-Zener crossings in the Stark map will be crossed adiabatically or diabatically. For low-m states there are many states of the same m-value energetically closeby and once the state crosses the neighboring hydrogenic manifold, the ionization process is mostly adiabatic such that ionization takes place close to the semi-classical ionization threshold $\mathcal{E} = 1/(16n^4)$. In contrast, high-m states tend cross the neighboring hydrogenic manifold diabatically and follow the Stark states of the hydrogenic manifold, leading to an ionization threshold larger by a factor of two to four [86]. This difference ionization behavior is exploited in state-selective field-ionization experiments: Electric fields are ramped on such that low-m states ionize earlier than high-m states and the ions can be assigned to the two cases due to their arrival time on an ion detector.

2.3.2 External magnetic fields

The interaction of Rydberg atoms with external magnetic fields can not be neglected in most experiments, as typically a magnetic offset field is applied setting the quantization axis in the lab. In our experimental setup, the atoms are even held in a magnetic trap such that Rydberg atoms will always experience a magnetic field.

In order to calculate the level energy shift for a Rydberg electron in an external magnetic field, one starts with the generalized momentum $(\mathbf{p} + \mathbf{A})$ with the magnetic vector potential $\mathbf{B} = \nabla \times \mathbf{A}$. When choosing the symmetric gauge $\mathbf{A} = -(\mathbf{r} \times \mathbf{B})/2$ one can insert this term in the kinetic energy part of the Hamiltonian in Eq. 2.10

$$\begin{aligned}\hat{H}_{\text{kin}} &= \frac{1}{2}\left(\mathbf{p} - \frac{\mathbf{r} \times \mathbf{B}}{2}\right)^2 \\ &= \frac{\mathbf{p}^2}{2} - \frac{1}{2}\mathbf{p}(\mathbf{r} \times \mathbf{B}) + \frac{1}{8}(\mathbf{r} \times \mathbf{B})^2 \\ &= \frac{\mathbf{p}^2}{2} + \frac{\mu_z B_z}{2} + \frac{B_z^2}{8}(x^2 + y^2), \end{aligned} \tag{2.23}$$

where the last line is valid for B oriented along the z-axis. The first term is the standard kinetic energy term, the second term is the linear Zeeman term with the magnetic moment μ_z of the electron and the third term describes diamagnetism. The atomic unit for the magnetic field is $\hbar/(ea_0^2) \approx 2.35 \times 10^5\,\mathrm{T} = 2.35 \times 10^9\,\mathrm{G}$.

In general the full Hamiltonian needs to be diagonalized, but for low magnetic fields in first order only the linear Zeeman term is contributing. The magnetic moment μ_z then comprises both the magnetic moment associated with the charged electron possessing an angular momentum and the magnetic spin moments of the electron and the nucleus. In total the energy shift is given by

$$\Delta E_{\text{Zeeman}} = g \cdot m \cdot B_z \tag{2.24}$$

where the m quantum number corresponds to the projection of the total spin (including both angular momentum, electron spin, and nuclear spin) onto the z-axis and g the corresponding Landé-factor weighting the spin contribution to the magnetic moment. For Rydberg atoms $m = m_J$ as the coupling to the nuclear spin is weak and the state can be described in the J-basis. For the case of low-L states, including the electronic ground state, the total spin projection is given by $m = m_F$. The respective Landé-factors are [79]

$$\begin{aligned} g_J &\approx 1 + \frac{J(J+1) + S(S+1) - L(L+1)}{2J(J+1)} \\ g_F &\approx g_J \frac{F(F+1) - I(I+1) + J(J+1)}{2F(F+1)}. \end{aligned} \tag{2.25}$$

The diamagnetic term is typically much weaker than the linear Zeeman term. For isolated states, such as S-states in Rubidium, no full diagonalization is needed, but the diamagnetic shift is

$$\Delta E_{\text{dia}} = \frac{B_z^2}{8} \left\langle \Psi_{nLm_L} \right| r^2 \sin(\theta) \left| \Psi_{nLm_L} \right\rangle, \tag{2.26}$$

with the angle θ between the electron position $\mathbf{r}$ and the z-axis [86]. It scales as n^4 and therefore, the relative strength of ΔE_{dia} compared to ΔE_{Zeeman} gets significant, as soon as $n^4 B > 1$.

This can be seen in Fig. 2.3, where both the linear Zeeman term and the diamagnetic term are presented for a set of $\left| n\mathrm{S}_{1/2}, m_J = 1/2 \right\rangle$ Rydberg states. While for low principal quantum numbers such as $n = 50$ the regime where both terms get comparable is entered for magnetic fields strength in the range of 1000 G, in contrast, for $n = 200$ already magnetic fields of $B = 3\,\mathrm{G}$ are strong enough. Megahertz line shifts due to the diamagnetic effect can be measured at even lower fields.

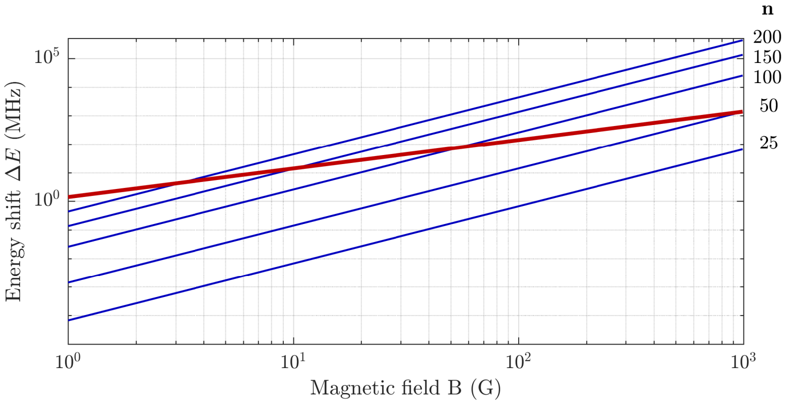

Fig. 2.3: Line shift ΔE for nS Rydberg states due to the linear Zeeman term and the diamagnetic term as a function of magnetic field B. The linear Zeeman shift of a $\left|n\mathrm{S}_{1/2}, m_J = 1/2\right\rangle$ state is independent of the principal quantum number n and marked as a red line. In contrast the diamagnetic line shift for the $\left|n\mathrm{S}_{1/2}, m_J = 1/2\right\rangle$ states (as labeled on the right) is getting stronger for increasing n.

2.4 Rydberg-Rydberg interaction

One main reason for the great interest in Rydberg physics during the last years stems from the fact, that strong long-range interactions arise between Rydberg atoms [12, 17–20, 26, 28, 90]. By exciting and deexciting atoms to a Rydberg state, these interactions between neutral atoms can be turned on and off. Therefore, a brief introduction to Rydberg-Rydberg interaction will be given here, despite the fact that the work in this thesis is in the regime, where only one Rydberg atom is excited in the whole sample.

If two Rydberg atoms approach each other they interact with each other according to the dipole-dipole interaction potential

$$V_{\mathrm{dd}}(R) = \frac{\mathbf{d}_1\mathbf{d}_2 - 3(\mathbf{R}\cdot\mathbf{d}_1)(\mathbf{R}\cdot\mathbf{d}_2)}{R^3} \tag{2.27}$$

with their respective dipole moments $\mathbf{d}_i$ and the distance $\mathbf{R}$ between the two atoms.

Rydberg atoms in nS states as treated in this thesis don't possess a permanent electric dipole moment. However, Rydberg atoms are very polarizable and an electric dipole moment can be induced. Hence, when two nS Rydberg atoms approach each other they interact with each other via induced dipole-dipole interaction given by the van-der-Waals potential

$$V_{\mathrm{vdW}} = \frac{C_6}{R^6} \tag{2.28}$$

which is characterized by the C_6 coefficient that typically scales as n^{11} [91]. When one Rydberg atom is photo-excited, the Rydberg energy levels of a neighboring atom are shifted due to this van-der-Waals interaction. If the shift is larger than the laser excitation bandwidth γ_{L} (which is typically larger than the natural linewidth of the Rydberg level), the neighboring atoms can not be excited to a Rydberg state. This is called the Rydberg blockade effect and is characterized by the blockade radius

$$r_{\mathrm{B}} = \sqrt[6]{\frac{C_6}{\hbar\gamma_{\mathrm{L}}}} \tag{2.29}$$

which increases proportional to $n^{11/6}$. For Rydberg states with $L \neq 0$ the blockade gets unisotropic. Many Rydberg experiments apply this blockade effect, for example for quantum information processing [18–20] and quantum simulation [26–28] or to introduce large optical non-linearities in the medium [24, 25].

In contrast to this isolated treatment of nS Rydberg states, in general the van-der-Waals interaction needs to be compared to the energy gap between the Rydberg pair state under consideration and neighboring Rydberg pair states [20, 92]. If the van-der-Waals term is large in comparison to this energy spacing, level mixing leads to electric dipole moments and therefore resonant dipole-dipole interactions arise. This is the case for high-L Rydberg states due to nearly degenerate states of the hydrogenic manifold. Furthermore, this crossover to dipole-dipole interaction also occurs for the case of Förster resonances for low-L Rydberg pair states as the level spacing is small. Moreover, it occurs for Rydberg atoms coming extremely close, as the van-der-Waals term gets very large [20, 92].

3

Rydberg atoms in dense media

When Rydberg atoms are immersed in a high density environment, neighboring atoms can be found within the Rydberg orbit. The Rydberg atom will interact with these neutral atoms via electron-neutral and ion-atom interaction. In most cases, the elastic electron-neutral scattering is the dominant term and can lead to the formation of ultralong-range Rydberg molecules. The potential energy curves supporting this molecular bound states emerge from electron-neutral and ion-atom scattering as presented in this chapter. The ion-atom interaction is described by a classical polarization potential. For the electron-neutral interaction between the Rydberg electron and a neutral atom not only quantum mechanical s- and p-wave scattering needs to be considered, but additionally the relative spin orientation of the Rydberg electron and the neutral atom is modifying the scattering process.

3.1 Introduction to quantum mechanical scattering in a spherically symmetric potential

For both the interaction of the Rydberg atom with a neutral atom the theory of the quantum mechanical scattering of two particles has to be applied. It is studied in many textbooks and the introduction here is based on Refs. [88, 93, 94]. For the scattering of two particles, the particles are treated as point-like objects and the problem is formulated in the center of mass frame with the reduced mass $\mu = m_1 m_2/(m_1 + m_2)$. The scattering process is described by the stationary Schrödinger equation for the scattering wave function $\Psi(R)$

$$\left[-\frac{\nabla^2}{2\mu} + V(R)\right]\Psi(\mathbf{R}) = E\Psi(\mathbf{R}) \tag{3.1}$$

for one particle with reduced mass μ and the potential $V(R)$ which is centered around the origin. Here, R denotes the interparticle distance. The collision energy is given by $E = k^2/(2\mu)$ with $k = |\mathbf{k}|$ being the absolute value of the relative wave vector between the two particles.

Typically, the ansatz

$$\lim_{R\to\infty} \Psi(\mathbf{R}) = e^{ikz} + f(E,\theta,\phi)\frac{e^{ikz}}{R} \tag{3.2}$$

is chosen, taking care of the boundary conditions of an “incoming” plane wave e^{ikz} and an “outgoing” spherical wave e^{ikz}/R scaled by the scattering amplitude $f(E,\theta,\phi)$, which depends on the polar angles θ and ϕ with respect to the z-axis. For the rotationally symmetric potential $V(R)$ it is sensible to treat the Schrödinger equation in spherical coordinates analogous to Eq. 2.11 for the calculation of the wave functions in the case of the Coulomb potential. However, the boundary condition of the incoming plane wave along the z-axis poses the requirement, that $m_l = 0$ due to symmetry reasons. This leads to the situation, in which only spherical harmonics

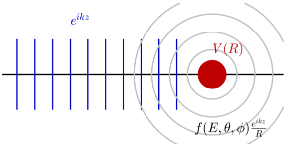

Fig. 3.1: Sketch of the scattering process at the potential $V(R)$ (red). The contributions of an “incoming” plane wave (blue) and a scattered “outgoing” spherical wave (gray) are illustrated.

$$Y_l^{m_l=0}(\theta,\phi) = \frac{1}{\sqrt{2\pi}}\sqrt{\frac{2l+1}{2}}P_l^0(\cos\theta), \tag{3.3}$$

contribute, which are proportional to the associated Legendre polynomials $P_l^0(\cos\theta)$. Therefore, the ansatz for the wave function is

$$\Psi(R,\theta) = \sum_{l=0}^{\infty} \mathcal{R}_{kl}(R) P_l(cos\theta). \tag{3.4}$$

In order to differentiate between the angular momentum in the scattering process, a lowercase l is used, while L is the label for the angular momentum of the electron in the potential of the nucleus. The contributions to the scattering problem for the different l-values are called partial waves and are denoted by s,p,d,... for $l = 0, 1, 2, ...$. Their respective radial wave functions are given by $\mathcal{R}_{kl}(R)$.

When this ansatz is used, every summand of Eq. 3.4 has to fulfill the Schrödinger equation, resulting in radial equations

$$\left[-\frac{1}{2\mu R}\frac{d^2}{dR^2}R + \frac{l(l+1)}{2\mu R^2} + V(R)\right]\mathcal{R}_{kl}(R) = E\mathcal{R}_{kl}(R). \tag{3.5}$$

for each value of l.

For the radial problem one can interpret the second an third term together as an effective potential

$$V_{\text{eff}} = \frac{l(l+1)}{2\mu R^2} + V(R), \tag{3.6}$$

thus consisting of the centrifugal barrier $l(l+1)/(2\mu R^2)$ and the interaction potential $V(R)$. While the centrifugal term is repulsive, in many cases the potential $V(R)$ of interest is attractive, such that the two terms compete depending on the interparticle separation R. The height of the centrifugal barrier rises for increasing l and more and more kinetic energy in the scattering process is required to overcome the barrier. Therefore, only a limited number of partial waves contribute for an experiment with given kinetic energy and the series in Eq. 3.4 can be truncated. For s-wave scattering ($l = 0$), the centrifugal term vanishes and we regain the potential $V(R)$. Typically, experiments aim to reach low temperatures to study quantum scattering, with only the s-wave term contributing to the scattering problem.

Many interaction potentials commonly studied for example dipole-dipole interaction, ion-atom interaction and van-der-Waals interaction follow power laws and can be written as $V(R) = C_n/R^n$. For such potentials, the effective range R^* and the characteristic energy E^* of the potential are given by [95]

$$\begin{aligned} R^* =& (2\mu C_n)^{1/(n-2)} \\ E^* =& \frac{1}{2\mu {R^*}^2}. \end{aligned} \tag{3.7}$$

At R^*, the kinetic energy equals the depth of the scattering potential. R^* and E^* correspond to the position and height of the p-wave barrier, respectively. Typically, for $R < R^*$ one assumes, that the C_n-potential is the dominant term and neglects the kinetic energy, whereas for $R > R^*$ the scattering potential can be neglected, leading to the Schrödinger equation for the free particle.

Therefore, in the limit of $R \to \infty$, where the potential can be neglected, the radial part follows

$$\mathcal{R}_{kl}(R) \sim \sin(kR - l\frac{\pi}{2} + \delta_l(k)). \tag{3.8}$$

with a phase shift $\delta_l(k)$ [88, 94]. As mentioned before, the series in Eq. 3.4 can be truncated, as only a limited number of partial waves contributes significantly to the scattering problem. In the case, where only s-wave scattering is relevant, the full information of the scattering process can be condensed into the scattering phase shift δ_0 for large interparticle separations R.

For completeness, the scattering amplitude f and cross section σ are stated, given by

$$\begin{aligned} f(E,\theta,\phi) =& \sum_{l=0}^{\infty}(2l+1)f_l(k)P_l(cos\theta) \\ \sigma =& \sum_{l=0}^{\infty}\frac{4\pi}{k^2}(2l+1)\sin^2(\delta_l(k)) \end{aligned} \tag{3.9}$$

as derived in many textbooks. The scattering amplitude f_l for the l^{th} partial wave is

$$f_l(k) = \frac{e^{i\delta_l(k)}\sin(\delta_l(k))}{k}, \tag{3.10}$$

which again depends solely on the kinetic energy and the scattering respective phase shift.

3.2 Ion-atom scattering

When a neutral atom resides inside the Rydberg orbit and approaches its ionic core it gets polarized by the ion. The interaction is described by the polarization potential

$$V_{\mathrm{i}}(R) = -\frac{\alpha_{Rb}}{2}\mathcal{E}_{\mathrm{i}}^2. \tag{3.11}$$

Here, α_{Rb} is the ground-state polarizability of the neutral ^{87}Rb atom which is $\alpha_{\mathrm{Rb}} = 2 \cdot C_4 = 318.8\,\mathrm{a.u.} = 5.256 \times 10^{-39}\,\mathrm{C^2m^2/J}$ [96][1]. The electric field of the ion is $\mathcal{E}_{\mathrm{i}} = 1/R^2$ given by the Coulomb law at the internuclear distance R between the neutral atom and the ion. Therefore, the polarization potential is given by

$$V_{\mathrm{i}}(R) = -\frac{C_4}{R^4}, \tag{3.12}$$

denoted from now on as the C_4-potential. The effective range of this scattering potential for the collision of a $^{87}\mathrm{Rb}^+$ ion and a ^{87}Rb neutral atom (and therefore $\mu = 0.5 \times m(^{87}\mathrm{Rb})$) is $R^* = \sqrt{2\mu C_4} \approx 5025\,\mathrm{a_0}$ and the characteristic energy $E^* \approx 6.8 \times 10^{-12}\,\mathrm{eV} = 78.9\,\mathrm{nK}$. Inserting the C_4-potential into Eq. 3.6, we end up with the effective potential

$$V_{\mathrm{eff,i}}(R) = \frac{l(l+1)}{2\mu R^2} - \frac{C_4}{R^4} \tag{3.13}$$

for the set of partial waves l. The spacial dependence of the potentials for the lowest partial waves are presented in Fig. 3.2. For $l = 0$ the potential is purely attractive, whereas for higher partial waves a centrifugal barrier appears. The height of the centrifugal barriers are listed in Table 3.1. One can extract from this table, that temperatures below 78.9 nK have to be reached, to be in the s-wave scattering regime. Such cold temperatures for ion-atom scattering have not been experimentally reached up to now.

partial wave	$l = 1$	$l = 2$	$l = 3$	$l = 4$
centrifugal barrier	78.9 nK	710 nK	2.84 µK	7.89 µK

Table 3.1: Centrifugal barrier heights for ion-atom scattering in ^{87}Rb.

In order to measure a sizable effect of the ion-atom interaction in a Rydberg experiment, an energy contribution in the MHz range should be aimed at.

---

[1] Note that often $C_4 = \alpha$ without the factor of two [1, 65], but in general C_n type potentials are defined as $V = C_n/R^n$

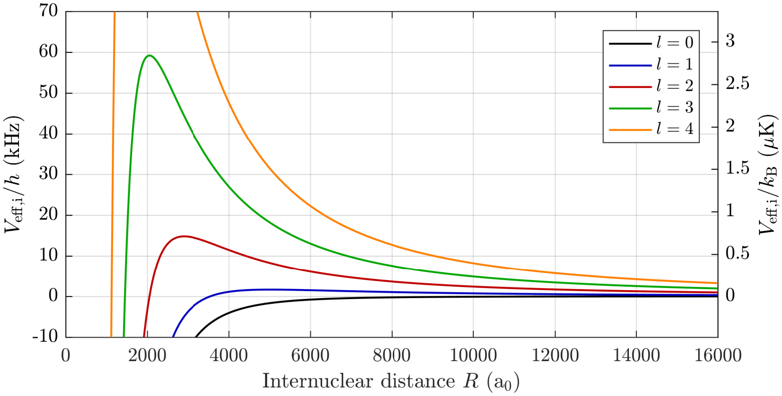

Fig. 3.2: Effective ion-atom scattering potential for partial waves up to $l = 4$. The behavior of the C_4 potential including the centrifugal term is presented as a function of the internuclear distance R in terms of energy (left axis) and temperature (right axis). The extracted centrifugal barrier heights are listed in Table 3.1.

However, for typical experiments with clouds of ultracold rubidium, the sample is dilute and the atoms only probe the outer part of the C_4-potential at kHz depth. In order to reach a regime, where the ion-atom interaction exceeds 1 MHz, the particles have to be as close as $1000\,a_0$. The density of the cloud needs to be increased to at least $1 \times 10^{15}\,\mathrm{cm}^{-3}$ to reach this nearest neighbor spacing of $1000\,a_0$. Only then, a line shift in the MHz range is expected on the Rydberg spectrum.

For very short internuclear distances $R \ll 100\,a_0$ the particles repel each other, such that the pure C_4-potential is insufficiently describing the scattering potential. If one is interested in this short-range behavior model potentials including short-range physics have to be applied [97].

3.3 Electron-atom scattering

Not only the ionic core of the Rydberg atom, but also the Rydberg electron interacts with neutral atoms residing within the Rydberg orbit. In fact, the electron-atom interaction term is much more relevant in many cases, as it starts to play a role as soon as the neutral atom enters the Rydberg orbit, whereas the ion-atom interaction is only dominant for $R << 1000\,a_0$.

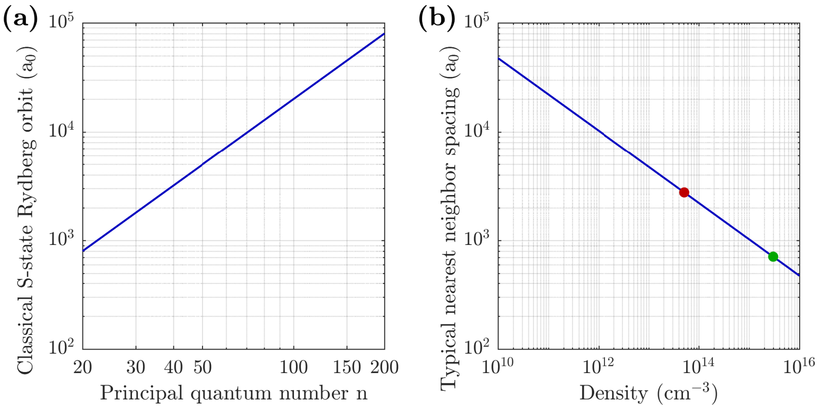

Fig. 3.3: Size of the classical Rydberg orbit and typical nearest neighbor spacing for comparison. (a) The classical size of an Rydberg S-orbit is presented as a function of principal quantum number n. (b) The peak position of the nearest neighbor distribution is shown vs the density. The density of the ultracold sample we use for the Trilobite Rydberg molecule experiment in chapter 5 is marked by the red symbol, while the density in the micro-BEC used for the investigation of the ionic impurity in the BEC (chapter 6 is marked by the green symbol.

Therefore, at as soon as the sample density is so high that the interparticle separation is on the order of the size of the Rydberg orbit, elastic electron-atom scattering is of significant strength and can lead to the formation of ultra long-range Rydberg molecules.

In order to compare the length scale of the Rydberg orbit to the typical spacing of nearest neighbors in an ultracold sample, Fig. 3.3 presents both. In Fig. 3.3(a) the classical size of the Rydberg S-orbit is presented as a function of principal quantum number n. It ranges from 800 a_0 for $n = 20$ to 80 000 a_0 for $n = 200$. The densities needed to typically find one perturber at this distance from the Rydberg nucleus can be extracted from Fig. 3.3(b). For example, at $n = 30$ the classical Rydberg S-orbit is 1800 a_0 in radius. To have on average one perturber placed inside this orbit, the density has to be at least $2 \times 10^{11}\,\mathrm{cm}^{-3}$. In the experiment, the sample is illuminated by radiation resonant with the transition to the Rydberg molecular state. Pairs of atoms which have the right distance to form a bound molecular state can then be excited.

First signatures of the effect of perturber atoms inside the Rydberg orbit were already found in 1934 [53, 54], when experiments in thermal vapor cells revealed line shifts and broadening of Rydberg lines, when the pressure inside the cell is increased. They observed that the amount and even the sign of the shift changed when using different background gases. Note that the shift and broadening were independent of the principal quantum number of the Rydberg state. The first theoretical model was presented by Fermi [55], where he introduced his widely known pseudopotential together with the quantum mechanical scattering length. He derived it from the quantum scattering theory for the limit where the range of interaction is small in comparison to the de-Broglie wavelength of the electron.

As the Rydberg electron orbits far from the nucleus, one can treat it as a quasi-free electron and study the interaction analogous to the case of the ion. In comparison to the ion-atom scattering, the effective mass $\mu \approx m_\mathrm{e} = 1\,\mathrm{a.u.}$ is dramatically reduced and therefore, the kinetic term and the centrifugal term are much larger at the same interparticle separations in comparison to the ion-atom case. As the centrifugal term is larger, the internuclear distance, where the C_4-term compensates the centrifugal term is at much lower values of $R^*_\mathrm{e} = \sqrt{2C_4} \approx 18\,\mathrm{a}_0$. The characteristic energy $E^*_\mathrm{e} = 42.7\,\mathrm{meV}$ is nine orders of magnitude higher than for the ion-atom interaction. Analogous to the ionic case, the effective potential for the electron is given by

$$V_{\mathrm{eff,e}}(R_\mathrm{e}) = \frac{l(l+1)}{2R_e^2} - \frac{C_4}{R_\mathrm{e}^4} \tag{3.14}$$

and is plotted for the lowest partial waves in Fig. 3.4 as a function of the electron-atom separation R_e. As the characteristic energy is so different, the temperature scale for the centrifugal barriers is kelvin instead of microkelvin for the ion-atom case. The centrifugal barrier heights are listed in Table 3.2.

The energies need to be compared to the kinetic energy of the scattering process which can be reached. It is given by the semi-classical kinetic energy of the Rydberg electron

$$E_\mathrm{kin} = -\frac{1}{2(n-\delta_{nLJ})^2} + \frac{1}{r} = \frac{k^2}{2}, \tag{3.15}$$

which is the energy, the Rydberg electron gains in the Coulomb potential relative to its binding energy. It is shown in Fig. 3.5(a) for short separations between the Rydberg electron and the core, as the highest kinetic energies are reached in this regime. There, the difference in kinetic energy between a Rydberg state of a moderate $n = 40$ and a high-n Rydberg state is small. As the scattering process is considered to be elastic, the kinetic energy of the

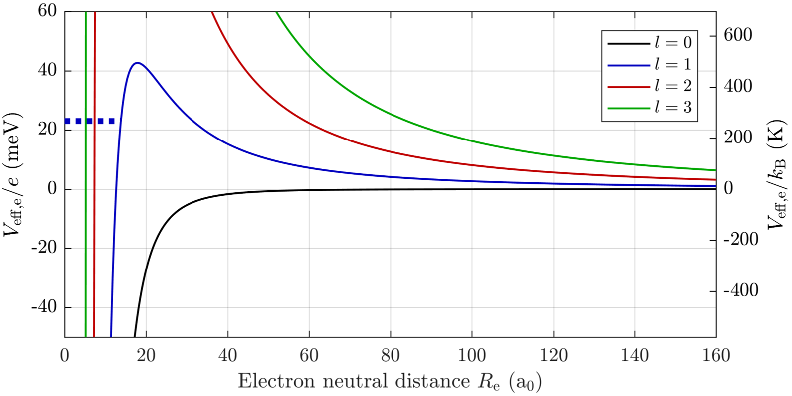

Fig. 3.4: Effective electron-atom scattering potential for partial waves up to $l = 3$. The behavior of the C_4 potential including the centrifugal term is presented as a function of the internuclear distance R_e in terms of energy (left axis) and temperature (right axis). The extracted centrifugal barrier heights are listed in Table 3.2. In contrast to the ion-atom scattering, the effective mass is now only m_e instead of $0.5 \times m(^{87}\mathrm{Rb})$. The dashed line indicates the energy of the p-wave scattering resonance.

partial wave	$l = 1$	$l = 2$	$l = 3$	$l = 4$
centrifugal barrier	42.7 meV	383 meV	1535 meV	4258 meV

Table 3.2: Centrifugal barrier heights for electron-atom scattering in ^{87}Rb.

Rydberg electron is calculated for one fixed n^* of a state of interest. This kinetic energy is used to calculate the terms for all Rydberg states taken into account.

The kinetic energy needs to be compared to the heights of the centrifugal barriers (Table 3.2), in order to decide how many partial waves have to be taken into account to adequately describe the electron-atom scattering. One finds that even for $n \to \infty$ the electron needs to approach the nucleus to $r = 71\,\mathrm{a}_0$ in order to gain enough energy to overcome the d-wave barrier. Internuclear separations such low are not relevant in typical experiments. Therefore, the discussion can be restricted to s- and p-wave scattering only. Furthermore, at these low distances the covalent bonds starts to play a role and the applicability of the Fermi model is questionable.

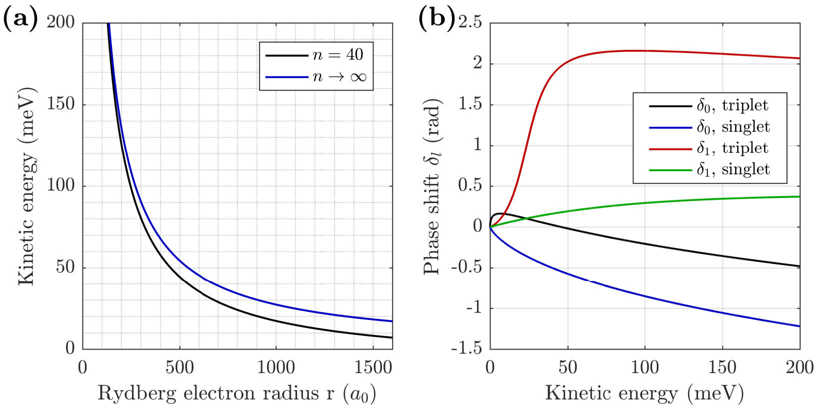

Fig. 3.5: Kinetic energy and phase shift δ_l for e$^-$-Rb collision. (a) The semi-classical kinetic energy of the electron-atom scattering process is presented as a function of the distance between the ionic core and the Rydberg electron r. (b) Scattering phase shifts for electron-atom s- and p-wave scattering for both singlet and triplet scattering is shown as a function of the kinetic energy of the scattering process. The phase jump of π in the p-wave triplet scattering channel indicates a scattering resonance.

One might think, that even p-wave scattering should not play a big role, as $r < 637\,\mathrm{a}_0$ to reach high enough kinetic energies to overcome the centrifugal barrier. However, it turns out that for ^{87}Rb there is a quasi-bound state behind the p-wave barrier which causes a shape resonance in the scattering cross section. If the kinetic energy matches this energy, the free particles couple resonantly to the quasi-bound state of Rb$^-$ behind the p-wave barrier. The corresponding energy is marked as a dashed line in Fig. 3.4.

This can also be seen by checking the scattering phase shifts δ_l, presented in Fig. 3.5(b), provided by I. Fabrikant [98]. According to Ref. [99], there is a phase jump of π at the resonance positions, which is the resonant contribution to the phase shift. In addition, there is an offset to the total scattering phase shift called the potential phase. At the resonance, δ should follow an arccot behavior. Therefore, the resonance position corresponds to the inflection point in the phase shift. This results in resonance positions at about 23 meV for the phase shifts of Ref.[98]. Sometimes, the potential phase is neglected and the phase shift of $\pi/2$ at attributed to the resonance. However, for our case this results in a kinetic energy value which is significantly higher

(32 meV).

For high n the kinetic energy of 23 meV is reached at $r \approx 1000\,\mathrm{a_0}$, which is a reasonable length scale for dense ultracold clouds. Moreover, also for larger r, away from the resonance, the phase shift is modified. Therefore, one can not neglect the p-wave term in the calculations of the electron-atom interaction.

In the scattering process the phase shifts also depend on the relative spin configuration of the electron and the spin of the neutral atom. Therefore, the phase shifts in Fig. 3.5 include curves for both triplet and singlet scattering. Details on the spin configurations and the implications for Rydberg molecules will be discussed in section 3.4.

As the range of interaction for the electron-atom scattering process is small in comparison to the de-Broglie wavelength of the electron and the interparticle spacing, one can follow the treatment of Fermi [55], who simplified the problem by the use of a δ-potential instead of the C_4-potential. Omont [100] later on extended it, in order to include the p-wave term as well, such that the potential for the s- and p-wave are given by

$$\begin{aligned} V_\mathrm{s} =& 2\pi a_\mathrm{s}(k)\delta^{(3)}(\mathbf{r}-\mathbf{R}) \\ V_\mathrm{p} =& 6\pi a_\mathrm{p}(k)\delta^{(3)}(\mathbf{r}-\mathbf{R})\overleftarrow{\nabla}\cdot\overrightarrow{\nabla}, \end{aligned} \tag{3.16}$$

where the δ function is non-zero for the case, where the Rydberg electron at position $\mathbf{r}$ is at the position $\mathbf{R}$ of the neutral perturber atom. All the information about the potential is condensed into the scattering lengths $a_l(k)$ depending on the phase shift as

$$a_l(k) = -\frac{\tan(\delta_l(k))}{k^{2l+1}}. \tag{3.17}$$

Classically, for a hard core potential with infinite height, a_s corresponds to the extent of the potential. In a quantum mechanical description it can be interpreted as the spatial displacement the outgoing wave has in comparison to the incoming plane wave for large R_e. The calculation of the phase shifts presented in Fig. 3.5 starts at $k = 0.003$. For k-values smaller than that, we extrapolated the phase shift with a modified value for the $(2l+1)$ exponent in Eq. 3.17, to meet the zero-energy scattering lengths of $a_0^\mathrm{T} = -16.1\,\mathrm{a_0}$ for triplet and $a_0^\mathrm{S} = 0.63\,\mathrm{a_0}$ for singlet scattering [101].

3.4 Born-Oppenheimer potential energy curves

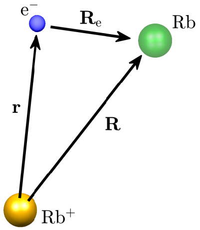

Fig. 3.6: Sketch of the coordinates $\mathbf{r}$ between Rydberg ionic core and Rydberg electron, $\mathbf{R}$ between the Rydberg ionic core and the neutral ground-state atom, and $\mathbf{R}_\mathrm{e}$ between the Rydberg electron and the neutral ground-state atom.

In order to investigate the interaction of the Rydberg atom with a neutral atom located inside the Rydberg orbit and the formation of an ultralong-range Rydberg molecule, we have to combine the interactions between the Rydberg electron, the ionic core and the neutral perturber. Due to the large difference of the motional timescales for the electron and the nucleus, the wave function of the molecule can be described by a product of an electronic component and a component comprising vibration and rotation. This is called the Born-Oppenheimer approximation. On this assumption, one can evaluate the Hamiltonian for the electronic component for each position $\mathbf{R}$ of the neutral atom with respect to the nucleus of the Rydberg atom independently, neglecting the motion of the two nuclei. Then, one can combine these R-dependent values and interpret it as the time-averaged potential the neutral atom experiences. In these potential curves, which are called Born-Oppenheimer potential curves or adiabatic potential energy curves (PECs), molecular bound states are predicted which are the ultralong-range Rydberg molecules. These ultralong-range Rydberg molecules were first proposed by C. Greene and coworkers [36] in 2000.

The Hamiltonian for the interaction of the Rydberg atom with a neutral atom can now be assembled including all three contributions

$$\hat{H}(\mathbf{r},\mathbf{R}) = \hat{H}_0(\mathbf{r}) + \hat{H}_{\mathrm{e,n}}(\mathbf{r},\mathbf{R}) + \hat{H}_{\mathrm{i,n}}(\mathbf{R})\,. \tag{3.18}$$

As introduced in section 2.2, the interaction between the Rydberg electron and the ionic core is given by $\hat{H}_0(\mathbf{r})$ and its eigenvalues are the energy levels of a bare Rydberg atom. The second part of the Hamiltonian $\hat{H}_{\mathrm{e,n}}(\mathbf{r},\mathbf{R})$ describes the scattering of the quasi-free Rydberg electron with the neutral atom as introduced in section 3.3 and depends on both the position $\mathbf{r}$ of the electron and $\mathbf{R}$ of the neutral atom. Finally, $\hat{H}_{\mathrm{i,n}}(\mathbf{R})$ denotes the term for the ion-atom interaction according to section 3.2. The relative coordinates between the three particles are sketched in Fig. 3.6, where $\mathbf{r}$ denotes the distance between Rydberg ionic core and Rydberg electron, $\mathbf{R}$ refers to the distance between the Rydberg ionic core and the neutral ground-state atom, and $\mathbf{R}_e$ labels the distance between the Rydberg electron and the neutral ground-state atom.

3.4.1 PECs for electron-atom s-wave triplet scattering

We will now, step by step, include more details into the electron-atom scattering process and discuss characteristic features in the Born-Oppenheimer potentials related to them. For the beginning, the electron-atom scattering is only described by the s-wave scattering term and we assume the spin of the electron and the neutral atom to be parallel. For this simplified case the Hamiltonian is given by

$$\hat{H}(\mathbf{r}, R) = \hat{H}_0 + 2\pi a_{\mathrm{s}}^{\mathrm{T}}(k(R))\delta^3(\mathbf{r} - R\hat{\mathbf{z}}) - \frac{C_4}{R^4}, \tag{3.19}$$

with the z-axis pointing along the internuclear axis. Here, $a_{\mathrm{s}}^{\mathrm{T}}$ refers to the triplet s-wave scattering length. One can then evaluate the matrix elements $\langle\Psi|\, \hat{H}(\mathbf{r}, R)\, |\Psi'\rangle$ of the Hamiltonian for a truncated basis and find the new eigenenergies and eigenstates of the system (including the interactions) by numerical diagonalization of this matrix. The results will be discussed later.

In Greene's first proposal, he also restricts the discussion to the case of s-wave triplet scattering and neglected the C_4-term as it only plays a role for small R. To get a first intuition for the shape of the molecular potential curves, one can start with a well isolated state Ψ_{iso}, where coupling to other states can be neglected e.g. due to a large quantum defect. Then, one can restrict the basis to the single state of interest and evaluate $\langle\Psi_{\mathrm{iso}}|\, \hat{H}(\mathbf{r}, R)\, |\Psi_{\mathrm{iso}}\rangle$ to end up with the Born-Oppenheimer potential

$$U_{\mathrm{iso,T}}(R) = E_{\mathrm{iso},0} + 2\pi a_{\mathrm{s}}^{\mathrm{T}}(k(R))\, |\Psi_{\mathrm{iso}}(R)|^2 - \frac{C_4}{R^4}. \tag{3.20}$$

As the S-state is split off from the hydrogenic manifold by the quantum defect, it can to first order be treated as such an isolated state. In Fig. 3.7(b) the PEC for the 40S state is presented[2]. If the distance R is sufficiently large, the C_4-term gets small, such that the potential curve is given by the energy of the bare isolated Rydberg state $E_{\mathrm{iso},0}$ and a modulation resembling the electron probability density $|\Psi_{\mathrm{iso}}(R)|^2$. Pictorially, at positions R where the electron is more likely to be, it will interact more strongly with the neutral

---

[2] Retrieved from full diagonalization. For all PECs presented in section 3.4, 40S state in Rubidium-87 is chosen as state of interest and 36m, 39P, 38D, 40S, and 37m were included in the diagonalization.

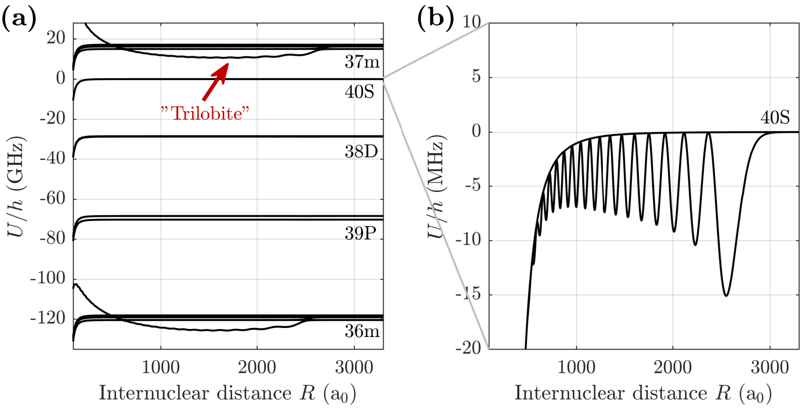

Fig. 3.7: Adiabatic potential energy curves U in the vicinity of the 40S state ($U = 0$) are presented as a function of internuclear distance R between the Rydberg nucleus and the neutral atom. Only triplet s-wave scattering is included for the electron-atom scattering process. (a) PECs in the vicinity of the 40S state. The ^{3}S Trilobite state detaches from the hydrogenic manifold. (b) Zoom-in on the 40S state.

atom and therefore, the potential will have dips[3]. For very small internuclear separations the C_4-potential dominates and the potential bends down.

The deepest bound molecular state, localized in the outer most potential well, allows for binding energies which range from GHz for $n \approx 20$ down to a few hundreds of kHz for $n \approx 70$. When the principal quantum number n increases, the Rydberg orbit increases proportional to n^2. As the probability density for the Rydberg electron wave function is normalized to one over the volume of the Rydberg orbit, the squared amplitude of the wave function reduces $\propto n^{-6}$ for increasing n. Therefore, also the depth of the outer most well of the Born-Oppenheimer potential decreases proportional to n^{-6} [40]. The binding energies of the ultralong-range Rydberg molecules decrease accordingly, up to the point where the molecular wave function starts to spread out over several valleys of the potential.

An exemplary molecular electron probability density for the 40S ultralong-range Rydberg molecule at a fixed distance of $R = 2548\,\mathrm{a}_0$ is presented in Fig. 3.8(a). The position of the nucleus of the Rydberg atom is marked in red, while the position of the neutral atom is depicted by the green dot.

---

[3] as $a_\mathrm{s}(k = 0) < 0$ in this case. For $a_\mathrm{s}(k = 0) > 0$ peaks will appear.

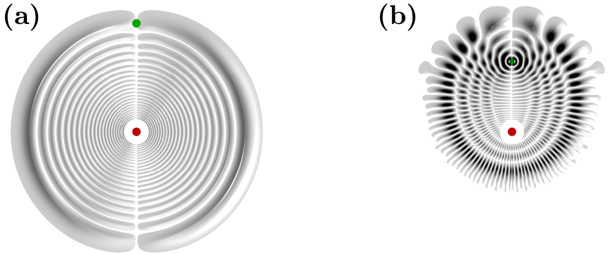

Fig. 3.8: Weighted electron probability density for triplet S-type and Trilobite Rydberg molecules. The position of the Rydberg core(red) and the neutral perturber atom (green) are marked. (a) The electron probability density is presented for the 40S ultralong-range Rydberg molecule in the R, z-plane for the neutral atom at $R = 2548\,\mathrm{a}_0$. (b) The electron probability density is shown for the $37m$ Trilobite Rydberg molecule in the R, z-plane for the neutral atom at $R = 1655\,\mathrm{a}_0$.

The molecular wave function is almost unperturbed in comparison to a bare Rydberg S-state orbital.

First ultralong-range Rydberg molecules bound in potentials stemming from such isolated Rydberg S-states in rubidium were experimentally observed in 2009 [38] by means of photo-association. Thereto, Rydberg spectroscopy is performed in the vicinity of an atomic Rydberg resonance, and the molecular binding energy is extracted from the frequency difference between the atomic and the molecular line. By now, not only rubidium S-type molecules have been photo-associated, but also P-type and D-type molecules and investigations have been extended to Rydberg molecules in cesium and strontium as well [44, 45, 47, 102–104]. In contrast to the photo-association of Rydberg molecules, Bellos et. al. [105] presented the excitation of Rb_2 molecules to Rydberg molecular states. Not only molecules in the vibrational ground state, but also vibrationally excited molcular states can be photo-associated [38].

In addition, trimer, tetramer and even pentamer molecules have been found [39, 40]. As the electronic wave function for the S-type molecule is almost identical to the wave function of the bare Rydberg S-state, one can assume, that the molecular potential for a second, third, or forth neutral atom in the orbit is to first order equal to the calculated two-body potential. Experimental studies of poly-atomic states support this assumption, as the their binding energies were found to be two times (trimer), three times (tetramer), and four times (pentamer) the binding energy of the dimer molecule, as long as all atoms are in the vibronic ground state of the outermost well of the molecular potential.

While the Rydberg S-states can be treated as isolated states, the case is different for degenerate states. One can show that when diagonalizing the scattering term evaluated in the truncated basis $b(\mathbf{r}) = (\Psi_1(\mathbf{r}), \Psi_2(\mathbf{r}), ...\Psi_n(\mathbf{r}))^T$ of the Rydberg states, all eigenvalues except for one equal zero [106]. The single remaining eigenvalue is $\lambda_{\text{Trilobite}}(R) = \sum_i |\Psi_i(R)|^2$ with the eigenvector equal to $b(R)$ as discussed in Appendix A.1. The wave function for this state is given by

$$\Psi_{\text{Trilobite}}(\mathbf{r}, R) = \frac{\sum_i \Psi_i(R)\Psi_i(\mathbf{r})}{\sqrt{\sum_i |\Psi_i(R)|^2}}. \tag{3.21}$$

One can see that for $\mathbf{r} = R\mathbf{z}$, all summands in the numerator are positive, meaning that all Rydberg wave functions interfere constructively. Note that this is independent of the sign of the scattering length. As Rydberg wave functions with $m_L > 0$ are zero on the $\mathbf{z}$-axis, only Rydberg states with $m_J \in \{-\frac{1}{2}, \frac{1}{2}\}$ contribute to this molecular wave function.

Therefore, when performing the full diagonalization for the hydrogen-like states which are almost degenerate, all but one potential energy curve are (almost) unperturbed. The one PEC corresponding to the single non-zero eigenenergy splits off as can be seen in Fig. 3.7(a). The potential is labeled “Trilobite”, as its electron orbital resembles a Trilobite fossil. This can be seen in Fig. 3.8(b), where the weighted electron probability density $R\sin(\theta)|\Psi(R, z)|^2$ is presented. At the neutral atom position, marked in green, the electron probability density is maximized by the constructive interference mentioned before. Due to the strong asymmetry in the electronic wave function, Trilobite Rydberg molecules can possess extraordinarily high electric dipole moments in the range of thousands Debye. A large electric dipole for a homonuclear molecule is very uncommon, as the symmetry between the atoms needs to be broken.

Trilobite Rydberg molecules were already predicted in Greene’s first theory work on Rydberg molecules [36] and were experimentally confirmed in 2015 [42]. A fraction of the large electric dipole moment of the Trilobite is admixed to low-L Rydberg molecules as presented in Ref. [41].

3.4.2 PECs for electron-atom s- and p-wave triplet scattering

The closer the Rydberg electron approaches the ionic core, the more kinetic energy it gains in the Coulomb potential in a semi-classical treatment. At some point, the kinetic energy in the electron-atom scattering process matches

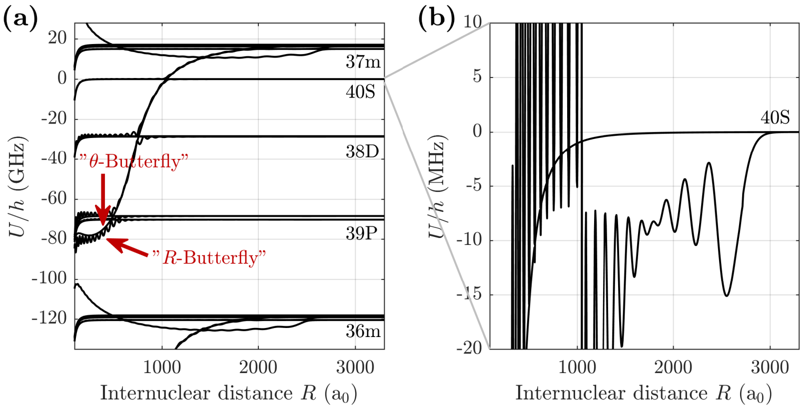

Fig. 3.9: Adiabatic potential energy curves U in the vicinity of the 40S state ($U = 0$) are presented as a function of internuclear distance R between the Rydberg nucleus and the neutral atom. Triplet s- and p-wave scattering is included for the electron-atom scattering process. (a) PECs in the vicinity of the 40S state. The ^{3}P Butterfly states detach from the hydrogenic manifold. (b) Zoom-in on the 40S state.

the energy of the quasi-bound Rb$^-$ state behind the p-wave centrifugal barrier, as discussed in section 3.3. This scattering resonance modifies the molecular potential energy curves. Therefore, the p-wave scattering term, needs to be included in the Hamiltonian [37, 100]

$$\begin{aligned}\hat{H}(\mathbf{r}, R) =&\hat{H}_0 + 2\pi a_\mathrm{s}^\mathrm{T}(k(R))\delta^3(\mathbf{r} - R\hat{\mathbf{z}}) \\ &+ 6\pi a_\mathrm{p}^\mathrm{T}(k(R))\delta^3(\mathbf{r} - R\hat{\mathbf{z}})\overleftarrow{\nabla} \cdot \overrightarrow{\nabla} - \frac{C_4}{R^4},\end{aligned} \tag{3.22}$$

where a_p^T is the triplet p-wave scattering length.

The full diagonalization of this Hamiltonian delivers the PECs presented in Fig. 3.9(a). One can see, that single states detach from the hydrogenic manifold and cross all quantum defect states. This is in analogy to the behavior of the (almost) degenerate states for the s-wave scattering term: Evaluating the p-wave term in the truncated basis $b(\mathbf{r}) = (\Psi_1(\mathbf{r}), \Psi_2(\mathbf{r}), ...\Psi_n(\mathbf{r}))^T$ of degenerate Rydberg states yields eigenvalues equal to zero except for three eigenvalues given by $\lambda_\xi(R) = \sum_i |\nabla_\xi \Psi_i(R)|^2$. Splitting the p-wave term into three spatial contributions for the gradients ∇_ξ with $\xi \in \{r, \theta, \phi\}$ leads to three single PECs splitting off from the manifold states. Their corresponding

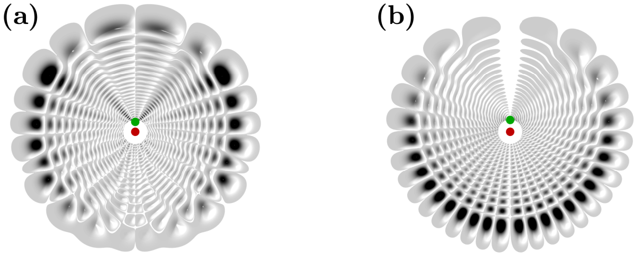

Fig. 3.10: Weighted electron probability density for triplet R-Butterfly and θ-Butterfly Rydberg molecules. The position of the Rydberg core (red) and the neutral perturber atom (green) are marked. (a) The electron probability density for the $37m$ R-Butterfly Rydberg molecule in the R, z-plane for the neutral atom at $R = 232\,\mathrm{a}_0$. (b) The electron probability density for the $37m$ θ-Butterfly Rydberg molecule in the R, z-plane for the neutral atom at $R = 277\,\mathrm{a}_0$.

wave function is given by

$$\Psi_{\xi-\text{Butterfly}}(\mathbf{r}, R) = \frac{\sum_i (\nabla_\xi \Psi_i(R))\Psi_i(\mathbf{r})}{\sqrt{\sum_i |\nabla_\xi \Psi_i(R)|^2}}. \tag{3.23}$$

The PEC, where the gradient along R is evaluated exhibits oscillatory behavior delivering the curve labeled R-Butterfly in Fig. 3.9. In Fig. 3.10(a) the corresponding electronic orbital is presented, where the radial gradient of the wave function is maximum at the position of the neutral atom (green). The term “Butterfly” was already introduced in [37], as the electron orbit has two “wings” of high electron probability density. The two states for $\xi \in \{\theta, \phi\}$ have the same eigenvalues, leading to the PEC referred to as θ-Butterfly or angular Butterfly, which shows no oscillation along R. A maximum angular gradient in the electronic wave function at the position of the neutral atom, can be seen in the weighted electron probability density Fig. 3.10(b). Calculating the gradients of the wave functions, one obtains that only states with $m_L = 0$ contribute to the R-Butterfly, while states with $m_L = \pm 1$ contribute to the angular Butterfly states.

Butterfly states are composed of high-L Rydberg levels, such that photo-excitation starting from a ground state atom does not provide enough angular momentum to couple to these PECs. Niederprüm et. al. [43] managed to photo-associate Butterfly molecules close to the level crossing with a Rydberg P-state, where sufficient P-character is admixed to the Butterfly states.

Coming back to the low-L states which are more common in experiments, one can study the 40S ultralong-range Rydberg molecular state, presented in Fig. 3.9(b). The R-Butterfly crosses at about $1000\,\mathrm{a}_0$ and couples strongly to the S-state. This reduces the energy for R greater than the resonance position and increases the energy for smaller internuclear distance. In contrast, the angular Butterfly state crosses without coupling. As long as only Rydberg molecular states bound in the outermost well are considered, the binding energy of the S-type Rydberg molecule is not changed dramatically by the p-wave term.

3.4.3 PECs for electron-atom s- and p-wave singlet and triplet scattering

As long as the electronic spins $\hat{S}_1$ of the Rydberg electron and the spin $\hat{S}_2$ of the neutral atom are parallel, the above treatment taking only triplet scattering into account is valid. In general, however, both triplet and singlet scattering has to be considered.

For the discussion of the angular momenta involved, the index 1 will label the Rydberg electron state, whereas the index 2 refers to the valence electron of the neutral atom. The orientation of electron spin $\hat{S}_1$ of the Rydberg electron relative to the orientation of the electron spin $\hat{S}_2$ of the neutral atom can be either parallel or antiparallel. For the configurations $\uparrow\uparrow$, $(\uparrow\downarrow+\downarrow\uparrow)/\sqrt{2}$, and $\downarrow\downarrow$ the total angular momentum in the scattering process is one, corresponding to triplet scattering. In contrast, for $(\uparrow\downarrow-\downarrow\uparrow)/\sqrt{2}$ it is zero corresponding to singlet scattering. If the spin configuration in the experiment is for example $\uparrow\downarrow$ both, the singlet and the triplet scattering channel contribute. To include this qualitative arguments in the Hamiltonian, one defines the two projectors

$$\begin{aligned}\hat{\mathcal{P}}_\mathrm{T} &= \frac{3}{4} + \hat{S}_1 \cdot \hat{S}_2,\\ \hat{\mathcal{P}}_\mathrm{S} &= \frac{1}{4} - \hat{S}_1 \cdot \hat{S}_2,\end{aligned} \tag{3.24}$$

which project the spin-part of the state onto the the triplet (T) and singlet (S) subspace. The part of the Hamiltonian describing the scattering process is then extended to

$$\begin{aligned}\hat{H}_\mathrm{sc}(\mathbf{r},R) = &\left[2\pi a_\mathrm{s}^\mathrm{T}(k(R))\hat{\mathcal{P}}_\mathrm{T} + 2\pi a_\mathrm{s}^\mathrm{S}(k(R))\hat{\mathcal{P}}_\mathrm{S}\right]\delta^3(\mathbf{r}-R\hat{\mathbf{z}})\\ &+ \left[6\pi a_\mathrm{p}^\mathrm{T}(k(R))\hat{\mathcal{P}}_\mathrm{T} + 6\pi a_\mathrm{p}^\mathrm{S}(k(R))\hat{\mathcal{P}}_\mathrm{S}\right]\delta^3(\mathbf{r}-R\hat{\mathbf{z}})\overleftarrow{\nabla}\cdot\overrightarrow{\nabla},\end{aligned} \tag{3.25}$$

to take care of s-wave singlet and triplet scattering as well as p-wave singlet and triplet scattering. The corresponding singlet phase shifts are included in Fig. 3.5. The singlet p-wave scattering does not show a resonance, as there is no phase jump of π in the phase shift.

When this scattering Hamiltonian is applied, there will be a singlet Trilobite molecular state emerging in addition to the triplet Trilobite splitting off from the almost degenerate states of the hydrogenic manifold. For this state, the electron probability density is also maximized at the position of the perturber - the corresponding PEC however, looks different as $a_\mathrm{s}^\mathrm{S}(k(R))$ differs from the triplet case (and even $a_\mathrm{s}^\mathrm{S}(0) > 0$). In the same way, additional singlet Butterfly molecular states appear, again maximizing the gradient of the wave function along R, θ, and ϕ.

However, it is not sufficient to only extend the scattering Hamiltonian by the singlet terms, because the electronic quantum numbers S_1, S_2 are no good quantum numbers for the full system. As discussed in section 2.1, the Rydberg electron spin couples to its angular momentum $\hat{L}_1$ leading to the fine structure of the Rydberg levels. Fortunately, the coupling to the nuclear spin $\hat{I}_1$ can be neglected for sufficiently high lying states. For the neutral atom with its electronic spin $\hat{S}_2$ it is vice versa: As the neutral atom is in its electronic ground state, the angular momentum L_2 is zero and does not need to be taken into account. Though, the interaction between $\hat{S}_2$ and the nuclear spin $\hat{I}_2$ is of significant strength. Therefore, the hyperfine interaction for the neutral atom (see section 2.1) has to be accounted for. All relevant spins involved in the problem as well as their couplings are sketched in Fig. 3.11. The basis to describe the full system is now given by $|n_1, L_1, J_1, m_{J_1}\rangle \otimes |m_{S_2}, m_{I_2}\rangle$, where the first part describes the spin-orbit coupled state of the Rydberg electron. The second part refers to the neutral perturber atom with the valence electron in the $5\mathrm{S}_{1/2}$ state. The full Hamiltonian reads

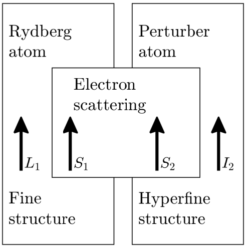

Fig. 3.11: Sketch of the spin-couplings involved in the scattering between the Rydberg electron and a neutral atom.

$$\begin{aligned}\hat{H}(\mathbf{r}, R) =& \hat{H}_0 + \left[2\pi a_\mathrm{s}^\mathrm{T}(k(R))\hat{\mathcal{P}}_\mathrm{T} + 2\pi a_\mathrm{s}^\mathrm{S}(k(R))\hat{\mathcal{P}}_\mathrm{S}\right] \delta^3(\mathbf{r} - R\hat{\mathbf{z}}) \\ &+ \left[6\pi a_\mathrm{p}^\mathrm{T}(k(R))\hat{\mathcal{P}}_\mathrm{T} + 6\pi a_\mathrm{p}^\mathrm{S}(k(R))\hat{\mathcal{P}}_\mathrm{S}\right] \delta^3(\mathbf{r} - R\hat{\mathbf{z}})\overleftarrow{\nabla} \cdot \overrightarrow{\nabla} \\ &+ A_\mathrm{HFS}\hat{\mathbf{S}}_2 \cdot \hat{\mathbf{I}}_2 - \frac{C_4}{R^4} \,. \end{aligned} \tag{3.26}$$

Note, that the spin-orbit coupling of the Rydberg electron is already included in $\hat{H}_0$ (see section 2.1).

The result of a full diagonalization of this Hamiltonian in a truncated basis for different interatomic distances R leads to the PECs depicted in Fig. 3.12(a). In comparison to the previous case, there are two sets of PECs: One set for $F_2 = 1$ lowered in energy by $-\frac{5}{2}A_{\text{HFS}}$ and one for $F_2 = 2$ increased in energy by $\frac{3}{2}A_{\text{HFS}}$. Some of the potential curves of the $F_2 = 2$ show no difference to the PECs calculated in section 3.4.2 except for an energy offset. This is due to the fact that for the electron in a fully stretched state and a parallel spin of the neutral atom, the triplet scattering case is regained. For all other cases, singlet and triplet scattering is mixed which can be illustrated by considering the configuration $\downarrow_{S_1}\uparrow_{S_2}$ which is present in both the triplet $(\uparrow\downarrow+\downarrow\uparrow)/\sqrt{2}$ channel and the singlet $(\uparrow\downarrow\text{-}\downarrow\uparrow)/\sqrt{2}$ channel. The fact that this state is coupled to the $\uparrow_{S_1}\downarrow_{S_2}$ configuration indicates, that states of different m_{F_2} of the neutral atom get coupled. The only good quantum number remaining as long as fields are absent or pointing along z is the sum of all magnetic quantum numbers

$$m_k = m_{J_1} + m_{S_2} + m_{I_2}. \tag{3.27}$$

In Fig. 3.12(b), the potential energy curves for the 40S+5S($F_2 = 2$) molecular state are presented as a function of interparticle separation. One can see, that there is one potential, which is of pure triplet character, that is unchanged in comparison to Fig. 3.9(b). In addition, there is a shallower potential showing up, which is the one of mixed singlet and triplet character. Remarkably, the mixing leads only to attractive curves in Fig. 3.9(b), although $a_{\text{s}}^{\text{S}}(0) > 0$.

Including the singlet scattering channels and the hyperfine interaction into the calculation of these potential energy curves was first presented by Anderson et. al. [44] and discussed at the example of Rydberg D-states. The first experimental observation was in 2015 [45] and later Ref. [5] followed, where magnetic offset fields were included enabling the tuning between singlet and triplet contributions. In Ref. [47], Niederprüm et. al. showed, that the excitation of Rydberg molecules, where different F_2-character is mixed, can be applied to induce remote spin flips in the neutral atom.

One more effect modifying the Born-Oppenheimer potential curves is the coupling of the angular momentum l in the p-wave scattering process to the total spin of the scattering process [107, 108], which is the sum of the Rydberg electron spin S_1 and the neutral atom spin S_2. This leads to more

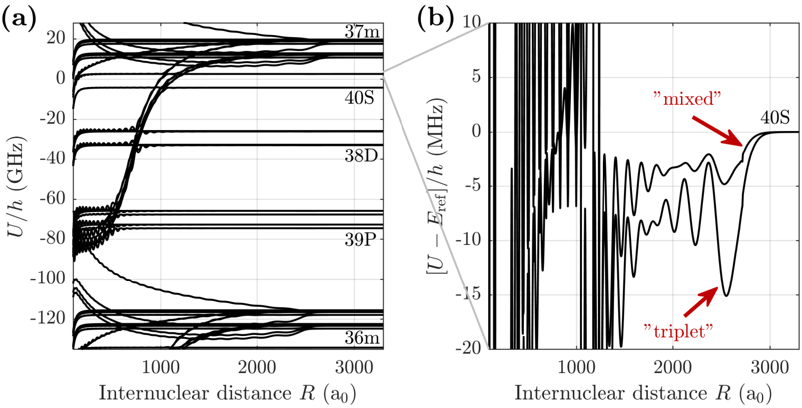

Fig. 3.12: Adiabatic potential energy curves U in the vicinity of the 40S state ($U = 0$) is presented as a function of internuclear distance R between the Rydberg nucleus and the neutral atom. Triplet and singlet, s- and p-wave scattering is included for the electron-atom scattering process and the hyperfine structure of the neutral atom is considered. (a) PECs in the vicinity of the 40S state. (b) Zoom-in on the 40S+5S($F_2 = 2$) state, offset by the hyperfine energy of the $F_2 = 2$ state which is $E_{\mathrm{ref}} = \frac{3}{2}A_{\mathrm{HFS}}$.

p-wave terms in the Hamiltonian depending on the coupled spin $j = 0, 1, 2$ with different momentum dependent phase shifts, resulting in more Butterfly Born-Oppenheimer potential curves separating from the hydrogenic manifold. This term is not included in our calculations, yet. Up to now, the term has not been rigorously identified in experiments, although first hints are discussed in Thomas et al. [48].

3.4.4 Calculation of the Born-Oppenheimer potentials

In order to retrieve the Born-Oppenheimer potential curves from the Hamiltonians presented in the previous sections, we start with the eigenstates of the bare Rydberg Hamiltonian (as detailed in section 2) as the basis for the calculation including interactions. These basis states in the J-basis are characterized by the quantum numbers $n_1, L_1, J_1, m_{J_1}, m_{S_2}, m_{I_2}$, where the state of the Rydberg electron is given in the J_1-basis.

The entries of the matrix representation of the Hamiltonian are thus calculated as

$$\left(\left\langle n_1, L_1, J_1, m_{J_1}\right| \otimes \left\langle m_{S_2}, m_{I_2}\right|\right) \hat{H} \left(\left|n_1', L_1', J_1', m_{J_1}'\right\rangle \otimes \left|m_{S_2}', m_{I_2}'\right\rangle\right). \quad (3.28)$$

The basis needs to be truncated in order to limit the size of the matrix which enables to perform the full diagonalization of the Hamiltonian to find the new eigenenergies and eigenstates for the system including interactions. To find the relevant states that need to be included in the calculation, one state of interest is preassigned. States which are energetically very distant to this state of interest in comparison to their coupling strength won't contribute to the potential curve of the state of interest. Therefore, only states of one or a few neighboring principal quantum numbers are typically taken into account. Including these states prevents the state of interest to diverge at the position of the p-wave shape resonance; the mutual coupling between the states leads to a situation, where only the outermost states diverge. However, one must not choose the basis size too large, as the eigenenergies don't converge. This is a consequence of the δ-potential used in the scattering Hamiltonian and is discussed in detail in Ref. [109].

In order to evaluate the Hamiltonian for the basis states, one has to determine the momentum $k(R)$ of the electron in the scattering process. The semi-classical electron momentum $k(R) = \sqrt{\frac{2}{R} - \frac{1}{(n^*)^2}}$ is applied, corresponding to the kinetic energy the electron gains in the Coulomb potential of the core ion, when approaching it. The scattering process is supposed to be elastic, which means that the kinetic energy has to be the same for all states. Therefore, the semi-classical electron momentum is evaluated for the state of interest and applied to all states taken into account.

The s- and p-wave scattering terms are evaluated for the singlet and triplet case. Therefore, the Rydberg states can no longer be treated in the J_1 basis, but have to be decoupled into the L_1, S_1 basis with the help of Clebsch-Gordan coefficients (see appendix A.2). Then, the relative spin orientation of S_1 and S_2 can be determined. Moreover, for the calculations we choose the perturber atom to be positioned on the z-axis. Then, it is helpful to split the Rydberg wave functions into the radial part and the spherical harmonics $\Psi(\mathbf{r}) = \mathcal{R}(r) Y_L^{m_L}(\theta, \phi)$ as discussed in section 2.2. As the spherical harmonics are defined for the L_1 quantum number rather than the J_1, the change to the L_1, S_1-basis pays off. The choice to use the molecular axis as quantization axis simplifies the calculations, as the spherical harmonics vanish on the z-axis for $m_L \neq 0$ and the gradient of the spherical harmonics vanishes for $m_L \neq \pm 1$. Therefore, only states with $m_L = -1, 0, 1$ need to be included in the calculation. For details on the calculation, especially how the positioning of the perturber on the z-axis simplifies the angular dependence, see appendix A.2.

3.4.5 Systematic errors in the calculation of Born-Oppenheimer potentials

There are some sources of inaccuracies in the calculation of the potential energy curves that need to be discussed: First, as already mentioned above, taking a finite number of neighboring states into account, one misses relevant coupling to the state of interest, but the eigenenergies don't converge when taking more and more states into account. Therefore, one typically restricts the basis size to the neighboring two to four hydrogenic manifolds, as the results show good agreement with results obtained by a Greens-function method [108]. Also the result for states well isolated by their respective quantum defects are in good agreement with the perturbative approach.

Second, the same semi-classical k-value is used for all states, but as their binding energies differ, their respective momentum should change accordingly. This problem is the most prominent for very low principal quantum numbers, where the binding energies of neighboring states differ dramatically. For increasing principal quantum numbers the momentum at fixed R converges and for $\gtrsim 40$, neighboring state have almost identical momentum such that the influence on the PECs is negligible for our work. An additional problem with the momentum dependent scattering length is the following: The p-wave scattering length diverges for small k as can be seen in Eq. 3.17. Therefore, at the position where the semi-classical momentum reaches zero a kink evolves in the potential energy curves. This kink is particularly pronounced for low $n \lesssim 30$ states and impedes the determination of molecular binding energies for these states. There is no established way to overcome this problem for such low principal quantum numbers, but in the work presented in the thesis, only states of higher principal quantum number are of interest.

Third, the use of Fermi's pseudo-potential is only valid as long as the range of interaction for the electron-atom scattering is small in comparison to the electron's de-Broglie wavelength, such that the interaction can be solely described by the phase shift. However, the range of interaction is $18\,\mathrm{a}_0$ and the de-Broglie wavelength of the electron gets similar to that once it gains enough kinetic energy in the Coulomb potential of the ionic core; for example for the $25\mathrm{S}_{1/2}$ $m_J = 1/2$ state presented in Fig. 2.1, the de-Broglie wavelength is about $35\,\mathrm{a}_0$ for the Rydberg electron at $r \approx 200\,\mathrm{a}_0$. This value is almost the same for high principal quantum numbers as well. The use of the δ-potential is not well justified for extremely small separations between the neutral atom and the Rydberg nucleus. However, in our experiments even the nearest neighbor is typically much further away ($\approx 700\,\mathrm{a_0}$) from the Rydberg core.

Fourth, we performed the calculations with sets of phase shifts we received from I. Fabrikant [98]. Comparing them to unpublished phase shifts we received from J. Pérez-Ríos as well as ones from H. Sadeghpour revealed small deviations. For example, we recognized, that calculating S-type Born-Oppenheimer potentials with the phase shifts from J. Pérez-Ríos results in slightly shallower potentials than using the ones from I. Fabrikant.

4

Experimental setup

The experimental setup is designed to prepare dense ultracold samples of Rubidium-87 and study Rydberg atoms in this environment. Therefore, a magneto-optical trap is loaded, the atoms are magnetically transported to the science chamber, followed by evaporative cooling to quantum degeneracy. Subsequently, two-photon excitation allows to excite one atom into a Rydberg state. In order to detect the Rydberg state, electric field ionization is applied and the ions are counted on a multi-channel plate detector. Absorption and phase contrast imaging are used to characterize the ultracold sample.

4.1 Vacuum setup

The experimental setup is designed for the study of Rydberg atoms in an ultracold and dense environment. Parts of it are presented in Refs. [110–115] as the design and built up of the apparatus started already in 2011. The vacuum setup consist of two chambers, a MOT chamber and a science chamber, connected by a magnetic transport. In Fig. 4.1 a half section view of the setup is shown.

The two chamber design allows for loading the magneto-optical trap (MOT) directly from the Rubidium-87 background gas, stemming from a rubidium reservoir attached to the chamber. However, the pressure in the chamber (maintained by an Agilent Vacion Plus 75 Starcell pump) of about 8×10^{-9} mbar hinders the preparation of a Bose-Einstein condensate, as collisions with particles of the background gas lead to heating of the sample. Therefore, the atoms are transported through a (DN 16) pipe of about 45 cm length to the science chamber by subsequently switching twelve pairs of coils (connected in anti-Helmholtz configuration), marked in blue in Fig. 4.1. The pressure in the science chamber is assumed to be 3×10^{-11} mbar, measured by an ion gauge (Varian UHV-24p) in the pumping cross, where an ion pump (Agilent Vacion Plus 150 Starcell Pump) and a titanium sublima-

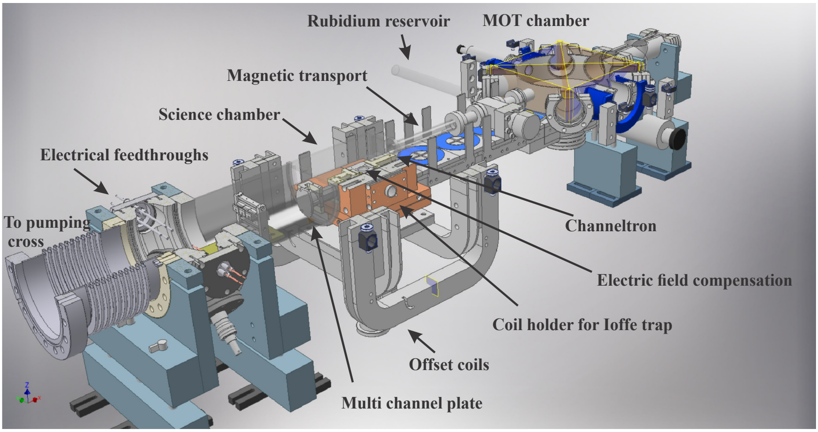

Fig. 4.1: Overview of the experimental setup - half section view. A two-chamber design is used, consisting of a MOT chamber, magnetic transport and a science chamber.

tion pump (Agilent TSP/Mini TI Ball) are installed. Inside the glass cell, the magnetic transport has a 90° turn to insert the atoms into the electric field compensation box. In the science chamber the atoms are held in a Quadrupole-Ioffe-Configuration (QUIC) trap and evaporative cooling allows to prepare thermal samples in the microkelvin temperature regime or even cool down to Bose-Einstein condensation. Subsequently, two-photon Rydberg excitation, electric field ionization and ion detection are performed. Finally, the cloud is imaged either after some time-of-flight after release from the trap, or by in-situ phase contrast imaging in the trap.

The science chamber is a tempax glass cell (Japan Cells custom design), which is anti-reflection coated for 420 nm, 480 nm, 780 nm and 1020 nm. The design of the glass cell is chosen such, that the coils for the QUIC trap holding the atoms can be mounted as close as possible to the atoms to ensure that the currents required can be held reasonable. At the same time, the volume inside the cell needs to be large to have sufficient space for the electric field compensation box and ion detectors.

While the first generation electric field compensation box was made out of titanium (non-magnetic), the second generation of the box, which was inserted into the vacuum setup in 2016, is made out of stainless steel (DIN 1.4404, AISI 316L). The box, displayed in Fig. 4.2 consists of six electric field electrodes to shield the atoms from stray electric fields. Holes in the field plates are covered with 50 µm thick wires to improve the electric field homogeneity inside the box. A radio-frequency antenna is mounted on one of the field plates to provide the RF signal for evaporative cooling. A channeltron (Photonis CEM 5901 MAGNUM) and a multi-channel plate detector (MCP) (Hamamatsu F4655-10) are mounted at the electric field compensation box and are used to detect ions, stemming from ionized Rydberg atoms. The second generation box has a three segment ion lens in front of the MCP detector, to spread the ions over several channels of the MCP. For high resolution phase contrast imaging and focused Rydberg excitation, there were two aspheres (Asphericon A15-12HPX-S) mounted in the top and bottom field plates of the first generation box. In the second generation box, there is only one asphere (Asphericon A15-12HPX-U) implemented which is mounted in the bottom field plate.

Several reasons motivated the change to the second generation electric field compensation box: In the first generation setup, all ions were focused on a single channel of the MCP which lead to destruction of this particular channel. Later, an electric short made the MCP break completely. In addition, in the first generation setup, the RF electrode was wound around the channeltron, causing the channeltron to heat up. Therefore, its resistance was dramatically

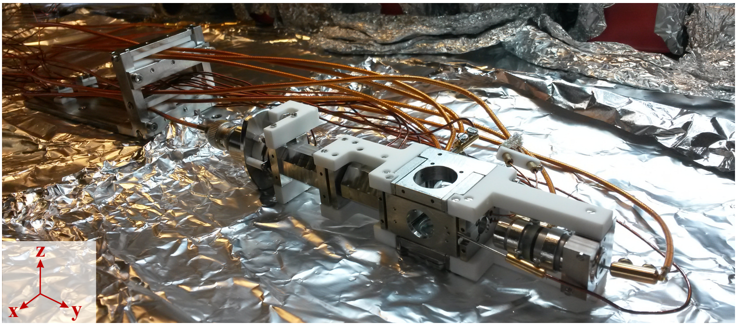

Fig. 4.2: Second generation electric field compensation box. Starting from the cable holder on the very left, there is the MCP detector, the three segments of the ions lens, a cubic field compensation box and a channeltron detector. The asphere mounted in the bottom field plate is not visible, as well as the RF coil which is placed inside the box.

reduced, such that it could not be operated on full front plate voltage and the detection efficiency was thus dramatically reduced. Furthermore, it turned out that the aspheres in the first box were only standard quality but not diffraction limited "ultra" quality which limited the imaging resolution. While the presence of the two aspheres made it easier to align the Rydberg excitation beam, the alignment of the high resolution phase contrast imaging was more challenging, as the beam needs to be collimated between the lenses. Additionally, the electric field stability in the first box was not as good as expected, attributed to the box being made of titanium. However, it turned out, that the improved electric field stability of the new box is mainly due to the larger separation from the high-voltage electrodes of the MCP (and ion lens) to the atoms in comparison to the first generation box - hence the titanium was probably not the limiting factor in the beginning.

4.2 Trapping and cooling of atomic clouds

First, Rubidium-87 atoms are caught in a magneto-optical trap from the background vapor. Therefore, three orthogonal pairs of cooling and repumping laser beams intersect at the center of the magnetic quadrupole field created by a pair of coils in anti-Helmholtz configuration. During MOT loading, there are 6.4 A running through the coils, resulting in magnetic fields of 5.5 G/cm along x,y and 11 G/cm along z. The orientation of the x-,y-, and z-axis

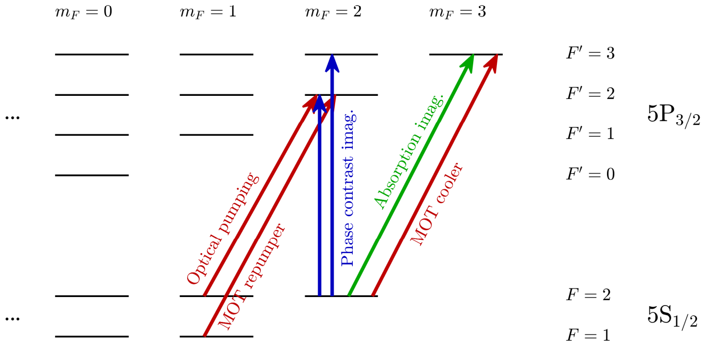

Fig. 4.3: Level scheme ^{87}Rb D2-line including relevant laser transitions for cooling and imaging of the cloud.

with respect to the setup is marked in Fig. 4.2. The transitions at about 780 nm for the MOT cooling and repumping laser are marked in Fig. 4.3. The MOT cooling laser is detuned by about 40 MHz (1.05 Γ) with respect to the transition during MOT loading.

In order to frequency stabilize the MOT lasers, the following procedure is applied: One arm of a reference laser operating at 780.246 nm is coupled into a fiber leading to a fiber coupled electro-optic modulator (EOM) and then to an ultra low expansion (ULE) cavity. The frequency sideband created by the EOM[1] driven at 324 MHz[2] is frequency locked to the cavity using the Pound-Drever-Hall technique [116, 117]. The EOM frequency is chosen such, that the reference laser is in resonance with the ^{85}Rubidium $F = 3 \rightarrow F' = 3, 4$ crossover peak. The beam of this reference laser is then split into three arms and each arm is overlapped with one of the other 780 nm beams (MOT cooler, MOT repumper, imaging laser) on an AC-coupled photodiode. The beat frequencies are stabilized to set point frequencies stemming from a direct digital synthesizer (DDS) board using a delay line lock (frequency dividers are used, as the DDS board can not output such high frequencies). In Fig. 4.4 the set point frequencies for the different laser beams are given, together with the frequency shift of ±80 MHz introduced by acousto-optical modulators (AOMs) used for switching of the laser beams. When the laser frequencies are supposed to change for example between MOT and molasses phase, the

---

[1] EOSPACE PM-0K5-20-PFA-PFA-780-S3mmFS
[2] Windfreak Synth USB II

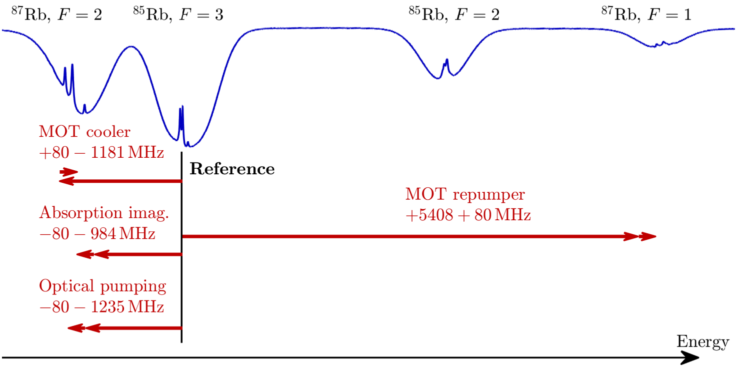

Fig. 4.4: Set point frequencies for the 780 nm lasers which are frequency stabilized with respect to the reference laser by frequency offset locks.

set point frequencies are changed. The reference laser, repumping laser and imaging laser are all external cavity diode lasers(Toptica DL Pro). MOT cooling and optical pumping light stems from the same (Toptica TA Pro) system but is switched with two separate AOMs.

The MOT phase, which takes 9.5 s is followed by a compressed MOT for 12 ms, molasses for 6 ms and optical pumping to the $F = 2$, $m_F = 2$ state for 1.5 ms. The optical pumping is followed by a magnetic transport, which takes about 1.4 s and is discussed in more detail in Ref. [110]. At the end of the transport about one billion atoms arrive with a temperature of about 800 µK. The atoms are held in a quadrupole trap (39.12 A resulting in 135 G/cm along x and y and 270 G/cm along z) and the first RF evaporation ramp is started. After a delay of 5 s, we start to ramp on the Ioffe coil to 48.62 A such that it runs on full current once the first evaporation ramp is over. This additional Ioffe coil is needed to prevent Majorana spin-flip losses in the cloud. The final trap geometry of the Quadrupole-Ioffe-Configuration (QUIC) trap is characterized by the trap frequencies $\omega_r = 2\pi \times 200\,\mathrm{Hz}$, $\omega_a = 2\pi \times 15\,\mathrm{Hz}$ and a magnetic offset field of about 1.7 G.

An overview of the radio-frequency (RF) evaporation ramps is given in table 4.1. If experiments with a non-condensed sample are performed, such as the result presented in section 5, ramp 3a is applied. For the thermal sample the peak density (see App. B.1) results in $5.1 \times 10^{13}\,\mathrm{cm}^{-3}$ for this configuration. A temperature of 1.2 µK and atom number of 6.6×10^{6} are extracted after time-of-flight (TOF) using absorption imaging. This dense

	RF	Time	Atom no.	Temp.	Peak density
Start	45 MHz	0 s	8×10^8	800 µK	
Ramp 1	11.25 MHz	7 s	2×10^8	200 µK	$7 \times 10^{11}\,\mathrm{cm}^{-3}$
Ramp 2	2.8 MHz	4.5 s	3.1×10^7	27 µK	$2 \times 10^{12}\,\mathrm{cm}^{-3}$
Ramp 3a	1.19 MHz	3.5 s	6.6×10^6	1.2 µK	$5.1 \times 10^{13}\,\mathrm{cm}^{-3}$
Ramp 3b	1.04 MHz	3.5 s	1×10^6	0.2 µK	$4.5 \times 10^{14}\,\mathrm{cm}^{-3}$

Table 4.1: Overview of the linear radio frequency ramps used for evaporative cooling. The end frequencies of each ramp and ramp duration is given as well as typical values for the final atom number, temperature, and density for the three cooling ramps applied. When spectroscopy is performed in a thermal ultracold cloud, ramp 3a is chosen. To reach a BEC ramp 3b is applied.

sample is perfectly suited to study ultralong-range Rydberg molecules, as the typical nearest neighbor spacing is $2760\,\mathrm{a_0}$. Hence, for Rydberg S-states with $n < 36$ the nearest neighbor atom is typically located inside the orbit, as can be extracted from Fig. 3.3(a) where the orbit sizes are given.

In contrast, when ramp 3b is applied, the atomic cloud is cooled to Bose-Einstein condensation. The typical BEC has 0.75×10^6 to 1×10^6 atoms (determined 10 MHz offresonant in TOF) and below 2×10^5 atoms in the thermal fraction (determined on resonance). The BEC has peak densities on the order of $4.5 \times 10^{14}\,\mathrm{cm}^{-3}$ and a chemical potential of about 3.6 kHz (see App. B.2). The Thomas-Fermi radius along the short axis is $R_r = 4.6\,\mu\mathrm{m}$ and $R_a = 61\,\mu\mathrm{m}$ along the long trap axis.

This BEC is then used, to load a tiny optical dipole trap [118], which is formed by an 855 nm beam of about 23 µW, focused by the aspheric lens (Asphericon A15-12HPX-U) of high numerical aperture NA= 0.55 in the bottom of our field compensation box down to ≈1.8 µm. After loading, which takes 10 ms, the BEC is shifted away by magnetic field ramps taking 10 ms as well and leaves a micro-BEC in the optical trap.

The micro-BEC is axially confined by the combination of the magnetic trap and the optical trap leading to trap frequencies of $\omega_a \approx 2\pi \times 270\,\mathrm{Hz}$. This trap frequency is measured by monitoring the oscillation of the cloud after a magnetic field kick as presented in Fig. 4.5(a). As the cloud oscillates along the imaging axis, we can detect the oscillation by monitoring the width of the cloud, as it moves in and out of the focal plane of our high-resolution imaging.

Along the radial axes, the micro-BEC is confined by the optical trap, leading to trap frequencies of $\omega_r \approx 2\pi \times 2.4\,\mathrm{kHz}$. This trap frequency is measured via parametric heating. The trap depth is modulated by 3% for 20 ms with a

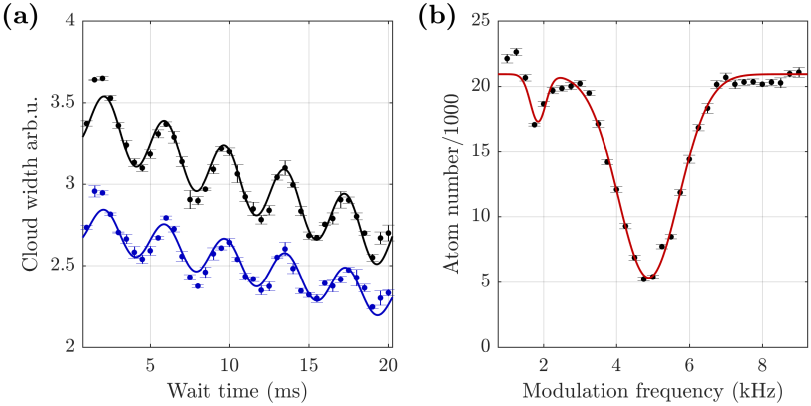

Fig. 4.5: Trap frequency measurements for the micro-BEC. (a) The axial trap frequency is measured by monitoring the cloud oscillation after a magnetic field kick. The black and blue points are fits to the two axes of the cloud which vary as the sample oscillates in and out of the imaging plane. The solid line is a sine fit in addition to a linear decay, revealing a trap frequency of 264(5) Hz for this configuration. (b) The radial trap frequency is measured via parametric heating. Therefore, the atom number is recorded as a function of the trap modulation frequency. The red solid line is a fit of two Gaussian dips, delivering the resonance at 4884(44) Hz for this data set.

certain frequency. Afterwards, the number of atoms that remain in the trap is determined. An exemplary heating curve is presented in Fig. 4.5(b) with a peak at twice the radial trap frequency as the breathing mode of the cloud is excited. Note that the BEC's extent along the trapping beam is significant in comparison to its Rayleigh length. This leads to a distribution of radial trap frequencies along the cloud, which causes the peak in Fig, 4.5 to broaden. The second smaller peak is probably due to a slight deviation of the beam profile in comparison to a Gaussian beam, such that the trap is not perfectly harmonic.

When only taking the optical potential into account, the BEC shape clearly deviates from a Thomas-Fermi profile as the cloud considerably spills out along the beam. In our setup, the additional potential by the magnetic field moderates this effect such that we don't see a significant deviation from a Thomas-Fermi profile when we model the density distribution in the hybrid-trap. The micro-BEC consist of $\approx 5 \times 10^4$ atoms, leading to a peak density of approximately $3 \times 10^{15}\,\mathrm{cm}^{-3}$. Three-body losses limit the lifetime

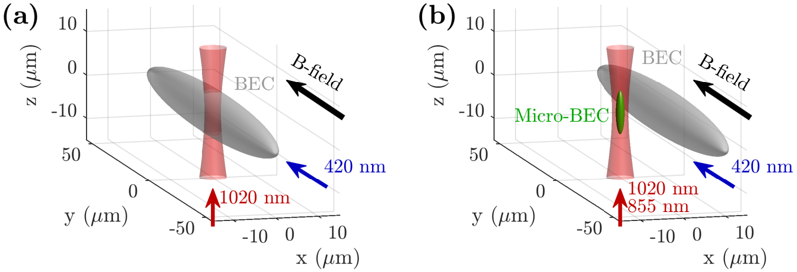

Fig. 4.6: Cloud orientation. (a) When Rydberg spectroscopy is performed in the large BEC, the 420 nm beam illuminates the full cloud along the y-axis while the second excitation beam at 1020 nm is focused through the center of the cloud. (b) For Rydberg experiments in the micro-BEC, the parent large BEC is shifted aside and the focused excitation beam at 1020 nm only excites atoms in the optical tweezer trap.

to $\tau = 19.5\,\mathrm{ms}$. Therefore, the use of higher trap power is not favorable as more atoms would get lost already during the trap loading procedure. The chemical potential of the micro-BEC is $h \times 26\,\mathrm{kHz}$ which corresponds to $k_\mathrm{B} \times 1.2\,\mu\mathrm{K}$. The offset magnetic field amounts 1.72 G but can be increased up to 7.73 G depending on the way we perform the magnetic field ramps to separate the micro-BEC.

The relative positioning of the parent large BEC and the micro-BEC including the magnetic field orientation is illustrated in Fig. 4.6(b). The imaging lens is placed below the sample resulting in an image along the long axis of the micro-BEC.

4.3 Rydberg excitation

Once the sample is prepared, one of the atoms is excited to a nS Rydberg state with $m_J = \{-1/2, +1/2\}$. Therefore, two-photon excitation is performed to excite a single atom to the Rydberg state incorporating the intermediate $6\mathrm{P}_{3/2}$ level at a detuning Δ (see Fig. 4.7). For this, the sample is illuminated with two frequency-tuneable laser beams at wavelengths 420 nm and 1020 nm. We use excitation pulses ranging from 200 ns to 20 µs pulse duration. Within one cloud we perform up to several thousand subsequent excitation pulses. Each excitation pulse is followed by an electric field ionization pulse and the detection of the resulting ions on a detector after some time-of-flight.

The timing of the control AOMs, field ionization pulses and the oscilloscope is triggered using a Swabian Instruments pulse generator. The relative orientation of the large BEC, micro-BEC, magnetic field axis, and the Rydberg excitation beams is illustrated in Fig. 4.6.

Two-photon Rydberg excitatio in rubidium is commonly performed exciting with two lasers at 780 nm and 480 nm via the $5P_{3/2}$ state. However, the excitation scheme used in our experiments incorporating the $6P_{3/2}$ state has some advantages: It is technically more challenging to provide high power at 480 nm than at 1020 nm. Therefore, it is easier to provide sufficiently high coupling strength to the Rydberg state without significant heating of the cloud when using the scheme involving the 1020 nm laser. In addition, frequency tuning of a 1020 nm external cavity diode laser is straightforward, whereas the tuning of a 480 nm laser (which is typically received by second-harmonic generation) is more complicated. Therefore, switching from one Rydberg state to another by setting the laser to a different wavelength requires less effort.

4.3.1 Excitation laser beams

A large beam at 420.3 nm illuminates the whole sample along the y-axis as indicated in Fig. 4.6. The beam has 0.77 mm $1/e^2$ radius and its frequency is detuned by Δ with respect to the transition from $5S_{1/2}$ $F = 2$ to $6P_{3/2}$ $F = 3$. Electric dipole matrix elements and lifetimes for this transition can be found in Ref. [119]. For the frequency stabilization of this laser (Toptica SHG-Pro), a sidearm of the non-frequency doubled seed laser is sent through an EOM[3] generating sidebands. Such a sideband is frequency locked to an ultra-low expansion cavity using the Pound-Drever-Hall technique [116, 117]. Note that the combination of this 420 nm laser with the 855 nm tweezer light can cause atoms to photo-ionize. This can lead to some offset ion count signal on the MCP.

The second laser beam at about 1020 nm propagates along the z-axis as marked in Fig. 4.6. It provides coupling to the desired nS (or nD) Rydberg state. The 1020 nm beam is focused by an high-NA aspheric lens inside our electric field compensation box, resulting in a focal spot size of 2.1(3) µm. This allows to have a larger mean density in the excitation volume in comparison to the mean density of the entire cloud. The focus is overlapped with the trapping beam for the micro-BEC, such that for experiments with the micro-BEC no excitation takes place in the remaining shifted large BEC

---

[3] EOSPACE PM-0K5-20-PFA-PFA-840-S3mmFS; frequency generation: Windfreak Synth USB II

(cf. Fig. 4.6(b)). Analogous to the 420 nm laser, this laser (Toptica TA-Pro) is frequency stabilized using a sidearm that is sent through a fiber-coupled EOM[4] and locking a sideband to the ultra-low expansion cavity using the Pound-Drever-Hall technique [116, 117]. In order to scan the laser in the vicinity of a Rydberg resonance, the EOM is operated by the (amplified) output of a direct digital synthesizer board (Analog Devices AD9959), which is programmed using an Arduino Due. Thereby, we can scan the sideband from 100 MHz to 650 MHz before the lock gets unstable - below 100 MHz we get too close to the carrier peak of the cavity and for 650 MHz the sideband from the neighboring carrier peak comes close, as the free spectral range of the ULE is about 1.5 GHz[5]. It is also possible to scan the frequency even between two excitation pulses (up to 100 kHz), allowing to retrieve a spectrum from a single cloud.

In Fig. 4.7, a sketch of the excitation scheme is presented. The case, where the $|n\mathrm{S}, m_J = +1/2\rangle$ Rydberg state is supposed to be addressed is marked with solid arrows. The 420 nm beam is σ^+-polarized coupling the $\left|5\mathrm{S}_{1/2}, F = 2, m_F = 2\right\rangle$ state to $\left|6\mathrm{P}_{3/2}, F = 3, m_F = 3\right\rangle$ off-resonant by $\Delta = 80\,\mathrm{MHz}$. The coupling to the $m_J = +1/2$ state is provided by the 1020 nm beam, which is linearly polarized. As it is inciding perpendicular to the magnetic field axis, it could in principle drive both σ^+ and σ^--transitions. However, for the case of nS Rydberg states, only the σ^--component will lead to Rydberg excitation to the $|n\mathrm{S}, m_J = +1/2\rangle$ state. This is indicated by the solid arrows in Fig. 4.7(b).

In case of Rydberg excitation to the $|n\mathrm{S}, m_J = -1/2\rangle$ state which is marked with dashed arrows in Fig. 4.7, the blue laser is σ^--polarized and the detuning to the intermediate state is chosen to be $\Delta = 830\,\mathrm{MHz}$. For this detuning being large in comparison to the hyperfine splitting of the state, one can neglect the splitting and treat the state in the J-basis (Fig. 4.7(c)). The σ^--light then couples offresonantly to the $m_J = -1/2$ state and the laser at 1020 nm drives the π-transition to the nS, $m_J = -1/2$ Rydberg state.

4.3.2 Electric field control

For increasing principal quantum number, the electric field sensitivity of the Rydberg atom increases dramatically ($\propto n^7$). Therefore, electric stray fields need to be compensated to observe narrow and non-shifted spectroscopic transitions for high n. The box providing the compensation voltages (Mea-

---

[4] EOSPACE PM-0K5-20-PFA-PFA-1010-SFS3mm

[5] Shifting EOM sidebands of neighboring carrier peaks on top of each other results in $FSR = 1496.4\,\mathrm{MHz}$

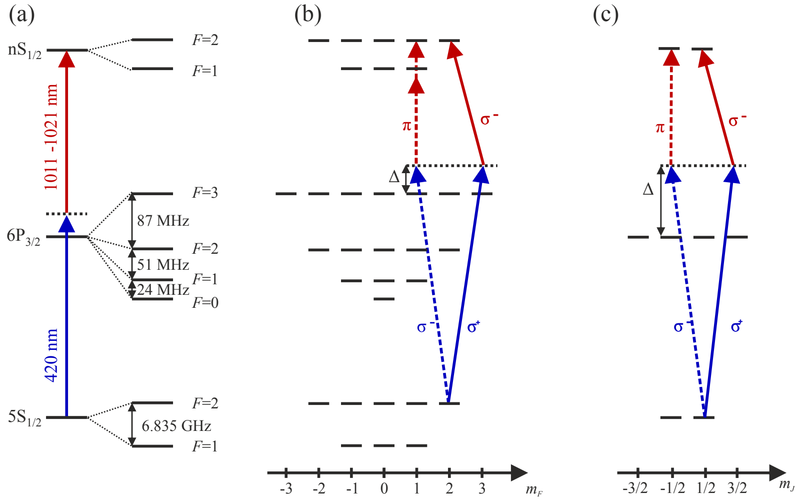

Fig. 4.7: Excitation scheme for nS Rydberg excitation. Depending on the laser polarization and intermediate detuning, $m_J = -1/2$ and $m_J = +1/2$ states can be addressed marked by dashed and solid arrows, respectively (a) Overview of energy levels and splittings involved. (b) Level scheme in the F-basis. (c) Level scheme in the J-basis.

surement Computing USB-3112) can control all electrodes and features very low noise. In order to determine the correct compensation voltages for the six cubically arranged field electrodes, we scan them pairwise applying a constant electric offset field and recording the shift of the Rydberg transition frequency. As discussed in section 2.3.1 the nS Rydberg transition line experiences a quadratic Stark shift. By extracting the minimum shift from a fit, we find the compensation field for the corresponding axis.

In order to compensate for field inhomogeneities two opposing field plates are e.g. put to a slightly increased voltage, while all other four plates are accordingly lowered, to change the gradient of the electric field at the center of the cubus. By scanning the electrode voltages this way, one can observe a broadening or narrowing of the Rydberg line and optimize the voltages for minimal Rydberg transition linewidth.

In our case, the limit is set by the stray field leaking into the cube along the y-axis. It is caused by the high voltage, applied to the MCP front plate and the last lens of the ions lens tubes. Its field inhomogeneities can not be fully compensated by the cubic set of field plates. The residual electric stray field gives rise to a Gaussian linewidth of ≈3 MHz for $n = 190$ and drifts of typically <3 mV/cm per day.

4.3.3 Electric field ionization and detection

In order to detect the Rydberg atoms, an electric field ionization pulse is applied after each excitation pulse. We choose the pulse to provide at least twice the field strength needed to ionize the nS Rydberg state (see section 2.3.1). Thereby, we ensure that we also detect Rydberg atoms which have undergone a state-changing collision and have a larger m_L quantum number [4]. The positive and negative voltage for the field ionization of Rydberg states of $n \lesssim 100$ is provided by two power supplies (TDK Lambda Z650-0.32) for the two field plates on the x-axis. For switching from the compensation fields to the ionization field we use a high-voltage switch (CGC instruments NIM-AMX700-3). For high-n Rydberg states, where voltages below ±10 V are required, an arbitrary function generator (Agilent Technologies 33522B) is used for both the compensation field and the ionization field along the x-axis. It features less noise and faster switching behavior. In addition, state selective ionization ramps can be performed.

The ions are then detected by either the channeltron (Photonis CEM 5901 MAGNUM) or the MCP detector (Hamamatsu F4655-10) after some microseconds of time-of-flight. Rb_2^+ ions, which can be formed by collisions of Rydberg atoms with neutral ground-state atoms [4] have twice the mass of the Rb^+ ions and can hence be identified by their longer time-of-flight.

We want to study the interaction of one Rydberg atom with neutral atoms close by without Rydberg-Rydberg interactions taking place (see section 2.4). Therefore, we aim to produce only one single Rydberg atom in the sample. In typical experiments, the Rydberg blockade radius is much larger than the BEC which should prevent the excitation of a second Rydberg atom in our sample. However, the efficiency of the blockade effect in a high density cloud is an open question. Therefore, as an experimental test, we prepare a low density cloud smaller than the Rydberg blockade radius for $n = 100$ and measure the number of detected ions for a linear increase of excitation power. When the blockade effect sets in, the rate of detected ions starts to deviate from a linear increase. The outcome of such a test is presented in Fig. 4.8, where the ion count rate is shown as a function of the power of the second excitation laser. This test allows us to determine a lower bound for the experimental ion-detection efficiency of at least 40%. Additionally,

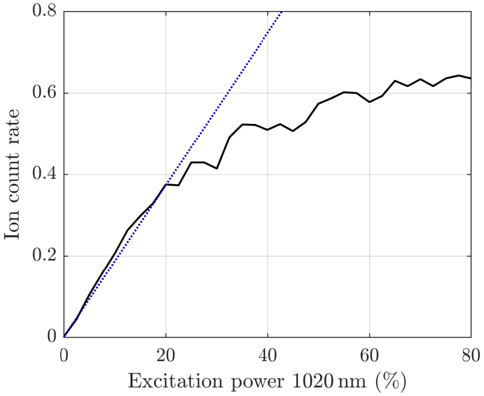

Fig. 4.8: Saturation test for the multi-channel plate detector. The ion count rate is monitored as a function of excitation laser power.

to ensure that we excite less than one Rydberg atom per pulse for the high density case as well, we additionally keep the mean ion count rate below 0.3 ions per excitation pulse.

4.3.4 Diamagnetic shift of the Rydberg level

Rydberg atoms of high principal quantum number experience a significant diamagnetic line shift even at a moderate external magnetic field strength (see section 2.3). Before spectroscopy in a dense sample is performed, the line center frequency of the Rydberg transition is determined independently in a dilute thermal sample held in the QUIC trap, where the offset magnetic field amounts $B_0 = 1.74\,\mathrm{G}$ for the trap configuration chosen in the experiments presented in chapter 6. After loading of the optical micro-trap, an offset field along the x-axis is applied to separate the large BEC from the micro-BEC in the optical trap. Only for the first set of measurements, in addition a magnetic field ramp along y was applied as well, as it leads to a slightly larger atom number for the micro-BEC. However, this magnetic field ramp along y was accompanied by a worse confinement along z and an increased magnetic offset field of $B_1 = 7.73\,\mathrm{G}$. At this magnetic field strength diamagnetic line shifts are relevant for $n > 120$.

Therefore, calibration measurements are performed to characterize the influence of the magnetic offset field. The atomic sample is prepared in the

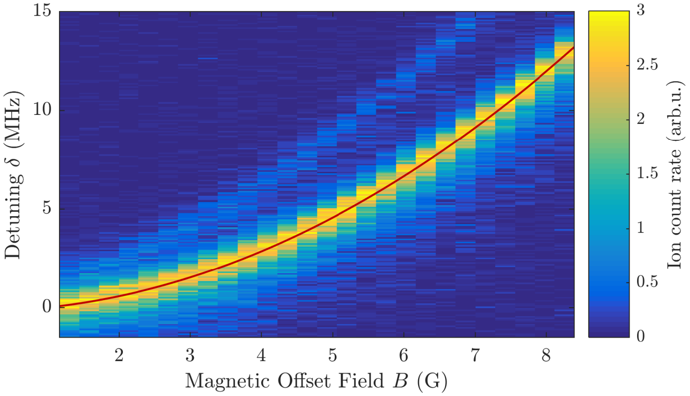

Fig. 4.9: Rydberg spectra for the $\left|160\mathrm{S}_{1/2}, m_J = 1/2\right\rangle$ Rydberg state at varying magnetic offset fields B. Zero detuning is referenced to the atomic Rydberg resonance at zero magnetic field. The red line shows a fit to the data based on Eq. 2.26 to the extracted line centers.

$\left|5\mathrm{S}_{1/2}, F = 2, m_F = 2\right\rangle$ state (Landé factor $g_F = 1/2$), which features the same linear Zeeman shift as the $\left|n\mathrm{S}_{1/2}, m_J = 1/2\right\rangle$ Rydberg states (Landé factor $g_J = 2$). Hence, for the optical transition, the linear Zeeman effect cancels and only the diamagnetic term remains. To quantify the diamagnetic shift for the Rydberg spectra in the dense cloud, for Rydberg states of $n \geq 127$, additional Rydberg spectra have been measured for varying magnetic offset fields of the QUIC trap in a dilute sample. An exemplary dataset for the $\left|160\mathrm{S}_{1/2}, m_J = 1/2\right\rangle$ state is shown in Fig. 4.9. From a quadratic fit to the data based on Eq. 2.26, a correction of 11.8 MHz is obtained for the $\left|160\mathrm{S}_{1/2}, m_J = 1/2\right\rangle$ state in the magnetic field of $B_1 = 7.73\,\mathrm{G}$. The same procedure, applied to the data for $n = 127$ and $n = 190$ results in shifts of 2.9 MHz and 22.1 MHz, respectively.

Note that for the data shown in Fig. 6.6 the altered loading procedure of the micro-BEC (avoiding magnetic fields ramps along the y-axis) results in a negligible change of the magnetic field strength, and consequently no significant diamagnetic shift.

4.4 Imaging of ultracold samples

In order to determine the atom number and temperature of the atomic sample, the cloud is imaged. Performing absorption imaging after time-of-flight allows us to extract both the atom number and temperature. As a second imaging technique, we can apply phase-contrast imaging to image the cloud in-situ in the trap.

4.4.1 Absorption imaging of the density distribution

Absorption images of the cloud are recorded after the atoms are released from the trap and expand during some variable time-of-flight (TOF) which is typically chosen to be 23 ms for clouds of microkelvin temperature in our experiment. For BECs 30 ms of TOF is used as a result of the slower expansion due to the lower temperature (and low chemical potential). The expansion of the cloud is given by it's kinetic energy for long TOFs. The σ^+ polarized imaging light is close to resonance with the transition from the $\left|5\mathrm{S}_{1/2}, F=2, m_F=2\right\rangle$ to the $\left|5\mathrm{P}_{3/2}, F'=3, m_F'=3\right\rangle$ state at $\lambda = 780.247\,\mathrm{nm}$ as indicated in Fig. 4.3. The imaging beam is propagating along the y-axis, antiparallel to the 420 nm Rydberg excitation beam. It is illuminating the cloud for 50 µs and is recorded on a CCD camera (PCO pixelfly usb). Power and detuning of the imaging light is adjusted as well as the TOF to ensure that the imaging light is not fully absorbed by the cloud, to prevent saturation effects in the optical density distribution.

For absorption imaging, we determine the optical density distribution OD from the fraction of the intensity I passing through the cloud and the background intensity I_0. The OD is extracted according to

$$\mathrm{OD} = \log\left(\frac{I}{I_0}\right) = \log\left(\frac{c\varepsilon_0^2/2 \cdot E_0^2 e^{-2\frac{\omega}{c} n''_{\mathrm{ref}} l}}{c\varepsilon_0^2/2 \cdot E_0^2}\right) = \frac{4\pi}{\lambda} n''_{\mathrm{ref}} l, \tag{4.1}$$

where n''_{ref} is the real part of the refractive index and l is the length of the sample. For the closed transition from $F=2, m_F=2$ to $F'=3, m_F'=3$ the electric dipole matrix element is given by the reduced dipole matrix element $d_{\mathrm{red}} = |\langle J=1/2|\,|er|\,|J'=3/2\rangle| = 4.227 e a_0$ multiplied by $\sqrt{1/2}$ [79]. With that, one can calculate the real part of the refractive index according to

$$n''_{\mathrm{ref}} = 1 + n(x,y,z)\frac{d_{\mathrm{red}}^2}{2\varepsilon_0 \hbar \Gamma} \cdot \frac{1}{1+(\Delta/2\Gamma)^2}. \tag{4.2}$$

Here, Δ is the laser detuning with respect to resonance, Γ refers to the natural line width of the transition and $n(x,y,z)$ the three dimensional density distribution of the cloud.

In order to receive the total atom number of the cloud, one has to be aware, that by taking an image the projection of the cloud integrated along one axis is received. For the ideal gas the number of detected atoms is extracted from the column density distribution as

$$N_{\text{detected,Gauss}} = \int\int a \exp\left(-\frac{x^2}{2\sigma_x^2} - \frac{z^2}{2\sigma_y^2}\right)\ dx\ dy = 2\pi a \sigma_x \sigma_y. \quad (4.3)$$

The Gaussian widths σ_x, σ_y of the cloud and the amplitude a are extracted by fitting the mathematical expression in the integral to the optical density distribution obtained from the recorded pictures. The final atom number is given by the fitted atom number, rescaled according to

$$\begin{aligned} N_{\text{tot,Gauss}} &= \int n_{\text{Gauss}}(x,y,z)\ d^3r \\ &= 2\pi a \sigma_x \sigma_y / \left(\frac{4\pi}{\lambda} \cdot \frac{d_{\text{red}}^2}{2\varepsilon_0 \hbar \Gamma} \frac{1}{1+(\Delta/2\Gamma)^2}\right). \end{aligned} \quad (4.4)$$

For the analysis of absorption images of a BEC, the Thomas-Fermi profile integrated along one direction is fit to the imaged integrated OD to receive the detected atom number

$$N_{\text{detected,TF}} = \int\int a \left[1 - \frac{x^2}{R_x^2} - \frac{y^2}{R_y^2}\right]^{3/2} dx\ dy = \frac{2\pi}{5} a R_x R_y \quad (4.5)$$

(see also App. B.2). The amplitude a and the Thomas-Fermi radii R_x, R_y are extracted from the 2D fitting procedure of the mathematical expression in the integral to the optical density distribution. The total number of atoms in the cloud is found according to

$$\begin{aligned} N_{\text{tot,TF}} &= \int n_{\text{TF}}(x,y,z)\ d^3r \\ &= \frac{2\pi}{5} a R_x R_y / \left(\frac{4\pi}{\lambda} \frac{d_{\text{red}}^2}{2\varepsilon_0 \hbar \Gamma} \cdot \frac{1}{1+(\Delta/2\Gamma)^2}\right). \end{aligned} \quad (4.6)$$

In order to avoid saturation of the picture, the laser needs to be detuned by $\Delta = 2\pi \times (-4\,\text{MHz})$ to $\Delta = 2\pi \times (-10\,\text{MHz})$ depending on the size of the BEC.

4.4.2 Phase contrast imaging of the density distribution

When the cloud is imaged in-situ in the magnetic trap, its optical density on resonance is too high such that the absorption typically saturates. One method to avoid this saturation effects and image an object of high OD is phase contrast imaging: The imaging beam is detuned with respect to the $\left|5\mathrm{S}_{1/2}, F=2, m_F=2\right\rangle$ to the $\left|5\mathrm{P}_{3/2}, F'=3\right\rangle$ transition at 780.247 nm by a large detuning of +500 MHz resulting in no considerable absorption but still significant dispersion of the light by the cloud. After the beam has traversed the cloud it is focused through a phase plate[6] which has a 100 µm diameter dip in the center leading to a phase shift of $\pi/2$. The light which is scattered by the BEC does not experience this $\pi/2$ phase shift, such that interference between the scattered and unscattered light creates the phase contrast image on the camera. For details see Ref. [113]. The imaging setup is sketched in Fig. 4.10, where the propagation of the imaging beam (blue) is marked in contrast to the propagation of the light scattered by the BEC (red). The asphere in the bottom of our electric field compensation box has a numerical aperture of NA= 0.55 to achieve a high-resolution image. In combination with the choice of subsequent lenses in the imaging path, this allows for a magnification of 44 at the CCD camera (Andor iXon Ultra 897). To record a picture, the cloud is illuminated for 10 µs along the z-axis.

As introduced, when phase contrast imaging is performed the properties of the atomic cloud are obtained from the dispersion of the light introduced by the atoms which is measured by interference of this light with background light. Thereby, not the real but the imaginary part n'_{ref} of the refractive index is accessed from the phase shift distribution [120]

$$\Phi = \frac{1}{2}\left(\frac{I}{I_0} - 1\right) = \frac{4\pi}{\lambda} n'_{\mathrm{ref}}. \tag{4.7}$$

This formula is only valid if the transmission through the cloud is close to unity, the refractive index is small and the phase plate provides $\pi/2$ phase shift. As we perform phase contrast imaging with linearly polarized light propgating perpendicular to the magnetic field axis (see Fig. 4.3), π-transitions from $\left|5\mathrm{S}_{1/2}, F=2, m_F=2\right\rangle$ to both $\left|5\mathrm{P}_{3/2}, F'=2, m'_F=2\right\rangle$ and $\left|5\mathrm{P}_{3/2}, F'=3, m'_F=2\right\rangle$ are driven. Therefore, we have to consider the two electric dipole matrix elements which are given by the reduced matrix element $d_{\mathrm{red}} = |\left\langle J=1/2\right| |er| \left|J'=3/2\right\rangle| = 4.227 e a_0$ multiplied by $\sqrt{1/6}$ and -$\sqrt{1/6}$,

---

[6] Fused silica substrate PW-2008-UV, refractive index: 1.454 at 780 nm, from Laser Components GmbH. Phase plate custom made by Holoeye: 430 nm deep dip resulting in $\pi/2$ phase shift.

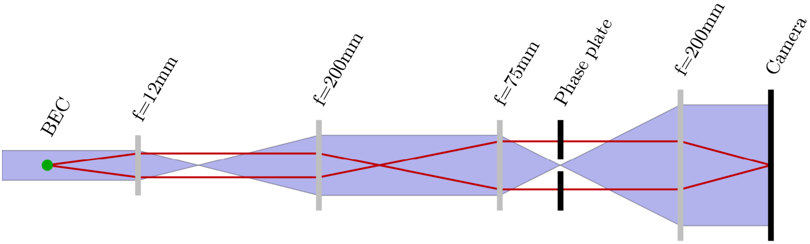

Fig. 4.10: Schematic illustration of the phase contrast imaging system. The blue shaded region indicates the spacial extent of the imaging beam while the red lines represent the propagation of the light scattered by the BEC (green). Lenses are sketched as gray bars, the labels refer to their respective focal lengths.

respectively [79]. Thus, the imaginary part of the refractive index is given by

$$n'_{\mathrm{ref}} = n(x,y,z)\left[\frac{d_{\mathrm{red}}^2}{6\varepsilon_0\hbar\Gamma}\cdot\frac{-\Delta_{F=3}}{1+(\Delta_{F=3}/2\Gamma)^2}+\frac{d_{\mathrm{red}}^2}{6\varepsilon_0\hbar\Gamma}\cdot\frac{-\Delta_{F=2}}{1+(\Delta_{F=2}/2\Gamma)^2}\right]. \tag{4.8}$$

Here, $\Delta_{F=3}$ denotes the detuning of the laser with respect to the $F = 2, m_F = 2$ to $F' = 3, m'_F = 2$ transition, whereas $\Delta_{F=2}$ labels the one to $F' = 2, m'_F = 2$.

We extract the number of detected atoms in the BEC from the phase shift distribution integrated along one axis

$$N_{\mathrm{detected,TF}} = \int\int a\left[1-\frac{x^2}{R_x^2}-\frac{y^2}{R_y^2}\right]^{3/2} dx\ dy = \frac{2\pi}{5}aR_xR_y \tag{4.9}$$

(see also App. B.2). Again, we determine the amplitude a and the Thomas-Fermi radii R_x, R_y by a 2D fit of the mathematical expression in the integral of the phase shift distribution. By rescaling this detected atom number according to

$$\begin{aligned} N_{\mathrm{tot,TF}} = \frac{2\pi}{5}aR_xR_y/\Bigg(\frac{4\pi}{\lambda}\Bigg[&\frac{d_{\mathrm{red}}^2}{6\varepsilon_0\hbar\Gamma}\cdot\frac{-\Delta_{F=3}}{1+(\Delta_{F=3}/2\Gamma)^2}\\ &+\frac{d_{\mathrm{red}}^2}{6\varepsilon_0\hbar\Gamma}\cdot\frac{-\Delta_{F=2}}{1+(\Delta_{F=2}/2\Gamma)^2}\Bigg]\Bigg) \end{aligned} \tag{4.10}$$

we can retrieve the total atom number of the cloud.

5

Photo-association of Trilobite Rydberg molecules

Trilobite Rydberg molecules are exotic ultralong-range dimer molecules with a huge electric dipole moment. This enormous electric dipole moment makes them appealing candidates for research of polar systems (see section 1). Trilobite Rydberg molecules consist of a neutral ground-state atom which is bound to the highly excited electron of a Rydberg atom by electron-neutral scattering. Already the first theoretical study of ultralong-range Rydberg molecules by Greene et al. [36] predicted their existence. The constructive interference of high-L electronic Rydberg states at the position of the neutral perturber atom gives rise to the unusual permanent electric dipole moment of the molecule (see section 3.4.1) which can amount to tenthousands of Debye [36]. Usually, homonuclear molecules don't possess an electric dipole moment, as the electron probability density is distributed symmetrically between the two nuclei. In this case, the symmetry is broken as one electron is excited to the Rydberg state.

Direct photo-association of Trilobite Rydberg molecules is hindered as dipole selection rules don't provide coupling to the state lacking low-L character. An exception is cesium, where the non-integer part of the S-state quantum defect is small by coincidence. Thereby, the level spacing between the S-state and the neighboring hydrogenic manifold is small which leads to admixing of S-character to the Trilobite potential energy curve and therefore allows for photo-association in this special case [42].

However, as presented in this chapter which is based on Ref. [2], a more general pathway exists to photo-associate Trilobite Rydberg molecules, making use of resonant coupling of the electron's orbital motion to the nuclear spin of the neutral perturber atom. For a particular principal quantum number the hyperfine splitting for the neutral atom matches the energy gap between the high-L Trilobite state and the optically accessible S-state. This resonance allows to form a hybrid potential energy curve consisting of the Trilobite state and the molecular S-state, offering the possibility to optically address the hybrid molecular state and providing a significant electric dipole moment. This novel method is applicable for many atomic species and is demonstrated here for the case of ^{87}Rb, where this resonant spin-orbit coupling gets efficient for $n = 50$.

Photo-association spectra are presented and compared to theoretical predictions based on the calculation of Born-Oppenheimer potential energy curves, as discussed in section 3.4. In the model, s- and p-wave electron-neutral scattering between the Rydberg electron and the neutral perturber atom is taken into account for both the singlet and triplet scattering channel, as well as the hyperfine interaction in the perturber atom. In addition, the electric dipole moment of the hybrid molecule is measured to be 135(45) D providing further evidence for the Trilobite character of the molecule.

5.1 Hybridized Trilobite Rydberg molecules

Rydberg electrons scatter with neutral ground-state atoms within the Rydberg orbit to form ultralong-range Rydberg molecules. Trilobite Rydberg molecular potentials stem from the s-wave scattering term for the Rydberg electron in (almost) degenerate energy levels of the hydrogenic manifold as introduced in detail in section 3.4.1. Such Trilobite Rydberg molecules can not be directly photo-associated by one or two-photon processes as they inherit their high-L character from the manifold states. In order to photo-associate a Trilobite Rydberg molecule, low-L character has to be admixed to their energy eigenstates. The full Born-Oppenheimer two-body potential energy curves U for the Rydberg atom interacting with one neighboring neutral atom are calculated based on the Hamiltonian

$$\begin{aligned}\hat{H}(\mathbf{r},R) =&\hat{H}_0 + \left[2\pi a_{\mathrm{s}}^{\mathrm{T}}(k(R))\hat{\mathcal{P}}_{\mathrm{T}} + 2\pi a_{\mathrm{s}}^{\mathrm{S}}(k(R))\hat{\mathcal{P}}_{\mathrm{S}}\right]\delta^3(\mathbf{r}-R\hat{\mathbf{z}})\\ &+ \left[6\pi a_{\mathrm{p}}^{\mathrm{T}}(k(R))\hat{\mathcal{P}}_{\mathrm{T}} + 6\pi a_{\mathrm{p}}^{\mathrm{S}}(k(R))\hat{\mathcal{P}}_{\mathrm{S}}\right]\delta^3(\mathbf{r}-R\hat{\mathbf{z}})\overleftarrow{\nabla}\cdot\overrightarrow{\nabla}\\ &+ A_{\mathrm{HFS}}\hat{\mathbf{S}}_2\cdot\hat{\mathbf{I}}_2\,, \end{aligned} \tag{5.1}$$

which is evaluated for a truncated basis[1] and diagonalized. Here, $\hat{H}_0$ is the Hamiltonian for the bare Rydberg atom including fine structure. The following four terms take care of the electron-neutral scattering for s- and p-wave scattering in the singlet (S) and triplet (T) scattering channel, depending on the respective scattering lengths $a_{\mathrm{s,p}}(k(R))$. The last term describes the hyperfine interaction in the neutral atom with the electronic spin $\mathbf{S}$ and the nuclear spin $\mathbf{I}$ of the neutral atom. While $\mathbf{r}$ refers to the distance between the Rydberg electron and the Rydberg nucleus, $\mathbf{R}$ denotes the position of the neutral atom with respect to the Rydberg ionic core. Variables with index 1 refer to the Rydberg atom and with index 2 to the neutral atom. A detailed discussion of the Hamiltonian including the characteristic features related to the terms is given in section 3. The ion-atom interaction term taken into account in that chapter is negligible for the atomic densities used in this chapter. Therefore, the term is omitted.

The lowest well of the Trilobite potential energy curves, calculated based on this Hamiltonian, is split by tens of GHz down to a few GHz with respect to the next lower lying nS Rydberg state for principal quantum numbers between 25 and 60. Only when this splitting gets comparable to the hyperfine splitting of 6.8 GHz, the singlet Trilobite potential can couple to the S-state potential of mixed singlet and triplet character (see section 3.4.3). This enables photo-association of hybrid Trilobite Rydberg molecules as it allows to admix low-L character to the Trilobite PEC. The resonant coupling is illustrated in Fig. 5.1, where Born-Oppenheimer potential curves are presented in the vicinity of the 40S, 50S and 60S state. All potentials corresponding to a nuclear spin of the neutral perturber atom of $F_2 = 2$ are marked in orange, while black PECs correspond to $F_2 = 1$.

For low n the hyperfine splitting between states with $F_2 = 1$ and $F_2 = 2$ is much smaller than the Rydberg level spacing between the S-state and the Rydberg states of the hydrogenic manifold (labeled m) which is shown for $n = 40$ in Fig. 5.1(a). In contrast, for high n it is different: The hyperfine

---

[1] For the PECs presented in this chapter for a certain state of interest, Rydberg states within +80 GHz to −140 GHz with respect to the state are taken into account. This corresponds to each two hydrogenic manifolds above and below the state of interest.

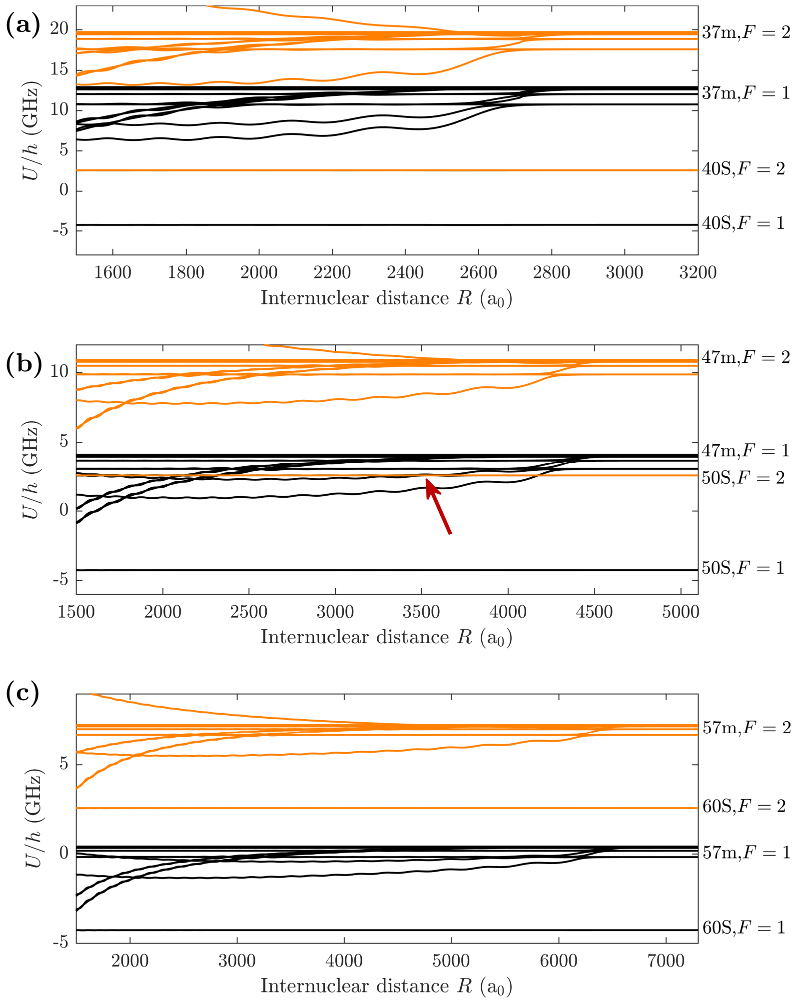

Fig. 5.1: Born-Oppenheimer potential energy curves U as a function of internuclear separation R in the vicinity of the 40S, 50S and 60S state. The energy of the bare nS Rydberg state is set to $U/h = 0\,\mathrm{GHz}$, respectively (a) For $n = 40$ the hyperfine splitting between $F_2 = 1$ and $F_2 = 2$ states is small in comparison to the level splitting between S- and manifold-states. (b) For $n = 50$ the splitting between the S-type and the Trilobite PEC is comparable to the hyperfine splitting leading to an avoided crossing at $R \approx 3500\,\mathrm{a}_0$, which is marked by a red arrow. (c) For $n = 60$ the hyperfine splitting is larger than the level spacing between S- and manifold-states.

splitting is still 6.8 GHz, but due to the relative level spacing decreasing according to n^{-3}, the splitting of the S-state to the Trilobite and manifold states is smaller than the hyperfine splitting which is shown at the example of the 60S state (see Fig. 5.1(c)). In between, for $n \approx 50$ the splitting between the Trilobite state and the S-state is comparable to the hyperfine splitting. A hybrid molecule can be excited, composed of the $50\mathrm{S}_{1/2}, m_{J_1} = -1/2, F_2 = 2$ state as well as the 47 Trilobite $F_2 = 1$ state.

In a pictorial way, one can understand this hybridization process in the following way: The $\downarrow_{\mathrm{rS}}\uparrow_{\mathrm{g}}$ molecular state can be photo-excited, where rS labels the electronic spin orientation of Rydberg S-state and g the nuclear spin orientation of the neutral atom in its electronic ground state. This state couples via mixed singlet and triplet scattering $\downarrow_{\mathrm{rS}}\uparrow_{\mathrm{g}} \pm \uparrow_{\mathrm{rT}}\downarrow_{\mathrm{g}}$ to the Trilobite Rydberg molecule state, referred to as rT, where the perturber atom has a flipped nuclear spin. By this spin-flip, energy of the nuclear spin is resonantly transferred to the orbital angular momentum of the Rydberg electron. Where the two potential energy curves meet, an avoided crossing arises due to the coupling, allowing to photo-associate molecules of both $\downarrow_{\mathrm{rS}}\uparrow_{\mathrm{g}}$ and $\uparrow_{\mathrm{rT}}\downarrow_{\mathrm{g}}$ character. The position of the avoided crossing is indicated in Fig. 5.1 by the red arrow.

The admixture of the Rydberg S-state to the Trilobite molecular potential is shown in Fig. 5.2. While the triplet Trilobite molecular potential curve crosses the 50S state without any coupling at 4188 a_0, the singlet Trilobite molecular potential curve, crossing at about 3500 a_0, couples strongly to the mixed S-type potential curve. Thereby, S-character is admixed to the Trilobite PEC. The S-character which is represented by the green shading of the PECs in Fig. 5.2 is calculated according to

$$P(\mathrm{S}) = \sum_{m_{J_1}, m_{S_2}, m_{I_2}} |\langle n = 50, L_1 = 0, J_1 = 1/2|\,\Psi\rangle|^2 \tag{5.2}$$

summing the square of the entries in the eigenvector corresponding to the contributions of the 50S Rydberg state to the molecular curve. Other S-states contribute only marginally. Molecular bound states can only be photo-associated if this S-character is sufficiently high.

The insets show the electron probability density for three representative internuclear separations to visualize how the hybrid character evolves with R. While the molecular state in the outermost well has an electron probability density which is almost identical to a Rydberg S-orbital, the electron probability density for the state crossing the S-state shows the characteristic shape of a Trilobite Rydberg molecule. Further in from the crossing, the electron

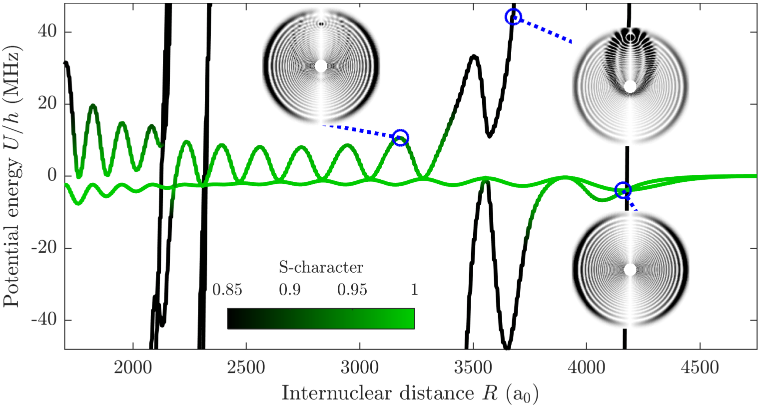

Fig. 5.2: Born-Oppenheimer potential energy curves U as a function of internuclear separation R. The $\left|50S_{1/2}, F_2 = 2\right\rangle$ state corresponds to $U/h = 0\,\mathrm{MHz}$. The hybridization of the 47m,$F_2 = 1$ singlet Trilobite PEC with the 50S,$F_2 = 2$ molecular potential is evident at $R \approx 3500\,a_0$. The S-character of the PECs is indicated by the green shading. The insets show the weighted electron probability density for the three positions of the PEC marked with blue circles.

probability density is still significantly distorted. The hybrid molecules photo-associated in this work, are bound at internuclear distances comparable to this position.

To quantify further how much the Trilobite character of the Born-Oppenheimer potential varies depending on the internuclear separation of the two atoms, not only the S-character of the adiabatic state is extracted but the state is decomposed into the different L_1-values. The angular momentum probability distribution of the Rydberg electron $P(L_1)$ is plotted in Fig. 5.3(a) for the potential energy curve exhibiting strong hybridization between the $n = 47$ Trilobite state and the 50S state (shown as a thick line in Fig. 5.3(b)) as a function of internuclear separation R. This illustrates which high-L orbital angular momentum states contribute to the shape of the electronic wave function of the hybrid Trilobite Rydberg molecule.

For values of R, were the radial wave function has nodes no admixture of other states to the state under consideration can take place - thus the hybridization vanishes. That shapes the behavior of $P(L_1)$ depending on R. To highlight this, the internuclear separations where the 50S wave function has a node are indicated by the white vertical lines. Further, the red lines

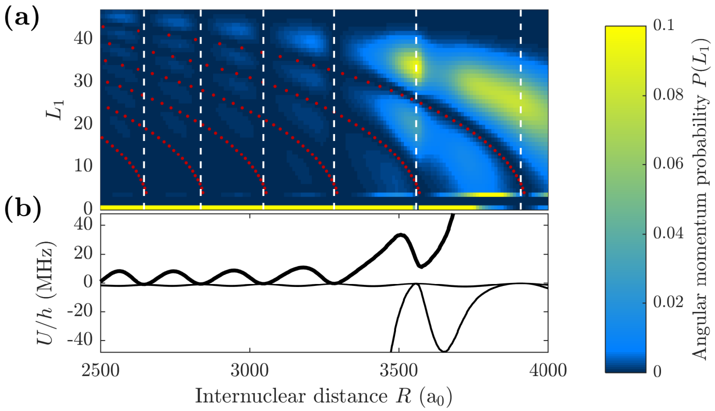

Fig. 5.3: Orbital angular momentum character of the hybridized ^{87}Rb Trilobite molecule. (a) Angular-momentum distribution $P(L_1)$ is presented as a function of the internuclear distance R for the hybridized Trilobite molecule in the vicinity of the 50S Rydberg state. The white dashed lines indicate the values of R for which the 50S-wave function has a node. The red dotted lines show the nodes of the $n = 47$ high-L wave functions. (b) Molecular potential energy U as a function of R in the vicinity of the 50S Rydberg state. The thick line shows the potential energy curve for which $P(L_1)$ is plotted in (a) (cf. Fig. 5.2).

mark the positions where the high-L_1 wave functions have their nodes. The number of nodes depending on n and L is discussed in section 2.2. It was also verified that the major contribution to the hybrid Trilobite potential stem from Rydberg states with principal quantum numbers $n = 50$ and $n = 47$.

As the ultracold cloud is held in a magnetic trap, we can not avoid magnetic offset fields in the experiment. In order to include these offset fields in the calculation of the potential energy curves the Hamiltonian accounting for the magnetic Zeeman effect (see section 2.3.2)

$$\hat{H}_B = \frac{\mathbf{B}}{2} \cdot (\hat{\mathbf{L}}_1 + g_S\hat{\mathbf{S}}_1 + g_S\hat{\mathbf{S}}_2 + g_I\hat{\mathbf{I}}_2) \tag{5.3}$$

is added to the Hamiltonian (Eq. 5.1) for the Rydberg atom interacting with the neutral perturber atom. While g_S is the electron spin g-factor, the nuclear spin g-factor is denoted by g_I. The PECs split according to the asymptotic Rydberg states which experience a different Zeeman effect. Also the coupling between the states is modified by the presence of the magnetic field $\mathbf{B}$.

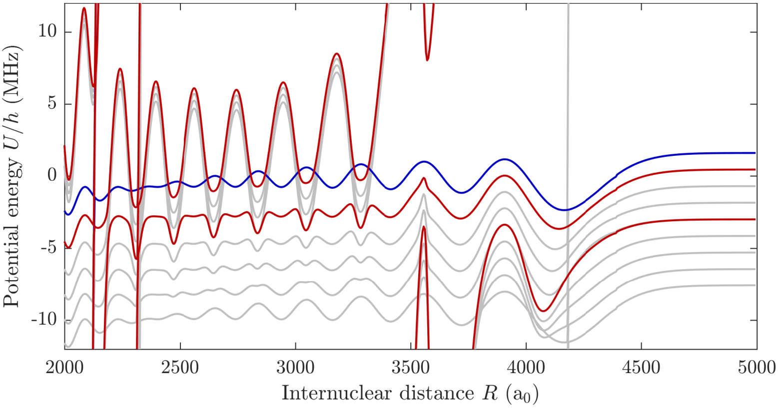

Fig. 5.4: Molecular potential energy curves in the vicinity of the 50S Rydberg state including an offset magnetic field (1.64 G) are presented as a function of the internuclear separation. The PECs are split due to the Zeeman effect. Curves with $m_K = 5/2$ $(3/2)$ are indicated with blue (red) lines. The grey lines correspond to PECs of different m_K, not relevant for this work. Zero energy corresponds to $\left|50\mathrm{S}_{1/2}, F_2 = 2, m_{F_2} = 2\right\rangle$.

The result of the full diagonalization of the Hamiltonian including the magnetic offset field is presented in Fig. 5.4, where the Born-Oppenheimer PECs in the vicinity of the 50S state are shown as a function of the internuclear distance between the Rydberg nucleus and the neutral ground-state atom. The magnetic offset field was set to 1.64 G for this calculation, corresponding to the value present in our experiment. One can identify 10 PECs associated with the $50\mathrm{S}_{1/2}, F_2 = 2$ asymptote which are split depending on their magnetic projection of the nuclear spin $m_{F_2} = \{-2, -1, 0, 1, 2\}$ and Rydberg electron spin $m_{J_1} = \{-1/2, +1/2\}$. Two of the asymptotes fall on top, as the $m_{F_2} = -2, m_{J_1} = 1/2$ Rydberg state experiences the same Zeeman shift as the $m_{F_2} = 2, m_{J_1} = -1/2$ state. PECs relevant for our experiment have $m_k = m_{J_1} + m_{S_2} + m_{I_2} = \{3/2, 5/2\}$ as the cloud is prepared in $F_2 = 2, m_{F_2} = 2$ where $m_{S_2} = 1/2$ and $m_{I_2} = 3/2$ and the Rydberg spin is $m_{J_1} = \pm 1/2$. The corresponding curves are marked in red ($m_k = 3/2$) and blue ($m_k = 5/2$), respectively.

For the calculation of the Born-Oppenheimer PECs in Fig. 5.4, the magnetic field is assumed to be parallel to the internuclear axis of the ultralong-range molecule. Generally, it is required to average the calculated spectra, received from the PECs, over all possible alignment angles between the internuclear axis and the magnetic field direction in order to model the experiment. This is necessary due to the fact, that the location of the neutral perturber atom is random for each experimental realization as the weak rotational splitting can not be resolved in the experiment. However, in the numerical calculations we found that the alignment angle between the field direction and the internuclear axis has only minor influence on all PECs relevant to this work. For S-type Rydberg states the PECs are even independent of that angle, which is indeed expected, as the S-type molecules are of Hund's case (b). Because of no angular momentum $L_1 = 0$ the orbital state is isotropic and has no alignment and the spins involved in the molecular problem S_1, S_2, and I_2 align with the magnetic field. For the Trilobite wave function the molecular binding is very strong (typically GHz) and decouples the orbital and intrinsic spins. The spins can therefore independently align with the magnetic field, while the Trilobite wave function is locked to the internuclear axis. Altogether, this means that the hybrid S- and Trilobite states in this work also do not depend on the alignment angle between internuclear axis and magnetic field.

5.2 Spectroscopy of Trilobite Rydberg molecules

In order to photo-associate Trilobite Rydberg molecules, an atomic sample of sufficiently high density is needed to ensure that a neighboring ground-state atom is located inside the Rydberg orbit. Additionally, the temperature needs to be low, as the molecules can break up due to its small binding energy, if there is too much kinetic energy. Therefore, the experiment starts with a sample of about 6.6×10^6 atoms at $1.2\,\mu\mathrm{K}$ with a peak density of $5.1 \times 10^{13}\,\mathrm{cm}^{-3}$, corresponding to the cooling ramp 3a, discussed in section 4.2. The atoms are prepared in the $F_2 = 2, m_{F_2} = 2$ hyperfine state, corresponding to $m_{S_2} = 1/2, m_{I_2} = 3/2$.

For the Rydberg excitation, a two-photon scheme is used. It involves σ^--polarized light at 420 nm ($1/e^2$ radius: 0.77 mm), which is off-resonant with respect to the transition from $\left|5\mathrm{S}_{1/2}, F = 2, m_F = 2\right\rangle$ to $\left|6\mathrm{P}_{3/2}, F = 3, m_F = 1\right\rangle$ by $\Delta = 830\,\mathrm{MHz}$ and is illuminating the full cloud, combined with a second laser beam at 1015.4 nm, driving π transitions to the $50\mathrm{S}_{1/2}, m_{J_1} = -1/2$ state (labeled $\downarrow$), which is focused to $2.1(3)\,\mu\mathrm{m}$. As discussed in section 4.3, there is still some residual coupling to the $m_{J_1} = +1/2$ Rydberg state (labeled $\uparrow$) for the Δ chosen. The magnetic offset field of 1.64 G points along the axial direction of our QUIC trap (see Fig 4.6), which allows us to spectroscopically resolve both m_{J_1} levels, due to their Zeeman splitting of $\delta = -4.6\,\mathrm{MHz}$. The excitation probability for the $\left|50\mathrm{S}_{1/2}\downarrow\right\rangle$ Rydberg states is about four times larger than for the $\left|50\mathrm{S}_{1/2}\uparrow\right\rangle$ component. The cloud is illuminated for 20 µs, leading to an average Rydberg excitation probability well below unity for the applied powers, in order to avoid Rydberg-Rydberg interactions (for details see sections 2.4 and 4.3.3). After Rydberg excitation, a strong electric field of 360 V/cm is applied in order to ionize the Rydberg atoms and accelerate the produced ions towards the channeltron detector. The channeltron detector was used despite of it lower detection efficiency as the MCP was broken and the data was taken before the rebuilt phase of the experiment in 2016.

The process of excitation, ionization and subsequent detection is repeated 1000 times at a rate of 2 kHz for each single atomic sample. As a consequence, the atom number decreases by $\approx 25\%$, while the cloud temperature slightly increases to 1.4 µK. To obtain Rydberg molecule spectra, as presented in Fig. 5.5, the aforementioned measurement sequence is repeated for different frequency detunings δ of the 1015.4 nm laser. Each data point is then an average over three such experimental runs and the exemplary errorbars represent the standard error extracted from 3000 pulses.

In Fig. 5.5 the mean ion count rate is depicted as a function of the laser detuning δ, where the frequency reference $\delta = 0\,\mathrm{MHz}$ corresponds to the transition to the $\left|50\mathrm{S}_{1/2}\uparrow\right\rangle$ Rydberg state. This transition doesn't shift in the magnetic field, as the Zeeman effect for the ground state and this Rydberg state is the same such that the effect on the transition frequency cancels. To compare the signal stemming from this Rydberg transition with the theoretical calculation of the previous section, the total spin projection has to be $m_K = 5/2$ (as $m_{J_1} = 1/2, m_{S_2} = 1/2, m_{I_2} = 3/2$). The strong transition to the $\left|50\mathrm{S}_{1/2}\downarrow\right\rangle$ Rydberg state at $\delta = -4.6\,\mathrm{MHz}$ is shifted due to the magnetic offset field and corresponds to $m_K = 3/2$. All other peaks arise due to the photo-association of ultralong-range Rydberg molecules. While conventional S-type Rydberg molecules have negative binding energies, in this spectrum a peak at $\delta = 4.2\,\mathrm{MHz}$ arises. We will later attribute it to the photo-association of hybridized Trilobite Rydberg molecule.

In order to identify the peaks in the spectrum, molecular bound states are calculated for the potential energy curves relevant for this work. Therefore, the PECs with $m_K = 3/2$ and $5/2$ are presented in Fig. 5.6(a) together with the absolute squared radial wave function of the vibrational molecular bound states $|\Phi_\nu(R)|^2$, which we calculate using the Numerov algorithm (the same way as for the radial wave functions of the Rydberg orbits). Bound states in the $m_K = 5/2$ (3/2) Born-Oppenheimer potential are marked in blue (red) and are offset by their respective binding energy. In Fig. 5.5 they

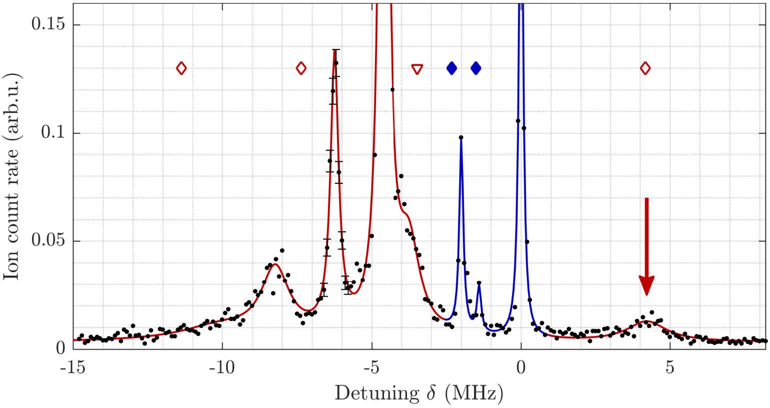

Fig. 5.5: Rydberg molecule spectrum showing the mean ion count rate as a function of laser detuning δ in the vicinity of the atomic Rydberg resonance $\left|50\mathrm{S}_{1/2}\uparrow\right\rangle$ (at $\delta = 0\,\mathrm{MHz}$). The red arrow marks the peak attributed to the photo-association of Trilobite Rydberg molecules. The magnetic offset field amounts 1.64 G. Representative error bars indicate the standard deviation. Solid lines are fits to the data based on a sum of multiple Lorentzians. Blue filled (red open) symbols indicate calculated binding energies of molecular states associated with PECs for which $m_K = 5/2$ ($m_K = 3/2$).

are marked with the corresponding blue (red) symbols and especially for the case of the PEC of pure triplet character ($m_K = 5/2$), the calculated binding energies show good agreement with the experimental data. Also for the $m_K = 3/2$ case, where the presence of the Trilobite potential modifies the PECs, the experimental results match the calculated binding energies considerably well. Note that the $m_K = 3/2$ state which is marked with the triangle is bound in a molecular potential which asymptotically connects to $\left|50\mathrm{S}_{1/2}\uparrow, F_2 = 2, m_{F_2} = 1\right\rangle$ state, which can not be excited in our experiment as the spin-polarized sample has $m_{F_2} = 2$. The mixed singlet and triplet scattering of the electron leads to some admixing of the other hyperfine state to the molecular state - the photo-association of this molecule induces a spin flip to $m_{F_2} = 1$ analogous to Ref. [47]. This allows for associating the molecular states, despite the fact that the asymptotic Rydberg level is not accessible in the experiment.

In order to identify the peak appearing at positive detuning, the calculated binding energies for the consecutively numbered bound states which are bound

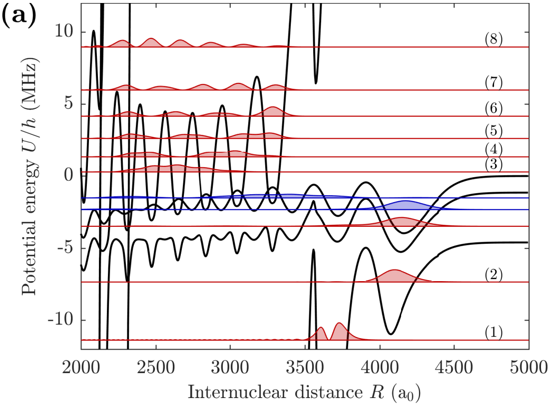

(b)

State	U_b/h (MHz)	d (D)
(1)	-11.4	2040
(2)	-7.4	101
(3)	0.3	45.5
(4)	1.3	71.4
(5)	2.6	98.4
(6)	4.2	117
(7)	6.0	121
(8)	9.0	174

Fig. 5.6: Bound states in the hybrid PECs of both Trilobite and S-type character. (a) Long-range molecular potentials U with $m_K = \{3/2, 5/2\}$ are presented in the vicinity of the 50S Rydberg state as a function of the internuclear separation. Calculated vibrational bound states $|\Phi_\nu(R)|^2$ are shaded in red (blue) depending, whether they are bound in the $m_K = 3/2$ (5/2) PEC and are offset by their respective binding energies U_b. Bound states with significant Trilobite admixture are numbered (1)-(8). Zero energy corresponds to the asymptote of the state $\left|50\mathrm{S}_{1/2}\uparrow, F_2 = 2, m_{F_2} = 2\right\rangle$ (b) Calculated binding energies U_b and dipole moments d for the vibrational bound states (1)-(8) in (a).

in the hybridized potential of both Trilobite and S-type character are listed in Fig. 5.6(b) together with their respective electric dipole moment d. The measured binding energy of $\delta = +4.2\,\mathrm{MHz}$ agrees with the state numbered (6) for this additional peak. States (3)-(5) do not show up as strongly as expected in the spectrum, but they very likely contribute to the offset signal at low positive detunings. Note that for state (6) a large portion of the radial wave function is located at relatively large internuclear separations such that the Franck-Condon factor can be considerably high. This is different for states (3)-(5). In addition, the expected lifetime of the molecular bound state (6) is reasonable and amounts $\tau = 1.8\,\mu\mathrm{s}$.

For the peak at $\delta = -8.4\,\mathrm{MHz}$, it is not clear what causes the deviation from the predicted peak position of state (1). As the following measurements of the electric dipole moment were performed before the bound states were calculated, we didn't consider this state for the measurement of the dipole moment.

5.3 Response to external electric fields

To gain further evidence that the unusual spectroscopic signal at blue detuning in Fig. 5.5 can be attributed to the photo-association of ultralong-range Rydberg molecules of hybrid Trilobite and S-character, its response to an external electric field is investigated. As the Trilobite Rydberg molecule possesses a huge electric dipole moment, one would expect that some electric dipole moment is admixed in the hybrid molecule as well. The expected strength of the dipole moment d along the z-axis, can be calculated according to

$$d = e \int |\Phi_v(R)|^2 \langle \Psi_{\mathrm{el}}(R)| \, \hat{z} \, |\Psi_{\mathrm{el}}(R)\rangle \, dR \, . \tag{5.4}$$

Here, $\Psi_{\mathrm{el}}(R)$ is the adiabatic electronic wave function at location R on the PEC of interest, which is obtained from our full diagonalization of $\hat{H}$: The eigenvector associated with the PECs eigenenergy at R delivers the weights for the Rydberg states making up the state $\Psi_{\mathrm{el}}(R)$. These R-dependent expectation values of the electronic dipole operator (along the **z**-direction) are weighted with the square modulus of the vibrational wave function of interest $\Phi_v(R)$ to find the weighted dipole moment for the states which are photo-associated in the experiment. The calculated dipole moments received for the hybrid Trilobite molecules are listed in Fig. 5.6(b). For state (6), a dipole moment of 117 D are expected.

To measure the electric dipole moment in the experiment, a homogeneous static electric field $\mathcal{E}$ is applied parallel to the magnetic field of the trap and spectra are recorded in the vicinity of the $\left|50\mathrm{S}_{1/2}\uparrow\right\rangle$ Rydberg state. In order to avoid any influence of possible field drift during the measurement, the sequence is slightly adapted: The full range of detunings δ is scanned for one atomic cloud in 200 steps ramping up and down in frequency 20 times which results in total in 4000 Rydberg excitation pulses per cloud. This is done for four different electric field values $\mathcal{E}$ for successively prepared clouds and the whole sequence is repeated such that each data point shows the average over 125 experimental runs. Thereby, one can avoid that possible drifts of electric stray fields systematically affect the measurement. Due to the increased number of excitation pulses per atomic cloud, the temperature is increased to 2.5 µK and the atom number decreases to 4.5×10^6 after the 4000 Rydberg excitation pulses.

The result of this measurement is presented in Fig. 5.7, where the mean ion count rate is shown as a function of laser detuning δ for a set of four electric fields $\mathcal{E}$. For the small electric fields applied which are only in the mV/cm

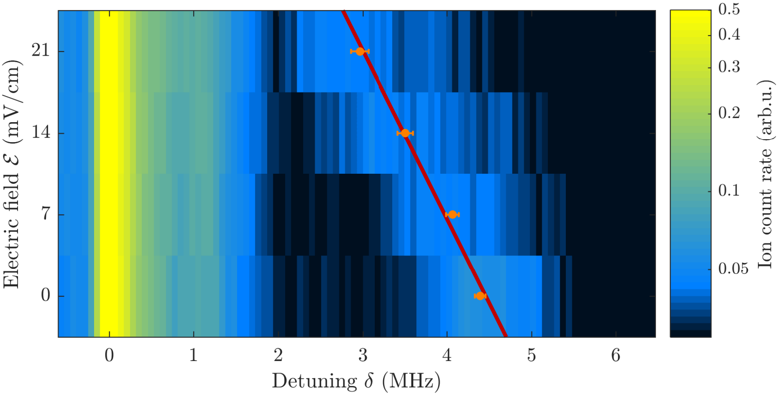

Fig. 5.7: Rydberg Stark map showing the mean ion count rate as a function of the laser detuning δ in the vicinity of the $\left|50\mathrm{S}_{1/2}\uparrow\right\rangle$ Rydberg state ($\delta = 0\,\mathrm{MHz}$ for the field free case) for four values of the electric field $\mathcal{E}$. Orange points depict the peak position of the blue detuned hybrid molecular state of Trilobite and S-character extracted from Lorentzian fits to the data. The red line is a linear fit to the peak positions, which yields an electric dipole moment of 135(45) D.

range, the atomic Rydberg transition to the $\left|50\mathrm{S}_{1/2}\uparrow\right\rangle$ state at $\delta = 0\,\mathrm{MHz}$ exhibits no noticeable Stark effect (see section 2.3.1). In contrast, the signal caused by the photo-association of hybrid Trilobite Rydberg molecules at $\delta = 4.2\,\mathrm{MHz}$ for no field, shifts by more than a MHz for an applied electric offset field of 21 mV/cm. The linear shift of the line with respect to the applied electric field reveals its large permanent electric dipole moment (and not an induced one) and confirms the assignment of the spectroscopic signal to the photo-association of hybrid Trilobite Rydberg molecules. The line centers for the different offset fields are extracted from Lorentzian fits to the line shape of the Trilobite signal and the results are plotted as orange points in Fig. 5.7. The electric dipole moment is extracted from this values by a linear fit (shown in red) and results in $d = h \times d\delta/d\mathcal{E} = 135(45)\,\mathrm{D}$. Within experimental uncertainties, this agrees with the theoretically predicted electric dipole moment of 117 D.

Note that conventional S-type ultralong-range Rydberg molecules, which feature only a small perturbative admixture of the Trilobite state, typically show a symmetric broadening of the molecular line relative to the atomic transition in response to electric fields [41]. This differs from what is observed here and hints at the need for a more elaborate theoretical description. One may speculate that it indicates a parallel orientation of the molecular state with respect to the electric field axis.

5.4 Tuning the spin-orbit coupling out of resonance

In section 5.1 it was discussed, that the coupling of the orbital angular momentum of the Rydberg electron to the nuclear spin of the neutral ground-state atom, which leads to the coupling of the Trilobite state to low-L Rydberg states depends crucially on the relative energy scale of the hyperfine splitting in comparison to the Rydberg level spacing and therefore the principal quantum number. In comparison to the 50S Rydberg state studied up to now, the strength of this coupling varies considerably with n for neighboring states.

For the case of the 49S state an increased Rydberg level spacing occurs and the singlet Trilobite PEC doesn't cross the S-type PEC, but passes about 50 MHz blue detuned. Although that energetic splitting is comparatively large, the curves of $m_K = 3/2$ couple considerably, leading to the lowering in energy of the Born-Oppenheimer curve with $49\mathrm{S}_{1/2}\downarrow, F_2 = 2, m_{F_2} = 2$. The potential energy curves for 49S are presented in Fig. 5.8(a) as a function of internuclear separation. In the experiment this is reflected by the broad wing at red detunings visible in the spectrum presented in Fig. 5.8(b), where the mean ion count rate is shown as a function of laser detuning δ in the vicinity of the transition to the $\left|49\mathrm{S}_{1/2}\uparrow\right\rangle$ state ($\delta = 0\,\mathrm{MHz}$). In contrast to the case of the 50S state in Fig. 5.8(e), no peak at blue detunings is visible at all for 49S. This is consistent with the calculated molecular bound states, which only show up at red detunings for 49S.

As discussed in detail in section 5.1, for 50S (Fig. 5.8(b)) the Trilobite PEC crosses the S-type PEC at $\approx 3500\,\mathrm{a}_0$, leading to a strong hybridization with the $m_K = 3/2$ state. This leads to the hybridized Trilobite molecules at blue detuning with respect to the atomic line, which are in agreement with the experimental observation (Fig. 5.8(e)).

In contrast, for 51S, the crossing of the Trilobite state with the S-state takes place at larger internuclear separations of about $4400\,\mathrm{a}_0$, which makes the outermost potential well of the S-type PEC with $m_{F_2} = 2$ and $m_K = 3/2$ open up. Therefore, no bound state exists in this PEC, which is in accordance with the measured spectrum presented in Fig. 5.8(f). There, no noticeable peaks show up at red detuning with respect to the $\left|51\mathrm{S}_{1/2}\downarrow\right\rangle$ state. As the energy gap between the Trilobite state and the S-state is not close to

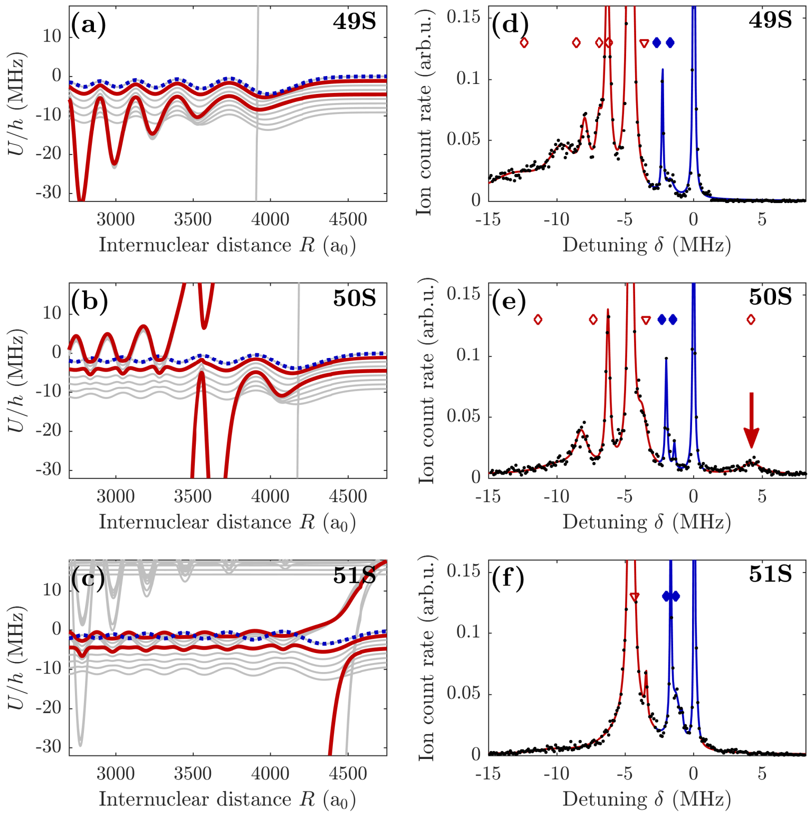

Fig. 5.8: (a)-(c) Ultralong-range molecular potentials U in the vicinity of the Rydberg states 49S (a), 50S (c), and 51S (c) as a function of internuclear separation R for a magnetic offset field of 1.64 G. Blue dotted (red solid) curves show PECs with $m_K = 5/2$ ($m_K = 3/2$). Grey lines indicate PECS of different m_K, not relevant for this work. Zero energy corresponds to the asymptotes of the states $\mathrm{nS}_{1/2} \uparrow, F_2 = 2, m_{F_2} = 2$ corresponding to $m_K = 5/2$. (d)-(f) Rydberg molecule spectra showing the mean ion count rate as a function of laser detuning δ in the vicinity of the atomic Rydberg states 49S (d), 50S (e), and 51S (f) at a magnetic offset field of 1.64 G. The zero of the frequency axis ($\delta = 0$ MHz) is referenced to the $n\mathrm{S}_{1/2} \uparrow$ atomic Rydberg level. Solid lines are fits to the data based on a sum of multiple Lorentzians. Blue filled (red open) symbols indicate calculated binding energies of molecular bound states associated with PECs for $m_K = 5/2$ ($m_K = 3/2$).

resonance with the hyperfine splitting in the ground-state atom anymore, the coupling is much weaker than for 50S and no hybrid molecules can be observed.

6

Ionic impurity in a Bose-Einstein condensate

The study of ion-atom interaction in the quantum scattering regime is a longstanding goal in experimental physics and many proposals exist for interesting novel research in this field (see section 1). Typically, ion-atom interaction at ultracold temperatures is investigated in hybrid systems, where an ultracold cloud is overlapped with an ion, trapped in a Paul trap [61, 64, 71–73, 121]. In Paul traps the ion can be centered in the trap at the beginning of the experiment and cooled to temperatures of hundreds or even tens of microkelvin. However, as soon as the ion starts to interact with neighboring atoms and slightly deflects from the trap center, it heats up due to its micromotion in the radio-frequency ion trap. Therefore, the temperature for such hybrid systems is usually limited to the millikelvin regime [74], far above the s-wave quantum scattering limit. Mixtures with favorable mass ratios, might allow to reach the quantum scattering regime in the future [122, 123]. As an alternative method, optical trapping of ions has recently been demonstrated, but controlled mixing with ultracold atoms remains an open challenge [75, 76], as the optical trapping laser also forms a potential for the atoms.

In this chapter, which is based on Ref. [1], a novel approach is presented which allows the study of ion-atom interaction for the core of a giant Rydberg atom immersed in a BEC of ^{87}Rb. The Rydberg nucleus is located in a dense micro-BEC where a small interparticle separation leads to ion-atom interaction in the MHz regime. As the Rydberg atom is excited from a condensed sample the ultralow temperature environment of the parent atomic ensemble is maintained. The kinetic energy of the Rydberg atom is slightly increased due to the photon-recoil of the Rydberg excitation which amounts $k_\mathrm{B} \times 730\,\mathrm{nK}$ for our experiment. Hence, the interaction of the BEC with the Rydberg ionic core is studied at temperatures below a microkelvin, which is about three orders of magnitude lower compared to what has been achieved in hybrid traps [124, 125]. Yet, our system temperature is still above the s-wave scattering limit, which for Rb is $E^* = k_\mathrm{B} \times 78.9\,\mathrm{nK}$ (see section 3.2). Note that the potential barrier for f-wave scattering amounts to $2.84\,\mu\mathrm{K}$, such that in our system only s-, p- and d-wave scattering contributes. A striking advantage of the method is that rapid acceleration of the ionic impurity due to detrimental electric stray fields is prevented by the Rydberg electron which provides an effective shielding.

By exciting Rydberg states with principal quantum numbers up to $n = 190$, a setting can be prepared, in which the Rydberg electron orbit largely exceeds the BEC size. Thereby, the typically dominant electron-atom interaction is suppressed due to the reduced overlap of the electron probability density and the atomic sample. The reduction of the electron-atom interaction is revealed by Rydberg spectra recorded for increasing principal quantum numbers. The comparison of the Rydberg excitation spectra at high n to our theoretical model unravels the contribution of the ion-atom interaction to the observed line shape. In addition, the collisional lifetime of the Rydberg excitation in the dense sample is measured.

6.1 Concept to study the ion-atom interaction between a Rydberg nucleus and a neutral atom

A Rydberg atom excited in a dense and ultracold sample interacts with neighboring neutral atoms via ion-atom and electron-atom interaction. As detailed in section 3, the ion-atom interaction is treated classically and described by the polarization potential $V_\mathrm{i} = -C_4/R^4$. In contrast, the electron-atom interaction is treated quantum mechanically as a contact interaction, where s- and p-wave scattering contributes in the singlet and triplet scattering channel. For the work presented in this chapter nS Rydberg states with $m_J = +1/2$[1] are addressed and as the BEC is prepared in the $F = 2, m_F = 2$ state, only triplet scattering needs to be considered. A full diagonalization of the Hamiltonian

$$\begin{aligned}\hat{H}(\mathbf{r}, R) =& \hat{H}_0 + \hat{H}_{\mathrm{sc,e}} + \hat{H}_i \\ =& \hat{H}_0 + 2\pi a_{\mathrm{s}}(k(R))\ \delta^3(\mathbf{r} - R\hat{\mathbf{z}}) \\ &+ 6\pi a_{\mathrm{p}}(k(R))\ \delta^3(\mathbf{r} - R\hat{\mathbf{z}}) \overleftarrow{\nabla} \cdot \overrightarrow{\nabla} - \frac{C_4}{R^4} \end{aligned} \tag{6.1}$$

evaluated for a truncated basis[2] yields the two-body Born-Oppenheimer potential energy curves $U_{\mathrm{i,e}}$ (PEC) (see chapter 3). Here, $\hat{H}_0$ denotes the Hamiltonian of the bare Rydberg atom including fine structure. The second and third term comprise the triplet s- and p-wave scattering of the Rydberg electron at $\mathbf{r}$ interacting with the neutral atom at $\mathbf{R}$. It depends on the respective scattering length $a_{\mathrm{s,p}}(k(R))$. Finally, as already introduced, the last term refers to the ion-atom interaction potential V_{i}. The Hamiltonian and the characteristic features in the two-body potential energy curves $U_{\mathrm{i,e}}$ related to its terms are discussed in detail in chapter 3. The label (i,e) indicates, that both the contribution of the ion and the electron is taken into account.

The interaction between the ionic Rydberg core and the neutral atom dominates only for very small internuclear separations. This is presented in Fig. 6.1, where in the upper panel the inner part of the interaction potential $U_{\mathrm{i,e}}$ (black) is shown as a function of internuclear separation R for the Rydberg 190S state. For comparison, the potential U_{e} is presented (red) for which the last term in Eq. 6.1 is omitted. The two potential energy curves $U_{\mathrm{i,e}}$ and U_{e} differ significantly for small internuclear separations of $\approx 1000\,\mathrm{a_0}$. In this regime the C_4-term gets considerable. Note, that the divergence at $1700\,\mathrm{a_0}$ is caused by the shape resonance in the triplet p-wave scattering channel.

In order to find signatures of the ion-atom interaction for the Rydberg nucleus interacting with a neutral atom, are small nearest neighbor spacing is required. Thereto, the density of the BEC needs to be increased dramatically in comparison to typical ultracold experiments with ^{87}Rb. In our experiment, this is achieved by the use of a tight micro-trap. To illustrate how the experiment meets this requirement the nearest neighbor ($N = 1$), next nearest neighbor ($N = 2$) and next-next nearest neighbor distribution ($N = 3$)

---

[1] The m_J quantum number is $+1/2$ throughout this chapter and is not explicitly stated anymore.

[2] One hydrogenic manifold above and one below the state of interest were taken into account. We numerically tested, that taking one or two more manifolds into account does not significantly change the calculated Rydberg spectrum.

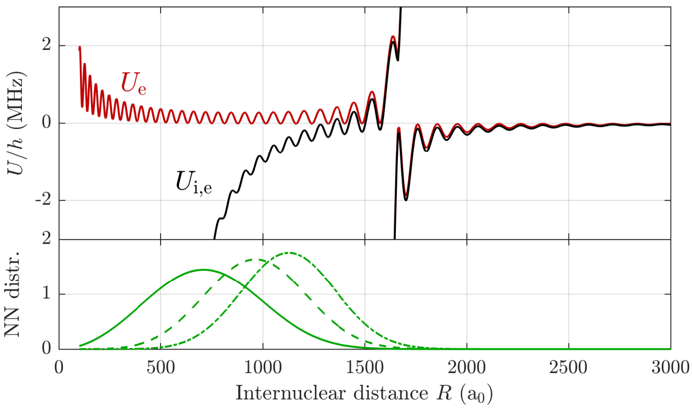

Fig. 6.1: The potential energy curves $U_\mathrm{i,e}$ (black) and U_e (red) are presented as a function of internuclear distance R in the vicinity of the $190\mathrm{S}_{1/2} + 5\mathrm{S}_{1/2}$ asymptote (at $U/h = 0\,\mathrm{MHz}$). While U_e only accounts for the electron-atom interaction, $U_\mathrm{i,e}$ also includes the interaction with the Rydberg core ion. In the lower panel, nearest (solid), next nearest (dashed), and next-next nearest (dash-dotted) neighbor distributions are depicted for a typical peak density of $\rho = 3 \times 10^{15}\,\mathrm{cm}^{-3}$.

according to [126]

$$p_N(R) = \frac{3}{(N-1)!}\left(\frac{4\pi\rho}{3}\right)^N R^{3N-1}\exp\left(-\frac{4\pi\rho}{3}R^3\right) \tag{6.2}$$

are of interest. These distributions are presented in the lower panel of Fig. 6.1 for the peak density of $\rho = 3 \times 10^{15}\,\mathrm{cm}^{-3}$ of our experiment. The nearest neighbor distribution peaks at $\approx 700\,\mathrm{a}_0$, where $U_\mathrm{i,e}$ and U_e show a deviation of more than 4 MHz.

However, for such a high density, many neutral atoms are located inside the Rydberg orbit and the electron-atom interaction typically dominates the effect of the ion-atom interaction by far. For large internuclear separations the PEC $U_\mathrm{i,e}$, which is presented in Fig. 6.2 as a function of internuclear separation R, is fully dominated by the electron-atom interaction. The potential energy curve resembles the electron probability density. As the size of the Rydberg orbit increases with the principal quantum number, the range of the potential increases accordingly. In our experiment, a BEC is prepared (depicted by the green shaded area in Fig. 6.2) for which the radial extent is significantly smaller than the range of the interaction potential for large n. Thereby,

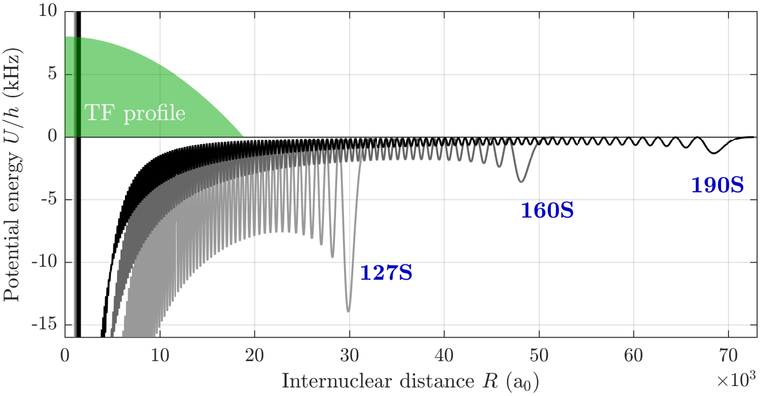

Fig. 6.2: The full spatial range of the potential energy $U_{\mathrm{i,e}}$ is shown for three principal quantum numbers as a function of internuclear separation R. Zero energy is set to the respective asymptotic $\left|n\mathrm{S}_{1/2}\right\rangle$ Rydberg state. For comparison the spatial extent of the BEC Thomas-Fermi profile (green) along the short trap axis is indicated.

the reduced overlap between the large Rydberg orbit and the BEC can be employed to suppress the dominant effect of the electron-atom interaction. Note, that the potential wells at large internuclear separations are in the kHz range, while the contribution of the C_4-term illustrated in Fig. 6.1 at internuclear distances corresponding to the typical particle spacing is in the MHz range.

In summary, our approach to study the ion-atom interaction is based on the combination of a very dense and small BEC with a Rydberg excitation of very high principal quantum number. This allows us to achieve a sufficiently small nearest neighbor spacing to increase the contribution of ion-atom interaction, while reducing the electron-atom interaction due to the small extent of the ultracold cloud in comparison to the Rydberg orbit size.

6.2 A Rydberg atom interacting with many atoms in a dense micro-BEC

The experiments presented in this chapter aim to observe the effect of the ion-atom interaction on the Rydberg excitation spectrum. Therefore, a theoretical model for the line shape of the Rydberg excitation spectrum is necessary which can be compared to the experimental results. This can finally enable us to disentangle the contributions of the electron-atom and ion-atom interaction contributing to the full line shape.

In order to model the line shape, one has to be aware that for a single Rydberg atom within a high density BEC, not only a single neutral atom is located inside the Rydberg orbit, but up to several thousands are. This raises the question to what extent it is suitable to apply the two-body interaction potential for each neutral atom independently. In our experiment, the Rydberg atom is excited to a nS Rydberg state, which is non-degenerate. Therefore, the admixture of other Rydberg states to the S-state due to the presence of the neutral atom is small and such is the modification of the S-orbital. This modification even decreases for increasing principal quantum number. At $n = 160$ it amounts to $\int [1 - P(\mathrm{S})]\rho \, d^3r \approx 2 \times 10^{-5}$, with $P(\mathrm{S})$ being the S-character of the S-type Born-Oppenheimer potential energy curve and ρ the normalized BEC density distribution used in the work presented in this chapter. The fact that the modification of the S-orbital is small implies that the potential for one atom in the Rydberg orbit is not changed by the presence of another atom. This allows us to employ the pairwise interaction potential, even for the case where many ground-state atoms are interacting with the same Rydberg atom.

For modeling the presence of many neutral atoms interacting with the Rydberg atom, we follow the treatment developed in Refs. [6, 110, 115]. In order to calculate the expected spectral line shape for the Rydberg excitation, a Monte-Carlo sampling approach is applied. It treats the atoms in the BEC as point-like particles of infinite mass that are randomly distributed within the range of U according to the Thomas-Fermi density distribution of the micro-BEC. The latter is known from independent measurements of atom numbers and trap frequencies. The atoms are assumed to have uncorrelated positions, as expected for a weakly interacting BEC.

One of the atoms is designated to carry the single Rydberg excitation. For each of the remaining atoms, the potential energy u_i is extracted from the interaction potential U according to its distance R to the Rydberg ionic core. The sum over the u_i delivers the energy shift U_n for a single Monte-Carlo configuration. The spectrum is obtained from the contributions of all U_n, weighted by the local excitation probability of the corresponding Rydberg atom. This probability is given by the intensity distribution of the 1020 nm excitation laser. Additionally, the contributions are convoluted with a Lorentzian profile reflecting the Rydberg excitation Fourier limited bandwidth. Note that the exact shape of the beam profile of the excitation

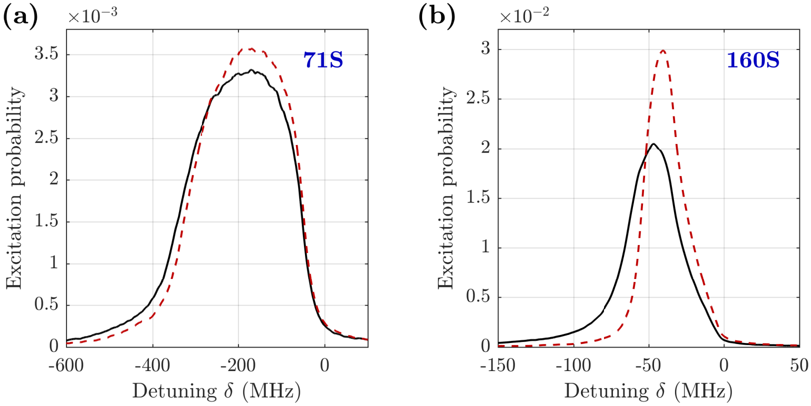

Fig. 6.3: Modeled Rydberg excitation spectrum for $\rho_{\text{peak}} \approx 3 \times 10^{15}\,\text{cm}^{-3}$ at $\left|71\text{S}_{1/2}\right\rangle$ in (a) and $\left|160\text{S}_{1/2}\right\rangle$ in (b). The normalized excitation probability is presented in black (red) based on the interaction potential $U_{\text{i,e}}$ including (U_{e} excluding) the contribution of the ionic core. The excitation probability is a depicted as a function of detuning δ with respect to the bare atomic Rydberg resonance at $\delta = 0\,\text{MHz}$.

laser has minor influence on the spectral shape due to the small sample size. Typically, 5×10^5 realizations are sampled for obtaining the modeled excitation spectrum. The area below the spectrum is finally normalized for comparison to the experimental data.

An exemplary spectrum is presented in Fig 6.3(a), for the case of a $\left|71\text{S}_{1/2}\right\rangle$ Rydberg state, excited in a micro-BEC of ≈ 47850 atoms with trap frequencies $\omega_r = 2\pi \times 2442\,\text{Hz}$ and $\omega_a = 2\pi \times 268\,\text{Hz}$. This corresponds to a peak density of about $3 \times 10^{15}\,\text{cm}^{-3}$ alike the peak density in the experiment. The more particles are found within the Rydberg orbit, the more energy values u_i contribute to the overall detuning U_n required to resonantly excite the Rydberg atom in this environment. Therefore, a larger detuning δ is generally required to excite a Rydberg atom in a high density environment compared to a low density environment. As long as the Rydberg orbit is significantly smaller than the BEC, the mean shift of the spectrum is, to first order, independent of n. This is the result of the electron probability density being normalized. More specifically, if the principal quantum number is increased, the orbit volume increases as (n^6) and so does the number of atoms inside. At the same time, due to the normalization of the electron probability density, the potential depth is getting shallower proportional to n^{-6}. This compensates for the increased number of perturber atoms contributing, such that the overall line shift is the same. In this regime, the line shift and broadening mainly depends linearly on the background density. In first approximation, taking only the s-wave scattering into account and neglecting the k-dependence of the scattering length, one can quantify the mean shift of the Rydberg line as

$$\Delta E_{\mathrm{mean}} = 2\pi a_{\mathrm{s}}^{T}(0)\rho, \tag{6.3}$$

as discussed in Ref. [56]. This formula is only applicable as long as the Rydberg orbit is significantly smaller than the size of the micro-BEC. However, once the Rydberg orbit exceeds the size of the micro-BEC, the electron-atom interaction is suppressed due to the reduced number of atoms interacting with the Rydberg electron. Therefore, the spectrum narrows although the center density is high. This can be seen at the example of the spectrum for $\left|160\mathrm{S}_{1/2}\right\rangle$ presented in Fig. 6.3(b), which is narrowed significantly in comparison to the case of $\left|71\mathrm{S}_{1/2}\right\rangle$ shown in (a).

Note that there is no perfect mapping between the local density and the required detuning [3] for a Rydberg excitation in this environment: If a single neutral atom is located close to the p-wave resonance, it can contribute with a large negative or positive shift u_i to the overall detuning U_n required to excite a Rydberg atom in such a configuration of neighboring atoms. This is the reason for the non-vanishing signal at extreme negative and at positive detunings δ in Fig. 6.3(a). For increasing n this effect reduces [6].

Previously, Rydberg excitation in ultracold experiments has been investigated in density regimes, for which the presence of numerous atoms within the Rydberg orbit, leads to significant broadenings and line shifts of the Rydberg spectroscopy line [6, 56, 57]. The ion-atom interaction was negligible as the Rydberg orbit was not exceeding the Thomas-Fermi radius of the BEC. In this regime, the model described above has been successfully applied, revealing the impact of the p-wave shape resonance on the line shape [6]. Moreover, this semi-classical sampling method has been shown to reproduce a full quantum mechanical treatment based on a functional determinant approach at sufficiently large densities [49, 127]. This holds for our system parameters and also when including the ion-atom interaction [128].

The ion-atom interaction is independent of the principal quantum number n and thus only depends on the density of the sample, which controls the nearest neighbor spacing. This can be seen by comparing a spectrum modeled based on $U_{\mathrm{i,e}}$ which includes both ion-atom interaction and electron-atom interaction as presented in black in Fig. 6.3 and a spectrum based on U_e, where the ion-atom interaction is neglected as presented in red. The contribution of the ion-atom interaction to the overall line broadening and shift is approximately the same for 71S and 160S as the density distribution of the BEC is the same and for our experimental parameters amounts $\approx 5\,\mathrm{MHz}$. Obviously, it is favorable to investigate the ion-atom contribution at 160S as the relative effect in comparison to the overall line broadening is much more pronounced.

6.3 Evidence for ion-atom interaction at submicrokelvin temperature

In order to access the ion-atom interaction, as a first step the suppression of the electron-atom interaction is demonstrated experimentally. The very first onset of this effect has been previously observed in Ref. [56]. In our experiment, a BEC of about 6×10^5 Rubidium-87 atoms with a temperature below 250 nK is prepared in the QUIC trap (corresponding to ramp 3b in section 4.2). The optical microtrap (wavelength 855 nm, Gaussian waist $\approx 1.8\,\mu\mathrm{m}$) is ramped on linearly within 10 ms and a subsequent ramp of the magnetic offset fields (taking 10 ms) shifts the parent BEC aside, leaving typically 6.5×10^4 atoms in the micro-BEC. For the trap frequencies of $\omega_r = 2\pi \times 2180(60)\,\mathrm{Hz}$ and $\omega_a = 2\pi \times 215(30)\,\mathrm{Hz}$ this results in a peak density of $\approx 3 \times 10^{15}\,\mathrm{cm}^{-3}$. The Thomas-Fermi radii amount about $R_r = 1.0\,\mu\mathrm{m}$ and $R_a = 9.2\,\mu\mathrm{m}$. When the tweezer is switched off, and the micro-BEC expands in the magnetic trap, an upper temperature limit 250 nK can be found. The lifetime of the micro-BEC in the trap amounts to 19.5 ms and is limited by three-body loss.

A single Rydberg atom is excited from the micro-BEC, which is spin-polarized in the $\left|5\mathrm{S}_{1/2}, F = 2, m_F = 2\right\rangle$ state, to an $\left|n\mathrm{S}_{1/2}, m_J = 1/2\right\rangle$ Rydberg state by two-photon excitation. The excitation couples to the intermediate state $\left|6\mathrm{P}_{3/2}, F = 3, m_F = 3\right\rangle$ offresonantly with a single-photon detuning of $\Delta = 80\,\mathrm{MHz}$. The laser beam at 420 nm illuminates all atoms. In contrast, the second beam at 1020 nm is focused through the same aspheric lens as the beam providing the optical tweezer trap. Thereby, Rydberg atoms can only be excited in the micro-BEC but not in the parent BEC which was shifted aside. The recoil energy transferred during excitation amounts to $k_\mathrm{B} \times 730\,\mathrm{nK}$. The excitation pulses take 500 ns each. Exceptionally, for the datasets recorded at $n = 40$ and 71 pulses of200 ns duration are applied due to the shorter collisional lifetime in the dense sample. Each excitation pulse is followed by electric field-ionization and detection (efficiency $> 40\%$) of the produced ion on a microchannel plate detector. This procedure is repeated five times with a repetition rate of 20 kHz in the same atomic sample. To avoid any Rydberg-Rydberg interaction, the ion count rate is kept well below one (< 0.3 ions/pulse). Rydberg spectra are obtained by variation of the two-photon detuning δ and averaging over at least 75 realizations. For high-n Rydberg states of $n > 127$ we account for diamagnetic line shifts (see sections 2.3 and 4.3.4) that arise due to the magnetic field ramps to a final value of 7.73 G during sample preparation. For more details on the experimental setup see chapter 4.

The results of such measurements for increasing principal quantum number n are presented in Fig. 6.4. For low principal quantum numbers, the spectra exhibit the expected huge shift and broadening as discussed in the previous section. As the Rydberg orbit size of both the 41S and the 71S state is considerably smaller than the Thomas-Fermi radii of the micro-BEC, the corresponding Rydberg spectra show about the same line shift which is comparable to the shift $\Delta E_{\text{mean}} = -289\,\text{MHz}$, obtained from the very simple model in Eq. 6.3.

However, for increasing principal quantum number, the spectrum narrows down and shifts to smaller detunings. This follows the prediction of our model introduced in the previous section and is caused by the decreasing overlap of the Rydberg orbit with the atomic cloud. The dimensions are sketched in the inset of Fig. 6.4; for $n = 190$ the Rydberg orbit has a radius of $\approx 3.7\,\mu\text{m}$ in contrast to the Thomas-Fermi radius of $R_r = 1.0\,\mu\text{m}$ along the short trap axis. The Rydberg spectra show an increased offset signal for increasing principal quantum number. The increase is linked to the higher laser power that is needed to photo-excite the high-n Rydberg states. The offset signal can partly be attributed to the combination of the 420 nm Rydberg laser and the 855 nm trap laser as photo-ionization takes place through coupling to the intermediate state.

The line shift expected from the full numerical model is marked with grey diamonds and follows the data nicely. Both the experimental line center as well as the line width is extracted from a Gaussian fit to the data, which is indicated by the solid lines in Fig. 6.4. A constant offset is included in the fitting procedure to account for the background ion count rate in the spectra. The choice of a Gaussian is justified as the functional determinant approach predicts a Gaussian envelope for the Rydberg excitation in the BEC [49]. Although, the ion-atom interaction causes an additional red shift of $\approx 5\,\text{MHz}$ to the line center, the effect on the spectral width is more prominent.

In Fig. 6.5 the extracted Gaussian line widths σ are presented and compared to the simulated line widths based on $U_{\text{i,e}}$ (U_{e}) depicted in black (red). The data clearly follows the prediction of the model, where both ion-atom and

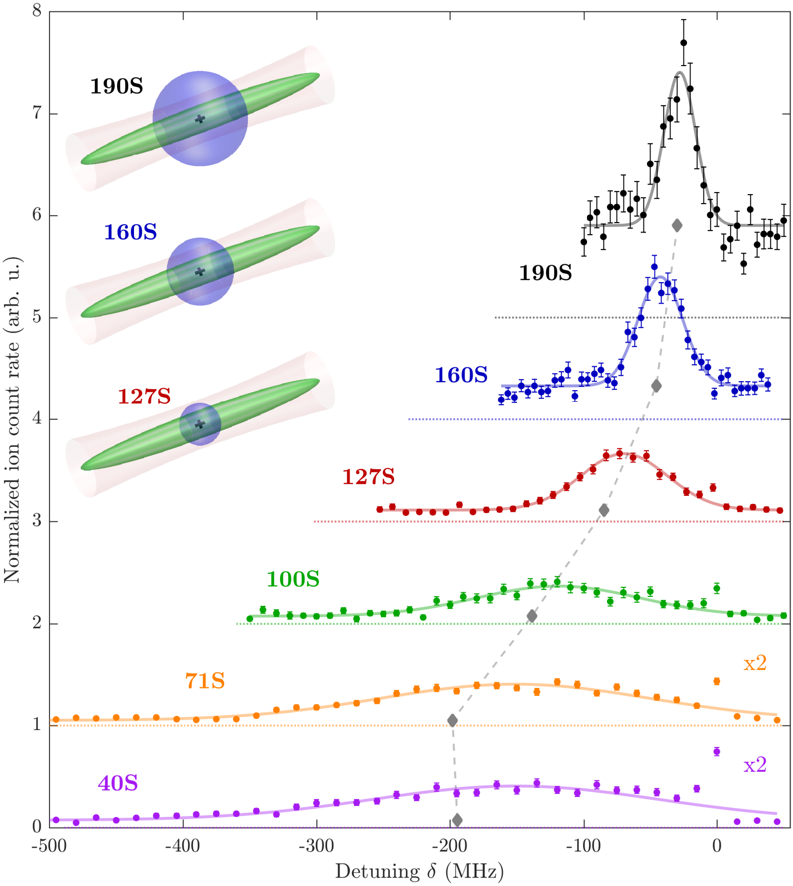

Fig. 6.4: Rydberg spectroscopy in the BEC. The normalized ion count rate is shown as a function of laser detuning δ with respect to the bare $n\mathrm{S}_{1/2}$ Rydberg resonance ($\delta = 0\,\mathrm{MHz}$) for a set of principal quantum numbers n as indicated. Solid lines are Gaussian fits to the data to extract the spectral width σ. The datasets are offset for better readability and zero count rate is denoted by the dotted lines. The data for $n = 40, 71$ is scaled by a factor of two. Error bars show 1σ statistical uncertainty. The filled diamonds indicate the center of the excitation spectra predicted from a full numerical simulation. Insets: Illustration of the BEC dimension (green), trapped in the optical tweezer (red), and the size of the nS Rydberg electron orbit (blue) for the Rydberg states $n = 127, 160, 190$.

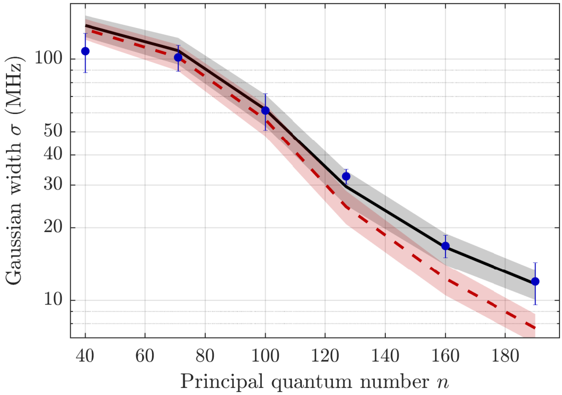

Fig. 6.5: Spectral width σ of the Rydberg spectra, extracted from a Gaussian fit, as a function of principal quantum number n. Error bars indicate the confidence interval from the fitting procedure. The solid black (dashed red) line shows the prediction from our numerical simulation with (without) taking the ion-atom interaction into account. Shaded regions indicate the experimental uncertainty in atom number (±10%) and trapping parameters.

electron-atom interaction is taken into account. In contrast, the model, for which the ion-atom interaction is neglected deviates for high principal quantum numbers. The shaded region indicates the confidence interval due to uncertainties in the input parameters of the theoretical model, namely the atom number and the trap frequencies. The error in the atom number is estimated to be ±10%, while dominant contribution comes from the error in the trap frequency. This is due to the choice of magnetic offset ramps which leads to a trap configuration with a second potential minimum on the y-axis. This doesn't influence the cloud during Rydberg spectroscopy but impedes the precise determination of the trap frequency. Note, that before and after each measurement, the electric stray fields in the chamber are compensated allowing us to achieve Gaussian widths of the bare Rydberg transition in the dilute sample which are $< 1\,\mathrm{MHz}$ for n up to 175 and $< 3\,\mathrm{MHz}$ for $n = 190$.

To gain further evidence for the ion-atom interaction contributing to the line shape of the Rydberg spectroscopy signal, the full modeled line shape should be compared to the measured spectra. In order to reduce the errorbars on the simulated spectra, received by the Monte-Carlo sampling method presented in section 6.2, the trap alignment was improved and the magnetic field ramps adjusted. This leads to a new trap geometry of $\omega_r = 2\pi \times 2442(20)\,\mathrm{Hz}$ for the radial and $\omega_a = 2\pi \times 268(4)\,\mathrm{Hz}$ for the axial trap axis. The residual offset magnetic field at the position of the micro-trap amounts to 1.74 G. Therefore, no correction due to diamagnetic shifts need to be taken into account, as the offset magnetic field is the same during calibration in the dilute cloud and for the final measurement. Additionally, the experimental sequence is repeated at least 100 times for each data point to reduce statistical uncertainty.

In Fig. 6.6, Rydberg spectra for $n = 160$ and $n = 175$ obtained with this optimized experimental sequence are presented. The spectral line shape is directly compared to the result of the simulation. The parameters entering the simulation, which are atom number and trap frequency are determined in independent measurements. The area under the simulated spectrum is normalized to the area below the data, which is obtained by the same Gaussian fitting procedure as described previously.

The model taking only the electron-atom interaction U_e into account, presented in red in Fig. 6.6, clearly deviates from the observed experimental line shape. Especially, the wing reaching to large negative detunings is not reproduced by the model at all. In contrast, the modeled spectrum presented in black, where both the ion-atom and the electron-atom interaction $U_\mathrm{i,e}$ are taken into account agrees much better and indeed reproduces the wing at negative detunings. This comparison unravels the role of ion-atom interaction of the Rydberg nucleus in the Bose-Einstein condensate, broadening and shifting the Rydberg excitation spectrum. It can only be revealed on account of the combination of a large orbit size of the Rydberg atom and the high density of neutral atoms close to its Rydberg nucleus. Deviations between the modeled spectrum and the experimental data at very small detunings are attributed to excitations in the residual thermal low density fraction of the BEC.

Note that spin-orbit interaction in the electron-atom p-wave scattering channel is not included in the Hamiltonian Eq. 6.1 [107, 108]. For the spin configuration studied in this work, the main effect of spin-orbit coupling are slight shifts of the divergence arising from the p-wave shape resonance and small modifications of the Born-Oppenheimer potential close by. We have checked at the example of the data for $n = 160$ that including spin-orbit coupling for p-wave scattering does not significantly affect the simulated excitation spectrum (see App. C.1).

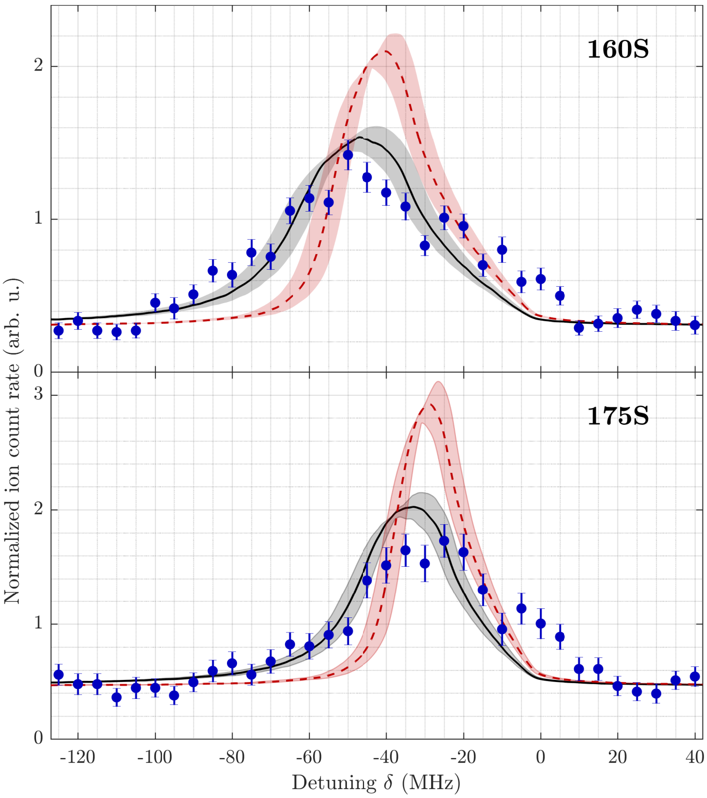

Fig. 6.6: Contribution of ion-atom interaction to Rydberg spectra for high-n Rydberg S-states ($n = 160, 175$). The normalized ion count rate is shown as a function of laser detuning δ in the vicinity of the bare $\left|n\mathrm{S}_{1/2}\right\rangle$ Rydberg resonance ($\delta = 0\,\mathrm{MHz}$). The solid black (dashed red) line shows the result of our full numerical line shape simulation with (without) taking the ion-atom interaction into account. The shaded areas indicate experimental uncertainty dominated by a ±10% error on the atom number [$N = 5.1 \times 10^4$ (160S), $N = 4.6 \times 10^4$ (175S)]. Error bars show 1σ statistical uncertainty.

6.4 Collisional lifetime

In order to perform further studies on the ionic impurity in the micro-BEC it is of great importance to know the lifetime of the Rydberg excitation in the sample. As investigated in Ref. [4] this lifetime in a dense environment is mainly limited by collisions with neighboring atoms, leading to a change of the Rydberg state from the initial S-state into a high-L Rydberg state. For low principal quantum numbers, the collisions can also lead to the formation of Rb_2^+ molecular ions. In both processes, the collision partners gain kinetic energy and leave the micro-BEC.

In order to measure the lifetime, we mainly follow the procedure described in Ref. [110]. The different ionization thresholds of the initial S-state in contrast to the final high-L state are used, to discriminate between the two. Specifically, S-states tend to ionize adiabatically with a threshold close to the classical limit of $1/(16n^4)$. In contrast, the high-L states ionize diabatically at higher field strength $\sim 1/(9n^4)$ [86]. In the experiment, a variable delay time t is introduced after each Rydberg excitation pulse and subsequently a two-step ionization sequence is applied. The first part of the ionization sequence is of lower electric field strength and ionizes predominantly S-states, while the second part ionizes all remaining Rydberg atoms, including high-L states. The two parts are sufficiently delayed in time, to ensure that the ionization products can be distinguished by their arrival time on the detector. Additionally, associated Rb_2^+ ions are also distinguished in time-of-flight due to their higher mass. Both, the fraction of detected S-states p_S and the sum of measured high-L and Rb_2^+ fraction $(1 - p_\mathrm{S})$ is extracted. The routine is repeated for increasing ionization delay times t to determine the collisional lifetime. Note, that the detuning δ is fixed to the center of the respective spectrum in Fig. 6.4, as exctracted from the Gaussian fit.

An exemplary data set for $n = 160$ is shown in Fig. 6.7(a). The Rydberg lifetime is extracted by fitting an exponential decay to the S-state fraction according to

$$p_\mathrm{S} = (1 - c) + c \cdot \exp\left(-\frac{t - t_0}{\tau}\right). \tag{6.4}$$

Here, c is a constant accounting for finite discriminability between S and high-L states, whereas the constant t_0 captures the pulse lengths. The lifetime τ is presented as a function of principal quantum number n in Fig. 6.7(b). Note that the lifetimes are determined for the settings and principal quantum numbers as for the first data set, which was presented in Fig. 6.4. The lifetime strongly raises with increasing principal quantum number. This is compatible

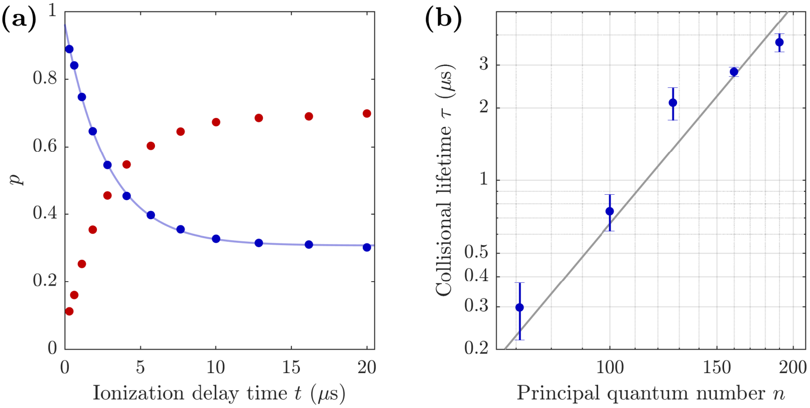

Fig. 6.7: Lifetime of the Rydberg excitation in the dense micro-BEC. (a) Fraction of S-states p_{S} (blue symbols) ionized by the first field pulse (0.85 V/cm) and fraction of high-L states (red symbols) ionized by the second field pulse (3.6 V/cm) of the state-selective ionization sequence as a function of delay time t. The data is taken for the 160S state at a detuning $\delta = 42.2\,\mathrm{MHz}$, corresponding to the line center of the spectrum in Fig. 6.4. Statistical error bars are smaller than the symbol size. The blue solid line is a fit to the data based on Eq. 6.4. (b) Collisional lifetime τ of the Rydberg excitation in the BEC as a function of principal quantum number n. The solid line is a fit to the data based on a $\propto n^3$ scaling.

to the trend observed in Ref. [4], where collisional lifetimes were investigated for a large BEC exceeding the Rydberg orbit size by far. Hence, it seems that the limiting factor for the lifetime is not the number of neutral atoms inside the Rydberg orbit but rather the the density of atoms at the position of the Rydberg nucleus and the simultaneous presence of the Rydberg electron at the core position. For Rydberg S-states the electron probability density at the position of the core decreases $\propto n^{-3}$, motivating the empirical fit $\propto n^{-3}$ (gray line) to the data, presented in Fig. 6.7(b). The dependence on the atomic density seems to be linear, as rescaling our life times according to the sixfold higher peak density in comparison to Ref. [4] leads to good agreement.

Note that for the Rydberg spectra, presented in Fig. 6.4 and Fig. 6.6, the ionization fields are chosen large enough to ionize both, S-states and high-L states, and are switched on after a fixed delay time of 200 ns. Additionally, the excitation time was chosen to 500 ns for $n > 71$ and 200 ns for $n = 40, 71$ to avoid any effects due to the limited lifetime.

In order to study the ion-atom interaction in the BEC in the future, the lifetime could be further increased when circular Rydberg states are excited instead of S-states. This would be additionally advantageous, as the overlap between the Rydberg orbital and the BEC would be further reduced.

7

Summary and outlook

In this thesis, the interaction of ions and electrons with ultracold atoms was investigated at the example of Rubidium-87. Thereto, a Rydberg atom was excited in a dense ultracold cloud. Both the interaction of the ionic core of the Rydberg atom and the Rydberg electron itself with neighboring neutral atoms was studied. Two main achievements were reported: First, photo-association of hybrid Trilobite Rydberg molecules was demonstrated. This is a special type of homonuclear molecules with a large electric dipole moment, which is bound by the electron-atom interaction. Second, it was shown for the first time that the ion-atom interaction between the Rydberg ionic core and the neutral atom can be accessed experimentally. The ion-atom interaction was observed at submicrokelvin temperature, once the nearest neighbor spacing in BEC is small and the electron-atom interaction is suppressed.

A Rydberg atom interacting with a neutral atom

The two-body Born-Oppenheimer potentials for the interaction of the Rydberg atom with one neutral atom were studied in detail as presented in chapter 3. The interaction is described by contributions of the two charges each interacting with the neutral atom in its electronic ground state: The Rydberg nucleus attracts the neutral atom, which is given by a classical polarization potential. This ion-atom interaction dominates only for short internuclear separations about $< 1000\,\mathrm{a_0}$. In addition, the Rydberg electron and the neutral atom interact, which requires a quantum mechanical treatment via contact interaction. The electron-atom interaction is the dominant contribution for larger internuclear separations.

There are several relevant terms contributing to the electron-atom interaction: For Rydberg levels isolated by their quantum defect, the electron-atom scattering leads to potential wells supporting bound states for the ultralong-range Rydberg molecules. For this finding, only s-wave scattering needs to be taken into account and the Rydberg electron spin and the total spin of the neutral atom have to be aligned in a triplet configuration. When this triplet s-wave scattering is applied for the case of the (almost) degenerate Rydberg levels of the hydrogenic manifold, one potential energy curve is lowered in energy in the GHz range and supports Trilobite Rydberg molecules. These molecules are of special interest as they possess huge electric dipole moments. When p-wave scattering between the Rydberg electron and the neutral atom is considered as well, it modifies the Born-Oppenheimer potentials mainly in the range, where the Rydberg electron has gained about 23 meV of kinetic energy in the Coulomb potential of the Rydberg ionic core. This is the consequence of a shape resonance occurring at this energy. The shape resonance allows for the creation of yet another type of Rydberg molecules, so-called Butterfly Rydberg molecules, which possess large electric dipole moments as well. In the general case, where the spin of the Rydberg electron is not parallel to the spin of the neutral atom, the treatment has to be extended to comprise both singlet and triplet scattering. Even mixing of the singlet and triplet scattering channel is possible. Additionally, the hyperfine interaction of the neutral atom has to be taken into account, as the electron spin is coupled to the nuclear spin.

The Hamiltonian modeling the interaction of the Rydberg atom with the neutral atom comprises these electron-atom s- and p-wave, singlet and triplet interaction terms in addition to the ion-atom contribution. The full Hamiltonian including the binding energies of the bare Rydberg states, the interaction terms and the hyperfine interaction in the perturber atom is set up for a truncated basis of bare Rydberg states. Via diagonalization, the Born-Oppenheimer potential energy curves are obtained for varying internuclear separations. With these potentials, we can calculate binding energies of Rydberg molecular states and compare them to spectroscopically determined binding energies.

In addition to these terms, the code is capable of including the Zeeman effect for external magnetic fields, if the field is pointing along the internuclear axis. This enables to compare the results to experiments performed in our magnetic trap. In the future, the code could be extended to account for external electric fields and magnetic fields with arbitrary orientation with respect to the internuclear axis. Besides, it would be desirable to extend the model to take also the spin-orbit interaction in the scattering process into account [107, 108].

Trilobite Rydberg molecules

Trilobite Rydberg molecules are a special class of Rydberg molecules and are of great interest as they possess huge electric dipole moments which they inherit from the contribution of Rydberg orbitals with high angular momentum L. However, photo-association of this molecules via one- or two-photon transitions is almost impossible, due to the lack of low-L character in combination with dipole selection rules.

In section 5, which is based on Ref. [2], a method is presented to overcome this problem. Resonant coupling between the orbital angular momentum of the Rydberg electron and the nuclear spin of the neutral atom allows for the admixture of S-character to the Trilobite potential energy curve. More specifically, the singlet Trilobite potential energy curve for the neutral atom in $F = 1$ gets mixed with the S-type potential of mixed singlet and triplet scattering character for the neutral perturber in $F = 2$. To tune the two potential energy curves in resonance, the principal quantum number is adjusted to $n = 50$, for which the hyperfine interaction energy in the neutral atom is comparable to the energy gap between the S-type and the Trilobite potential energy curve. Such hybrid Trilobite molecules supported by this mixed potential energy curve were investigated spectroscopically and their binding energies were determined. In addition, by monitoring the response to an external electric field it was shown, that these molecules possess a electric dipole moments of more than 100 Debye.

The new approach to photo-associate Trilobite Rydberg molecules presented in this thesis is readily applicable to other atomic species that have a hyperfine structure. This opens routes for the tailored engineering of long-range interacting few- to many-body systems based on strongly polar Rydberg molecules as discussed for a 1D chain system of such molecules in Ref. [51]. Moreover, exotic polarons [49, 50] could be realized by a polar molecule acting as an impurity in a many-body system serving as a bath. Finally, Trilobite Rydberg molecules could be employed to probe quantum chemistry on mesoscopic scales [4].

Ion-atom interaction of the Rydberg nucleus in a BEC

Several experimental platforms are dedicated to investigate the interaction of neutral atoms with ions held in a Paul trap[61, 64, 71–73, 121]. Yet, the extension to the quantum scattering regime could open up a new world of phenomena studied in such experiments. This includes the detailed study of the molecular potential including scattering resonances [58–60], ultracold quantum chemistry [61–64], impurity physics with charged particles [65–67] and quantum simulation [68–70]. In section 6 of this thesis, which is based on Ref. [1], a new approach is presented, allowing to study ion-atom interaction at submicrokelvin temperature. This temperature is about three orders of magnitude lower than for hybrid systems based on a Paul trap and only one order of magnitude above the quantum mechanical s-wave scattering limit.

Starting with a micron-sized very dense Bose-Einstein condensate of rubidium atoms, one single atom among them was excited to a high-lying Rydberg state up to $n = 190$. In this case, many neighboring atoms are located inside the Rydberg orbit. Therefore, a Monte-Carlo sampling method was applied to find the integrated effect of all the atoms within the Rydberg orbit. Due to the small nearest neighbor spacing in the sample, the ionic core of the Rydberg atom interacts significantly with neutral neighboring atoms. This has been clearly revealed by a line shape analysis of the Rydberg spectroscopy line in comparison to the modeled line shape. The ion-atom interaction is usually dominated by the electron-atom interaction of the Rydberg electron with the atoms within its orbit. Due to the extremely large Rydberg orbit in this work, the electron-atom interaction could be strongly suppressed. As the Rydberg orbit of $\approx 3.7\,\mu\text{m}$ exceeds the size of the micro-BEC along the short trap axis of $\approx 1.0\,\mu\text{m}$ by far, the overlap of the electron probability density with the ultracold sample was reduced. With the electron still being present, it even provided a Faraday shield for the Rydberg nucleus, preventing its acceleration due to detrimental electric stray fields. In addition the lifetime of the Rydberg excitation in the micro-BEC was studied.

This novel approach to study ion-atom interaction for a single ionic impurity in a micro-BEC at submicrokelvin temperature opens a new way to study the quantum regime of ion-atom scattering. The choice of an atomic species with a higher s-wave scattering limit such as lithium ($E^* \approx k_\mathrm{B} \times 30\,\mu\mathrm{K}$) or a reduced or even recoil-free Rydberg excitation [129] can push the system temperature to the quantum scattering regime. To study the ion-atom interaction the excitation of circular Rydberg states could be promising [130–132], as this would further reduce the overlap between the Rydberg orbit and the micro-BEC and additionally the lifetime is expected to be orders of magnitudes higher. It could allow for reaching motional timescales of the ion, that could possibly be extended by optical trapping techniques [133], to open new routes to explore many-body polaron physics. In order to make the electron-atom interaction vanish completely, one could apply photo-ionization [59] - however, then the Faraday shielding for the ion provided by the electron will vanish with it. Note that the ion-atom interaction is probed via the Rydberg electron in this thesis. It is not yet clear, how the pure ion-atom interaction could be experimentally observed, especially if photo-ionization is applied.

A

Rydberg molecules

A.1 Trilobite and Butterfly Rydberg molecules

For reference, see [106]. The Hamiltonian H_{sc} for the electron-atom s-wave scattering term can be evaluated in a truncated basis of bare Rydberg states $b = (\Psi_1(\mathbf{r}), \Psi_2(\mathbf{r}), ...\Psi_n(\mathbf{r}))^T$. Each matrix element in the Hamiltonian for degenerate states is then given by

$$\begin{aligned} H_{\mathrm{sc},ij} &= 2\pi a_{\mathrm{s}}^{\mathrm{T}}(k(R)) \int d\mathbf{r} \Psi_i^*(\mathbf{r}) \delta^3(\mathbf{r} - R\mathbf{z}) \Psi_j^*(\mathbf{r}) \\ &= 2\pi a_{\mathrm{s}}^{\mathrm{T}}(k(R)) \Psi_i^*(R) \Psi_j(R), \end{aligned} \tag{A.1}$$

which in total results in a structure like

$$H_{\mathrm{sc}}(R) = c(R) \begin{pmatrix} |\Psi_1(R)|^2 & \Psi_1^*(R)\Psi_2(R) & ... & \Psi_1^*(R)\Psi_n(R) \\ \Psi_2^*(R)\Psi_1(R) & |\Psi_2(R)|^2 & ... & \Psi_2^*(R)\Psi_n(R) \\ \vdots & \vdots & \ddots & \vdots \\ \Psi_n^*(R)\Psi_1(R) & \Psi_n^*(R)\Psi_2(R) & ... & |\Psi_n(R)|^2 \end{pmatrix} \tag{A.2}$$

with $c(R) = 2\pi a_{\mathrm{s}}^{\mathrm{T}}(k(R))$. Therefore, this Hamiltonian can be written as $c(R) \cdot M(R) = c(R) \cdot v(R) v^\dagger(R)$ with $v(R) = (\Psi_1(R), \Psi_2(R), ...\Psi_n(R))^T$.

One can show that for a matrix of this form, $(n-1)$ eigenvalues are zero: For $M \neq 0$ and $v \neq 0$ one knows that $\text{rank}(M) \neq 0$. In addition, one can apply the Sylvester theorem for separable matrices and finds $\text{rank}(M) = \text{rank}(vv^\dagger) \leq \text{rank}(v) \cdot \text{rank}(v^\dagger) = 1 \cdot 1$. So the rank of the matrix is one, which means, that there is only one non-zero eigenvalue. This eigenvalue λ is found by $Hv = (c \cdot vv^\dagger)v = c \cdot v(v^\dagger v) = v(c \sum_i |v_i|^2)$, so the eigenvalue is $\lambda(R) = c \sum_i |\Psi_i(R)|^2$, corresponding to the Trilobite curve with the eigenvector equal to $v(R)$. Therefore, the wave function of the Trilobite molecule is given by basis states (which are the bare Rydberg wave functions) weighted by the entries of the normalized eigenvector, resulting in

$$\Psi_{\text{Trilobite}}(\mathbf{r}, R) = \frac{\sum_i \Psi_i(R)\Psi_i(\mathbf{r})}{\sqrt{\sum_i |\Psi_i(R)|^2}}. \tag{A.3}$$

For $\mathbf{r} = R\mathbf{z}$ which is the location of the neutral atom, all summands in the numerator are positive, corresponding to constructive interference of the $\Psi\mathbf{r}$. This leads to the high electron density at the position of the neutral atom and the large electric dipole moment, characteristic for Trilobite Rydberg molecules. As Rydberg wave functions with $m_l > 0$ are zero on the $\mathbf{z}$-axis, only Rydberg states with $m_j \in \{-\frac{1}{2}, \frac{1}{2}\}$ contribute to the Trilobite molecular wave function.

For the p-wave scattering the same procedure can be applied: Setting $c(R) = 6\pi a_{\text{p}}^{\text{T}}(k(R))$ and $v(R) = (\nabla_\xi \Psi_1(R), \nabla_\xi \Psi_2(R), ... \nabla_\xi \Psi_n(R))^T$ with $\xi \in \{R, \theta, \phi\}$. For each ξ, there are $(n-1)$ eigenvalues equal to zero and a single eigenvalue given by $\lambda_\xi(R) = c \sum_i |\nabla_\xi \Psi_i(R)|^2$. These $\lambda_\xi(R)$ constitute the Butterfly molecular PECs. The corresponding wave functions of the Butterfly molecular state are then given by

$$\Psi_{\xi-\text{Butterfly}}(\mathbf{r}, R) = \frac{\sum_i (\nabla_\xi \Psi_i(R))\Psi_i(\mathbf{r})}{\sqrt{\sum_i |\nabla_\xi \Psi_i(R)|^2}}. \tag{A.4}$$

As discussed in Ref. [37] only Rydberg wave functions with $m = 0$ contribute to the R-Butterfly and maximize its gradient along R, whereas only $m = 1$ wave functions contribute to the angular Butterfly orbit, where the gradient orthogonal to the internuclear axis is maximized.

A.2 Evaluating the matrix element of the Hamiltonian for the Born-Oppenheimer potentials

The Born-Oppenheimer potential curves are calculated by evaluating the matrix elements $\langle\Psi(\mathbf{r})|\,\hat{H}(\mathbf{r},R)\,|\Psi'(\mathbf{r})\rangle$ of the Hamiltonian

$$\begin{aligned}\hat{H}(\mathbf{r},R) =&\hat{H}_0+\hat{H}_\mathrm{s}^\mathrm{T}+\hat{H}_\mathrm{s}^\mathrm{S}+\hat{H}_\mathrm{p}^\mathrm{T}+\hat{H}_\mathrm{p}^\mathrm{S}+\hat{H}_{HFS}+\hat{H}_\mathrm{i}\\ \hat{H}(\mathbf{r},R) =&\hat{H}_0+\left[2\pi a_\mathrm{s}^\mathrm{T}(k(R))\hat{\mathcal{P}}_\mathrm{T}+2\pi a_\mathrm{s}^\mathrm{S}(k(R))\hat{\mathcal{P}}_\mathrm{S}\right]\delta^3(\mathbf{r}-R\hat{\mathbf{z}})\\ &+\left[6\pi a_\mathrm{p}^\mathrm{T}(k(R))\hat{\mathcal{P}}_\mathrm{T}+6\pi a_\mathrm{p}^\mathrm{S}(k(R))\hat{\mathcal{P}}_\mathrm{S}\right]\delta^3(\mathbf{r}-R\hat{\mathbf{z}})\overleftarrow{\nabla}\cdot\overrightarrow{\nabla}\\ &+A_\mathrm{HFS}\hat{\mathbf{S}}_2\cdot\hat{\mathbf{I}}_2-\frac{C_4}{R^4}\,. \end{aligned}\tag{A.5}$$

in the basis $|n,L_1,J_1,m_{J_1};m_{S_2},m_I\rangle^1$ for a fixed value of R and diagonalizing this matrix to find the new eigenenergies and eigenvectors for the Rydberg levels including the interaction with a new atom. In order to retrieve the potential energy curves this eigenenergies parametrically depending on R are then joined. In space coordinates this wave functions can be written as

$$\begin{aligned}&\langle\mathbf{r}|n,L_1,J_1,m_{J_1};m_{S_2},m_I\rangle\\ &=\mathcal{R}_{n,L_1,J_1}(r)\sum_{m_{S_1}}\langle L_1,m_{L_1},S_1,m_{S_1}|J_1,m_{J_1}\rangle\,Y_{L_1}^{m_{L_1}}(\theta,\phi)\otimes|m_{S_2},m_I\rangle\end{aligned}\tag{A.6}$$

where the sum includes $m_{S_1}=\pm1$ and the magnetic quantum number $m_{L_1}=m_{J_1}-m_{S_1}$. This needs to be done, as the Rydberg states in the J,m_J-basis need to be written as a superposition of states in the L,m_L,S,m_S-basis, in order to use the spherical harmonics $Y_{L_1}^{m_{L_1}}(\theta,\phi)$. Apart from that, the decomposition into the L,m_L,S,m_S-basis allows to evaluate the singlet and triplet projection operators which depend on S rather than J.

A.2.1 Evaluating the Clebsch-Gordan coefficient

The Clebsch-Gordan coefficient $C_{L,m_L,S,m_S}^{J,m_J}=\langle L,m_L,S,m_S|J,m_J\rangle$ needed for decomposition of the Rydberg states given in the J,m_J-basis into the states given in the L,m_L,S,m_S-basis, can be simplified for our special case

---

[1] n from now on refers to n_1 and I to I_2.

[134] as

$$C^{J,m_J}_{L,m_L,S,m_S} = \pm\sqrt{\frac{L+1/2\pm m_{J_1}}{2L+1}} \quad \text{for } S=\frac{1}{2},\ m_S=\frac{1}{2},\ J=L\pm\frac{1}{2}$$
$$C^{J,m_J}_{L,m_L,S,m_S} = \sqrt{\frac{L+1/2\mp m_{J_1}}{2L+1}} \quad \text{for } S=\frac{1}{2},\ m_S=-\frac{1}{2},\ J=L\pm\frac{1}{2}. \tag{A.7}$$

A.2.2 Evaluating the triplet and singlet projection operators

The singlet and triplet projection operators can be written as

$$\hat{\mathcal{P}}_{\mathrm{T}} = \frac{3}{4} + \hat{S}_1\cdot\hat{S}_2$$
$$\hat{\mathcal{P}}_{\mathrm{S}} = \frac{1}{4} - \hat{S}_1\cdot\hat{S}_2, \tag{A.8}$$

and when evaluating the projector one makes use of the relation

$$\langle\Psi(\mathbf{r})|\,\hat{S}_1\cdot\hat{S}_2\,|\Psi(\mathbf{r})\rangle = \frac{1}{2}\,\langle\Psi(\mathbf{r})|\,S_1^+S_2^- + S_1^-S_2^+ + 2S_1^zS_2^z\,|\Psi(\mathbf{r})\rangle \tag{A.9}$$

with the raising and lowering operators S^+ and S^- and the spin projection operator along z

$$\left\langle S',m'_S\right|S^z\left|S,m_S\right\rangle = \hbar m_S\ \delta_{S',S}\ \delta_{m'_S,m_S}$$
$$\left\langle S',m'_S\right|S^+\left|S,m_S\right\rangle = \hbar\sqrt{(S-m_S)(S+m_S+1)}\delta_{S',S}\ \delta_{m'_S-1,m_S}$$
$$\left\langle S',m'_S\right|S^-\left|S,m_S\right\rangle = \hbar\sqrt{(S+m_S)(S-m_S+1)}\delta_{S',S}\ \delta_{m'_S+1,m_S}. \tag{A.10}$$

This results in

$$\left\langle S'_1=\frac{1}{2},m'_{S_1},S'_2=\frac{1}{2},m'_{S_2}\right|\hat{S}_1\cdot\hat{S}_2\left|S_1=\frac{1}{2},m_{S_1},S_2=\frac{1}{2},m_{S_2}\right\rangle$$
$$=\frac{\hbar^2}{2}\Bigg[2m_{S_1}m_{S_2}\ \delta_{m'_{S_1},m_{S_1}}\ \delta_{m'_{S_2},m_{S_2}}$$
$$+\sqrt{\left(\frac{1}{2}-m_{S_1}\right)\left(\frac{3}{2}+m_{S_1}\right)\left(\frac{1}{2}+m_{S_2}\right)\left(\frac{3}{2}-m_{S_2}\right)}\ \delta_{m'_{S_1}-1,m_{S_1}}\ \delta_{m'_{S_2}+1,m_{S_2}}$$
$$+\sqrt{\left(\frac{1}{2}+m_{S_1}\right)\left(\frac{3}{2}-m_{S_1}\right)\left(\frac{1}{2}-m_{S_2}\right)\left(\frac{3}{2}+m_{S_2}\right)}\ \delta_{m'_{S_1}+1,m_{S_1}}\ \delta_{m'_{S_2}-1,m_{S_2}}\Bigg] \tag{A.11}$$

A.2.3 Evaluating the s-wave electron-neutral scattering term

The evaluation of the s-wave scattering term of the electron-neutral interaction for the singlet and triplet case is given by

$$\begin{aligned}
&\langle n, L_1, J_1, m_{J_1}; m_{S_2}, m_I | \, \hat{H}_{\mathrm{s}}^{\mathrm{T/S}} \left| n', L_1', J_1', m_{J_1}'; m_{S_2}', m_I' \right\rangle \\
&= \delta_{m_I, m_I'} \left\langle n, L_1, J_1, m_{J_1}; m_{S_2} \right| 2\pi a_{\mathrm{s}}^{\mathrm{T/S}} \hat{\mathcal{P}}_{\mathrm{T/S}} \delta^3(\mathbf{r} - R\hat{\mathbf{z}}) \left| n', L_1', J_1', m_{J_1}'; m_{S_2}' \right\rangle \\
&= \delta_{m_I, m_I'} 2\pi a_{\mathrm{s}}^{\mathrm{T/S}}(k) \sum_{m_{S_1}=-1/2}^{1/2} \sum_{m_{S_1}'=-1/2}^{1/2} C^{J_1, m_{J_1}}_{L_1, m_{L_1}, S_1, m_{S_1}} C^{J_1', m_{J_1}'}_{L_1', m_{L_1}', S_1', m_{S_1}'} \\
&\quad \times \int \mathcal{R}_{n, L_1, J_1}(r) \mathcal{R}_{n', L_1', J_1'}(r) \; \delta(r - R) \; dr \\
&\quad \times \int Y_{L_1}^{m_{L_1}}(\theta, \phi) \left(Y_{L_1'}^{m_{L_1}'}(\theta, \phi) \right)^* \; \delta(\theta - \theta_0) \delta(\phi - \phi_0) \; d\theta \; d\phi \\
&\quad \times \left\langle S_1', m_{S_1}', S_2', m_{S_2}' \right| \hat{\mathcal{P}}_{\mathrm{T/S}} \left| S_1, m_{S_1}, S_2, m_{S_2} \right\rangle . \qquad \text{(A.12)}
\end{aligned}$$

The Clebsch-Gordan coefficients $C^{J, m_J}_{L, m_L, S, m_S}$ can be calculated according to Eq. A.7 and the projection operators $\hat{\mathcal{P}}_{\mathrm{T/S}}$ according to sec. A.2.2. The radial integral we solve numerically for each value of R. The integral of the angular coordinates can be simplified, as we set $\theta_0 = 0$ and $\phi_0 = 0$ by setting the position of the perturber onto the z-axis. In addition, it is known, that all Laplace's spherical harmonics with $m_L \neq 0$ vanish on the z-axis. Therefore, it can be simplified according to

$$\begin{aligned}
Y_L^{m_L=0}(\theta_0 = 0, \phi_0 = 0) &= \frac{1}{\sqrt{2\pi}} \sqrt{\frac{(2L+1)}{2} \frac{(L - m_L)!}{(L + m_L)!}} \; P_L^{m_L}(\cos\theta) e^{i m_L \phi} \\
&= \frac{1}{\sqrt{2\pi}} \sqrt{\frac{(2L+1)}{2} \frac{(L - 0)!}{(L + 0)!}} \; P_L^0(1) e^0 \\
&= \frac{1}{\sqrt{2\pi}} \sqrt{\frac{2L+1}{2}}
\end{aligned} \qquad \text{(A.13)}$$

and the integral over the angular coordinates θ and ϕ is therefore given by

$$\begin{aligned}
&\int Y_{L_1}^{m_{L_1}}(\theta, \phi) \left(Y_{L_1'}^{m_{L_1}'}(\theta, \phi) \right)^* \; \delta(\theta - \theta_0) \delta(\phi - \phi_0) \; d\theta d\phi \\
&\quad = \frac{1}{4\pi} \sqrt{(2L_1 + 1)(2L_1' + 1)} \qquad \text{(A.14)}
\end{aligned}$$

A.2.4 Evaluating the p-wave electron-neutral scattering term

The evaluation of the p-wave scattering term of the electron-neutral interaction for the singlet and triplet case is performed analogously to the s-wave scattering term. The matrix elements of the Hamiltonian

$$\begin{aligned}
&\langle n, L_1, J_1, m_{J_1}; m_{S_2}, m_I |\, \hat{H}_{\mathrm{p}}^{\mathrm{T/S}} \left| n', L_1', J_1', m_{J_1}'; m_{S_2}', m_I' \right\rangle \\
&= \delta_{m_I, m_I'} \langle n, L_1, J_1, m_{J_1}; m_{S_2} |\, 6\pi a_{\mathrm{p}}^{\mathrm{T/S}} \hat{\mathcal{P}}_{\mathrm{T/S}} \delta^3(\mathbf{r} - R\hat{\mathbf{z}}) \overleftarrow{\nabla} \cdot \overrightarrow{\nabla} \left| n', L_1', J_1', m_{J_1}'; m_{S_2}' \right\rangle \\
&= \delta_{m_I, m_I'} 6\pi a_{\mathrm{p}}^{\mathrm{T/S}}(k) \sum_{m_{S_1}=-1/2}^{1/2} \sum_{m_{S_1}'=-1/2}^{1/2} C_{L_1, m_{L_1}, S_1, m_{S_1}}^{J_1, m_{J_1}} C_{L_1', m_{L_1}', S_1', m_{S_1}'}^{J_1', m_{J_1}'} \\
&\times \int \overrightarrow{\nabla} \left(\mathcal{R} Y\right) \overrightarrow{\nabla} \left(\mathcal{R}' Y'^{*}\right)\ \delta^3(\mathbf{r} - R\hat{\mathbf{z}})\ d^3 r \\
&\times \left\langle S_1', m_{S_1}', S_2', m_{S_2}' \right| \hat{\mathcal{P}}_{\mathrm{T/S}} \left| S_1, m_{S_1}, S_2, m_{S_2} \right\rangle . \qquad \text{(A.15)}
\end{aligned}$$

have to be calculated, depending parametrically on R. Again, the Clebsch-Gordan coefficients $C_{L, m_L, S, m_S}^{J, m_J}$ can be calculated according to Eq. A.7 and the singlet and triplet projection operators $\hat{\mathcal{P}}_{\mathrm{T/S}}$ according to sec. A.2.2 the same as for the s-wave scattering case.

The integral needs some further study. For better readability, we neglect the indices for now. As the radial part of the wave function $\mathcal{R}$ only depends on the radial coordinate r, whereas the spherical harmonics Y only depend on the angular coordinates θ, ϕ, the gradient of the wave function is given by

$$\overrightarrow{\nabla} \left(\mathcal{R}_{n, L_1, J_1}(r) Y_{L_1}^{m_{L_1}}(\theta, \phi) \right) = \begin{pmatrix} \frac{\partial \mathcal{R}}{\partial r} Y \\ \frac{1}{r} \mathcal{R} \frac{\partial Y}{\partial \theta} \\ \frac{\mathcal{R}}{r \sin(\theta)} \frac{\partial Y}{\partial \phi} \end{pmatrix} \qquad \text{(A.16)}$$

and so the integral is evaluated as

$$\begin{aligned}
&\int \vec{\nabla}\left(\mathcal{R}Y\right) \vec{\nabla}\left(\mathcal{R}'Y'^*\right) \ \delta^3(\mathbf{r}-R\hat{\mathbf{z}}) \ d^3r \\
&= \int\int\int \left[\frac{\partial \mathcal{R}}{\partial r}\frac{\partial \mathcal{R}'}{\partial r} YY'^* + \frac{\mathcal{R}}{r}\frac{\mathcal{R}'}{r}\frac{\partial Y}{\partial \theta}\frac{\partial Y'^*}{\partial \theta} + \frac{\mathcal{R}}{r\sin(\theta)}\frac{\mathcal{R}'}{r\sin(\theta)}\frac{\partial Y}{\partial \phi}\frac{\partial Y'^*}{\partial \phi}\right] \\
&\qquad \times \delta(r-R)\delta(\theta-\theta_0)\delta(\phi-\phi_0) \ dr \ d\theta \ d\phi \\
&= \underbrace{\int \frac{\partial \mathcal{R}}{\partial r}\frac{\partial \mathcal{R}'}{\partial r} \ \delta(r-R) \ dr}_{I_{\mathrm{R1}}} \underbrace{\int\int YY'^* \ \delta(\theta-\theta_0)\delta(\phi-\phi_0) \ d\theta \ d\phi}_{I_{\mathrm{Ang1}}} \\
&+ \underbrace{\int \frac{\mathcal{R}}{r}\frac{\mathcal{R}'}{r} \ \delta(r-R) \ dr}_{I_{\mathrm{R2}}} \underbrace{\int\int \frac{\partial Y}{\partial \theta}\frac{\partial Y'^*}{\partial \theta} \ \delta(\theta-\theta_0)\delta(\phi-\phi_0) \ d\theta \ d\phi}_{I_{\mathrm{Ang2}}} \\
&+ \underbrace{\int \frac{\mathcal{R}}{r}\frac{\mathcal{R}'}{r} \ \delta(r-R) \ dr}_{I_{\mathrm{R3}}} \underbrace{\int\int \frac{1}{\sin(\theta)}\frac{1}{\sin(\theta)}\frac{\partial Y}{\partial \phi}\frac{\partial Y'^*}{\partial \phi} \ \delta(\theta-\theta_0)\delta(\phi-\phi_0) \ d\theta \ d\phi}_{I_{\mathrm{Ang3}}} \\
&= I_{\mathrm{R1}} \times I_{\mathrm{Ang1}} + I_{\mathrm{R2}} \times I_{\mathrm{Ang2}} + I_{\mathrm{R3}} \times I_{\mathrm{Ang3}} \qquad \text{(A.17)}
\end{aligned}$$

where we introduced the I labels for the different integrals. We evaluate the integrals $I_{\mathrm{R1}}, I_{\mathrm{R2}}, I_{\mathrm{R3}}$ numerically. The integral I_{Ang1} is the same as for the s-wave case and results in

$$I_{\mathrm{Ang1}} = \int\int YY'^* \ \delta(\theta-\theta_0)\delta(\phi-\phi_0) \ d\theta \ d\phi = \frac{1}{4\pi}\sqrt{(2L_1+1)(2L_1'+1)}. \qquad \text{(A.18)}$$

as $\theta_0 = 0$ and $\phi_0 = 0$ and only $m_L = 0$ terms contribute.

For the evaluation of I_{Ang2} we need the gradient of the spherical harmonic along θ which is (see Ref. [93])

$$\begin{aligned}
\frac{\partial Y_L^m}{\partial \theta} &= \sqrt{\frac{2L+1}{16\pi}\frac{(L-m)!}{(L+m)!}} \left[P_L^{m+1}(\cos(\theta)) \right. \\
&\qquad \left. -(L+m)(L-m+1)P_L^{m-1}(\cos(\theta))\right] e^{im\phi} \\
&= \sqrt{\frac{2L+1}{16\pi}\frac{(L-m)!}{(L+m)!}} \left[P_L^{m+1}(1) - (L+m)(L-m+1)P_L^{m-1}(1)\right]
\end{aligned} \qquad \text{(A.19)}$$

where the second line is valid for $\theta = 0$ and $\phi = 0$. The Legendre polynomials are only non-vanishing for $P_L^0(1) = 1$, so only spherical harmonics with $m \pm 1$ have a non-zero gradiant on the z-axis. Therefore, the second angular integral results in

$$\begin{aligned}
I_{\text{Ang2}} &= \int\int \frac{\partial Y}{\partial\theta}\frac{\partial Y'^*}{\partial\theta}\ \delta(\theta-\theta_0)\delta(\phi-\phi_0)\ d\theta\ d\phi \\
&= \sqrt{\frac{(2L_1+1)}{16\pi}\frac{(2L_1'+1)}{16\pi}\frac{(L_1-(m_{L_1}))!}{(L_1+(m_{L_1}))!}\frac{(L_1'-(m_{L_1}'))!}{(L_1'+(m_{L_1}'))!}} \\
&\quad\times\left[P_{L_1}^{m_{L_1}+1}(1) - (L_1+m_{L_1})(L_1-m_{L_1}+1)P_{L_1}^{m_{L_1}-1}(1)\right] \\
&\quad\times\left[P_{L_1'}^{m'_{L_1}+1}(1) - (L_1'+m'_{L_1})(L_1'-m'_{L_1}+1)P_{L_1'}^{m'_{L_1}-1}(1)\right] \\
&= \sqrt{\frac{(2L_1+1)}{16\pi}\frac{(2L_1'+1)}{16\pi}((L_1+1)L_1)^{-m_{L_1}}((L_1'+1)L_1')^{-m'_{L_1}}} \\
&\quad\times\left[\delta_{m_{L_1},-1} - (L_1+m_{L_1})(L_1-m_{L_1}+1)\delta_{m_{L_1},1}\right] \\
&\quad\times\left[\delta_{m'_{L_1},-1} - (L_1'+m'_{L_1})(L_1'-m'_{L_1}+1)\delta_{m'_{L_1},1}\right]. \qquad \text{(A.20)}
\end{aligned}$$

The third angular integral contains the derivative of the spherical harmonic with respect to the angle ϕ (see Ref. [93])

$$\begin{aligned}
\frac{1}{\sin(\theta)}\frac{\partial Y_L^m}{\partial\phi} &= \sqrt{\frac{2L+1}{16\pi}\frac{(L-m)!}{(L+m)!}}\left[-P_L^{m+1}(\cos(\theta))\right. \\
&\qquad \left.-(L+m)(L-m+1)P_L^{m-1}(\cos(\theta))\right]\frac{ie^{im\phi}}{\cos(\theta)} \\
&= \sqrt{\frac{2L+1}{16\pi}\frac{(L-m)!}{(L+m)!}}i\left[-P_L^{m+1}(1) - (L+m)(L-m+1)P_L^{m-1}(1)\right]. \qquad \text{(A.21)}
\end{aligned}$$

Having regard to $\frac{1}{\sin(\theta)}\frac{\partial(Y_L^m)^*}{\partial\phi} = -\frac{1}{\sin(\theta)}\frac{\partial Y_L^m}{\partial\phi}$, one can evaluate the integral

I_{Ang3} as

$$\begin{aligned}
I_{\text{Ang3}} &= \int\int \frac{1}{\sin(\theta)} \frac{1}{\sin(\theta)} \frac{\partial Y}{\partial \phi} \frac{\partial Y'^{*}}{\partial \phi}\ \delta(\theta - \theta_0)\delta(\phi - \phi_0)\ d\theta\ d\phi \\
&= \sqrt{\frac{(2L_1+1)}{16\pi} \frac{(2L_1'+1)}{16\pi} \frac{(L_1 - m_{L_1})!}{(L_1 + m_{L_1})!} \frac{(L_1' - m_{L_1}')!}{(L_1' + m_{L_1}')!}} \\
&\quad \times i \left[-P_{L_1}^{m_{L_1}+1}(1) - (L_1 + m_{L_1})(L_1 - m_{L_1} + 1) P_{L_1}^{m_{L_1}-1}(1) \right] \\
&\quad \times i \left[P_{L_1'}^{m_{L_1}'+1}(1) + (L_1' + m_{L_1}')(L_1' - m_{L_1}' + 1) P_{L_1'}^{m_{L_1}'-1}(1) \right] \\
&= \sqrt{\frac{(2L_1+1)}{16\pi} \frac{(2L_1'+1)}{16\pi} ((L_1+1)L_1)^{-m_{L_1}} ((L_1'+1)L_1')^{-m_{L_1}'}} \\
&\quad \times i \left[-\delta_{m_{L_1},-1} - (L_1 + m_{L_1})(L_1 - m_{L_1} + 1)\delta_{m_{L_1},1} \right] \\
&\quad \times i \left[\delta_{m_{L_1}',-1} + (L_1' + m_{L_1}')(L_1' - m_{L_1}' + 1)\delta_{m_{L_1}',1} \right] .
\end{aligned} \tag{A.22}$$

B

Density distribution in the trap

B.1 Ideal gas in the harmonic trap

Both the magnetic trap and the optical dipole trap used in this work, is approximated to provide harmonic confinement

$$V(x,y,z) = \frac{m}{2}(\omega_x^2 x^2 + \omega_y^2 y^2 + \omega_z^2 z^2) \tag{B.1}$$

with the trap frequencies ω_i. According to the Maxwell Boltzmann distribution, the density distribution of the cloud in the trap is then given by

$$\begin{aligned} n(x,y,z) =& n_0 \exp\left(-\frac{\frac{m}{2}(\omega_x^2 x^2 + \omega_y^2 y^2 + \omega_z^2 z^2)}{k_\mathrm{B} T}\right) \\ =& n_0 \exp\left(-\frac{x^2}{2\sigma_x^2} - \frac{y^2}{2\sigma_y^2} - \frac{z^2}{2\sigma_z^2}\right) \end{aligned} \tag{B.2}$$

with the Gaussian widths of the distribution $\sigma_i = \frac{1}{\omega_i}\sqrt{\frac{k_\mathrm{B} T}{m}}$ and the peak density n_0. The total atom number is in given by the integral over all three dimensions

$$N_{\mathrm{tot}} = \int n(x,y,z)\; dx\; dy\; dz = n_0 (2\pi)^{3/2} \sigma_x \sigma_y \sigma_z \tag{B.3}$$

which tells means in turn, that we can determine the peak density of the cloud from the atom number and trap parameters according to

$$n_0 = N_{\mathrm{tot}} \omega_x \omega_y \omega_z \left(\frac{m}{2\pi k_{\mathrm{B}} T} \right)^{3/2} . \tag{B.4}$$

B.2 BEC in the harmonic trap

Again we start with the harmonic trapping potential Eq. B.1. In the Thomas-Fermi approximation, the kinetic energy is neglected and at the rim of the condensate the potential energy equals the chemical potential μ. This tells us, that the Thomas-Fermi radii are given by $R_i = \frac{1}{\omega_i}\sqrt{\frac{2\mu}{m}}$ and we can write the density distribution as

$$n(x,y,z) = n_0 \left[1 - \frac{x^2}{R_x^2} - \frac{y^2}{R_y^2} - \frac{z^2}{R_z^2} \right] . \tag{B.5}$$

Again we receive the total atom number from integration along all three dimensions

$$\begin{aligned}
N_{\mathrm{tot}} =& \int_{-x_0}^{x_0} \int_{-y_0}^{y_0} \int_{-z_0}^{z_0} n(x,y,z)\; dx\; dy\; dz \quad \text{with } z_0 = R_z \sqrt{1 - \frac{x^2}{R_x^2} - \frac{y^2}{R_y^2}} \\
=& \frac{4}{3} n_0 R_z \int_{-x_0}^{x_0} \int_{-y_0}^{y_0} \left[1 - \frac{x^2}{R_x^2} - \frac{y^2}{R_y^2} \right]^{3/2} dx\; dy \quad \text{with } y_0 = R_y \sqrt{1 - \frac{x^2}{R_x^2}} \\
=& \frac{\pi}{2} n_0 R_y R_z \int_{-x_0}^{x_0} \left[1 - \frac{x^2}{R_x^2} \right]^2 dx \quad \text{with } x_0 = R_x \\
=& \frac{8}{15} n_0 \pi R_x R_y R_z
\end{aligned} \tag{B.6}$$

In order to be able to determine the peak density, we have to rearrange this formula further, by the use of the Thomas-Fermi radii $R_i = \frac{1}{\omega_i}\sqrt{\frac{2\mu}{m}}$ and the chemical potential $\mu = 4\pi\hbar^2 a n_0 / m$, where a is the scattering length for the particles in the cloud. It results in

$$\begin{aligned} N_{\mathrm{tot}} =& \frac{8\pi n_0}{15\omega_x\omega_y\omega_z}\left(\frac{2\mu}{m}\right)^{3/2} \\ =& \frac{(8\pi n_0)^{5/2}a^{3/2}\hbar^3}{15\omega_x\omega_y\omega_z m^3}. \end{aligned} \tag{B.7}$$

Therefore, the peak density and the chemical potential are given by

$$\begin{aligned} n_0 =& \frac{1}{8\pi}\left(\frac{15\omega_x\omega_y\omega_z m^3 N_{\mathrm{tot}}}{a^{3/2}\hbar^3}\right)^{2/5} \\ \mu =& \frac{1}{2}\left(15\omega_x\omega_y\omega_z N_{\mathrm{tot}}\sqrt{m}\hbar^2 a\right)^{2/5} \end{aligned} \tag{B.8}$$

C

Rydberg spectrum in a dense micro-BEC

C.1 Modeling the Rydberg spectrum including the spin-orbit effect in the scattering process

As mentioned in section 3.4.3, for the calculation of the PECs in the last chapter 6, the singlet scattering channels can only by neglected as long as spin-orbit interaction in the p-wave scattering channel is omitted. Including this coupling in the Fermi model in general causes further butterfly potentials that cross the S-type Born Oppenheimer curves. For our spin configuration of $m_K = 5/2$ only two of them couple with the latter (see e.g. [108] Fig. 4(c) or [107]). Moreover, the coupling of one of them is very weak. Consequently, the main effect of the spin-orbit coupling is a shift of the avoided crossing and slight modifications of the potential energy curve in its vicinity. In order to verify that spin-orbit interaction does not significantly affect our calculated spectra, the results are compared to additional calculations based on Born-Oppenheimer curves for which $l - S$ coupling is included in the p-wave channel in Fig. C.1. We acknowledge C. Fey and P. Schmelcher for providing the corresponding potential energy curves.

The spectra modeled based on the PECs including the spin-orbit coupling

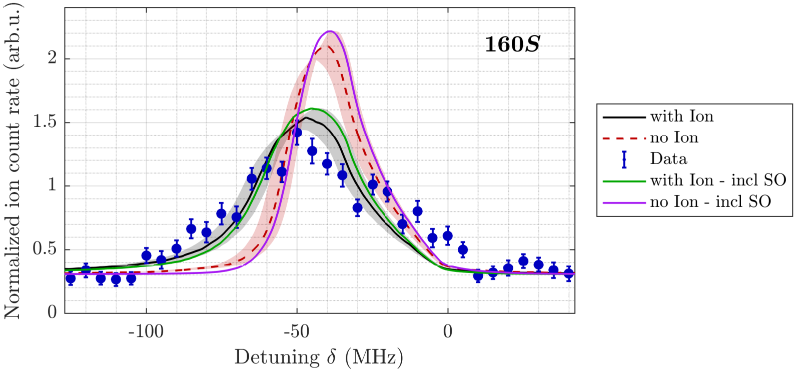

Fig. C.1: Data points, red and black curves are taken from Fig. 6.6. In addition, the result of our full numerical model is presented based on potential energy curves including spin-orbit coupling in the p-wave scattering channel with (green) and without (purple) taking the ion-atom interaction into account. Note that the effect of spin-orbit interaction is within our experimental error bars (shaded regions).

only vary within our experimental error bars but do not significantly deviate from the results of the calculation neglecting this effect.

Bibliography

[1] Kleinbach, K. S., Engel, F., Dieterle, T., Löw, R., Pfau, T. & Meinert, F. “Ionic Impurity in a Bose-Einstein Condensate at Submicrokelvin Temperatures”. Phys. Rev. Lett. **120,** 193401 (2018) (cit. on pp. 10, 17, 37, 97, 118).

[2] Kleinbach, K. S., Meinert, F., Engel, F., Kwon, W. J., Löw, R., Pfau, T. & Raithel, G. “Photoassociation of Trilobite Rydberg Molecules via Resonant Spin-Orbit Coupling”. Phys. Rev. Lett. **118,** 223001 (2017) (cit. on pp. 8, 16, 80, 117).

[3] Liebisch, T. C. *et al.* “Controlling Rydberg atom excitations in dense background gases”. J. Phys. B **49,** 182001 (2016) (cit. on p. 104).

[4] Schlagmüller, M., Liebisch, T. C., Engel, F., Kleinbach, K. S., Böttcher, F., Hermann, U., Westphal, K. M., Gaj, A., Löw, R., Hofferberth, S., Pfau, T., Pérez-Ríos, J. & Greene, C. H. “Ultracold Chemical Reactions of a Single Rydberg Atom in a Dense Gas”. Phys. Rev. X **6,** 031020 (2016) (cit. on pp. 9, 16, 71, 111, 112, 118).

[5] Böttcher, F., Gaj, A., Westphal, K. M., Schlagmüller, M., Kleinbach, K. S., Löw, R., Liebisch, T. C., Pfau, T. & Hofferberth, S. “Observation of mixed singlet-triplet Rb_2 Rydberg molecules”. Phys. Rev. A **93,** 032512 (2016) (cit. on p. 53).

[6] Schlagmüller, M., Liebisch, T. C., Nguyen, H., Lochead, G., Engel, F., Böttcher, F., Westphal, K. M., Kleinbach, K. S., Löw, R., Hofferberth, S., Pfau, T., Pérez-Ríos, J. & Greene, C. H. “Probing an Electron Scattering Resonance using Rydberg Molecules within a Dense and Ultracold Gas”. Phys. Rev. Lett. **116,** 053001 (2016) (cit. on pp. 9, 16, 102, 104).

[7] Wollaston, W. H. “A method of examining refractive and dispersive powers, by prismatic reflection”. Philosophical Transactions of the Royal Society **92,** 365 (1802) (cit. on pp. 5, 13, 20).

[8] Fraunhofer, J. “Bestimmung des Brechungs- Farbenzerstreuungs-Vermögens verschiedener Glasarten, in Bezug auf die Vervollkommnung achromatischer Fernrohre”. Denkschriften der Königlichen Akademie der Wissenschaften zu München **5,** 193 (1814) (cit. on pp. 5, 13, 20).

[9] Ångström, A. J. “Recherches sur le spectre solaire”. Upsal: W. Schultz (1868) (cit. on pp. 5, 13, 20).

[10] Bohr, N. “XXXVII. On the constitution of atoms and molecules”. Philos. Mag. **26,** 476 (1913) (cit. on pp. 5, 13, 20).

[11] Sommerfeld, A. “Zur Quantentheorie der Spektrallinien”. Ann. Phys. **356,** 1 (1916) (cit. on pp. 5, 13, 21).

[12] Löw, R., Weimer, H., Nipper, J., Balewski, J. B., Butscher, B., Büchler, H. P. & Pfau, T. “An experimental and theoretical guide to strongly interacting Rydberg gases”. J. Phys. B **45** (2012) (cit. on pp. 5, 6, 13, 14, 31).

[13] Metcalf, H. J. & van der Straten, P. *Laser Cooling and Trapping,* 323 (1999) (cit. on pp. 5, 14).

[14] Anderson, M. H., Ensher, J. R., Matthews, M. R., Wieman, C. E. & Cornell, E. A. “Observation of Bose-Einstein Condensation in a Dilute Atomic Vapor”. Science **269,** 198 (1995) (cit. on pp. 5, 14).

[15] DeMarco, B. & Jin, D. S. “Onset of Fermi degeneracy in a trapped atomic gas”. Science **285,** 1703 (1999) (cit. on pp. 5, 14).

[16] Greiner, M., Regal, C. A. & Jin, D. S. “Emergence of a molecular Bose-Einstein condensate from a Fermi gas”. Nature **426,** 537 (2003) (cit. on pp. 5, 14).

[17] Raimond, J. M., Vitrant, G. & Haroche, S. “Spectral line broadening due to the interaction between very excited atoms: ’the dense Rydberg gas’”. J. Phys. B **14,** L655 (1981) (cit. on pp. 6, 14, 31).

[18] Jaksch, D., Cirac, J. I., Zoller, P., Rolston, S. L., Côté, R. & Lukin, M. D. “Fast Quantum Gates for Neutral Atoms”. Phys. Rev. Lett. **85,** 2208 (2000) (cit. on pp. 6, 14, 31, 32).

[19] Lukin, M. D., Fleischhauer, M., Côté, R., Duan, L. M., Jaksch, D., Cirac, J. I. & Zoller, P. "Dipole Blockade and Quantum Information Processing in Mesoscopic Atomic Ensembles". Phys. Rev. Lett. **87,** 037901 (2001) (cit. on pp. 6, 14, 31, 32).

[20] Saffman, M., Walker, T. G. & Mølmer, K. "Quantum information with Rydberg atoms". Rev. Mod. Phys. **82,** 2313 (2010) (cit. on pp. 6, 14, 31, 32).

[21] Urban, E., Johnson, T. A., Henage, T., Isenhower, L., Yavuz, D. D., Walker, T. G. & Saffman, M. "Observation of Rydberg blockade between two atoms". Nat. Phys. **5,** 110 (2009) (cit. on pp. 6, 14).

[22] Tiarks, D., Schmidt, S., Rempe, G. & Dürr, S. "Optical pi phase shift created with a single-photon pulse". Sci. Adv. **2** (2016) (cit. on pp. 6, 14).

[23] Liang, Q.-Y., Venkatramani, A. V., Cantu, S. H., Nicholson, T. L., Gullans, M. J., Gorshkov, A. V., Thompson, J. D., Chin, C., Lukin, M. D. & Vuletić, V. "Observation of three-photon bound states in a quantum nonlinear medium". Science **359,** 783 (2018) (cit. on pp. 6, 14).

[24] Pritchard, J. D., Maxwell, D., Gauguet, A., Weatherill, K. J., Jones, M. P. A. & Adams, C. S. "Cooperative Atom-Light Interaction in a Blockaded Rydberg Ensemble". Phys. Rev. Lett. **105,** 193603 (2010) (cit. on pp. 6, 14, 32).

[25] Peyronel, T., Firstenberg, O., Liang, Q. Y., Hofferberth, S., Gorshkov, A. V., Pohl, T., Lukin, M. D. & Vuletić, V. "Quantum nonlinear optics with single photons enabled by strongly interacting atoms". Nature **488,** 57 (2012) (cit. on pp. 6, 14, 32).

[26] Weimer, H., Müller, M., Lesanovsky, I., Zoller, P. & Büchler, H. P. "A Rydberg quantum simulator". Nat. Phys. **6,** 382 (2010) (cit. on pp. 6, 14, 31, 32).

[27] Léséleuc, S., Weber, S., Lienhard, V., Barredo, D., Büchler, H. P., Lahaye, T. & Browaeys, A. "Accurate Mapping of Multilevel Rydberg Atoms on Interacting Spin-1/2 Particles for the Quantum Simulation of Ising Models". Phys. Rev. Lett. **120,** 113602 (2018) (cit. on pp. 6, 14, 32).

[28] Bernien, H., Schwartz, S., Keesling, A., Levine, H., Omran, A., Pichler, H., Choi, S. W., Zibrov, A. S., Endres, M., Greiner, M., Vuletić, V. & Lukin, M. D. “Probing many-body dynamics on a 51-atom quantum simulator”. Nature **551,** 579 (2017) (cit. on pp. 6, 14, 31, 32).

[29] Schauss, P., Zeiher, J., Fukuhara, T., Hild, S., Cheneau, M., Macri, T., Pohl, T., Bloch, I. & Gross, C. “Crystallization in Ising quantum magnets”. Science **347,** 1455 (2015) (cit. on pp. 6, 14).

[30] Pupillo, G., Micheli, A., Boninsegni, M., Lesanovsky, I. & Zoller, P. “Strongly Correlated Gases of Rydberg-Dressed Atoms: Quantum and Classical Dynamics”. Phys. Rev. Lett. **104,** 223002 (2010) (cit. on pp. 6, 14).

[31] Zeiher, J., van Bijnen, R., Schauss, P., Hild, S., Choi, J. Y., Pohl, T., Bloch, I. & Gross, C. “Many-body interferometry of a Rydberg-dressed spin lattice”. Nature Physics **12,** 1095 (2016) (cit. on pp. 6, 14).

[32] Sedlacek, J. A., Schwettmann, A., Kübler, H. & Shaffer, J. P. “Atom-Based Vector Microwave Electrometry Using Rubidium Rydberg Atoms in a Vapor Cell”. Phys. Rev. Lett. **111,** 063001 (2013) (cit. on pp. 6, 14).

[33] Vitrant, G., Raimond, J. M., Gross, M. & Haroche, S. “Rydberg to plasma evolution in a dense gas of very excited atoms”. J. Phys. B **15,** L49 (1982) (cit. on pp. 6, 14).

[34] Robinson, M. P., Tolra, B. L., Noel, M. W., Gallagher, T. F. & Pillet, P. “Spontaneous Evolution of Rydberg Atoms into an Ultracold Plasma”. Phys. Rev. Lett. **85,** 4466 (2000) (cit. on pp. 6, 14).

[35] Pohl, T., Pattard, T. & Rost, J. M. “Plasma formation from ultracold Rydberg gases”. Phys. Rev. A **68,** 010703 (2003) (cit. on pp. 6, 14).

[36] Greene, C. H., Dickinson, A. S. & Sadeghpour, H. R. “Creation of Polar and Nonpolar Ultra-Long-Range Rydberg Molecules”. Phys. Rev. Lett. **85,** 2458 (2000) (cit. on pp. 7, 15, 44, 48, 79).

[37] Hamilton, E. L., Greene, C. H. & Sadeghpour, H. R. “Shape-resonance-induced long-range molecular Rydberg states”. J. Phys. B **35,** L199 (2002) (cit. on pp. 7, 15, 49, 50, 122).

[38] Bendkowsky, V., Butscher, B., Nipper, J., Shaffer, J. P., Löw, R. & Pfau, T. “Observation of ultralong-range Rydberg molecules”. Nature **458,** 1005 (2009) (cit. on pp. 7, 15, 47).

[39] Bendkowsky, V., Butscher, B., Nipper, J., Balewski, J. B., Shaffer, J. P., Löw, R., Pfau, T., Li, W., Stanojevic, J., Pohl, T. & Rost, J. M. “Rydberg Trimers and Excited Dimers Bound by Internal Quantum Reflection”. Phys. Rev. Lett. **105,** 163201 (2010) (cit. on pp. 7, 15, 47).

[40] Gaj, A., Krupp, A. T., Balewski, J. B., Löw, R., Hofferberth, S. & Pfau, T. “From molecular spectra to a density shift in dense Rydberg gases”. Nat. Comm. **5,** 4546 (2014) (cit. on pp. 7, 15, 46, 47).

[41] Li, W., Pohl, T., Rost, J. M., Rittenhouse, S. T., Sadeghpour, H. R., Nipper, J., Butscher, B., Balewski, J. B., Bendkowsky, V., Löw, R. & Pfau, T. “A Homonuclear Molecule with a Permanent Electric Dipole Moment”. Science **334,** 1110 (2011) (cit. on pp. 7, 15, 48, 92).

[42] Booth, D., Rittenhouse, S. T., Yang, J., Sadeghpour, H. R. & Shaffer, J. P. “Production of trilobite Rydberg molecule dimers with kilo-Debye permanent electric dipole moments”. Science **348,** 99 (2015) (cit. on pp. 7, 8, 15, 16, 48, 80).

[43] Niederprüm, T., Thomas, O., Eichert, T., Lippe, C., Pérez-Ríos, J., Greene, C. H. & Ott, H. “Observation of pendular butterfly Rydberg molecules”. Nat. Comm. **7,** 12820 (2016) (cit. on pp. 7, 15, 50).

[44] Anderson, D. A., Miller, S. A. & Raithel, G. “Photoassociation of Long-Range nD Rydberg Molecules”. Phys. Rev. Lett. **112,** 163201 (2014) (cit. on pp. 7, 15, 47, 53).

[45] Sassmannshausen, H., Merkt, F. & Deiglmayr, J. “Experimental Characterization of Singlet Scattering Channels in Long-Range Rydberg Molecules”. Phys. Rev. Lett. **114,** 133201 (2015) (cit. on pp. 7, 15, 47, 53).

[46] Gaj, A., Krupp, A. T., Ilzhöfer, P., Löw, R., Hofferberth, S. & Pfau, T. “Hybridization of Rydberg Electron Orbitals by Molecule Formation”. Phys. Rev. Lett. **115,** 023001 (2015) (cit. on pp. 7, 15).

[47] Niederprüm, T., Thomas, O., Eichert, T. & Ott, H. “Rydberg Molecule-Induced Remote Spin Flips”. Phys. Rev. Lett. **117,** 123002 (2016) (cit. on pp. 7, 15, 47, 53, 89).

[48] Oliver, T., Lippe, C., Eichert, T. & Ott, H. “Experimental realization of a Rydberg optical Feshbach resonance in a quantum many-body system”. arXiv:1712.05263 (2017) (2017) (cit. on pp. 7, 15, 54).

[49] Schmidt, R., Sadeghpour, H. R. & Demler, E. “Mesoscopic Rydberg Impurity in an Atomic Quantum Gas”. Phys. Rev. Lett. **116,** 105302 (2016) (cit. on pp. 8, 9, 15, 16, 104, 106, 118).

[50] Schmidt, R. & Lemeshko, M. “Deformation of a Quantum Many-Particle System by a Rotating Impurity”. Phys. Rev. X **6,** 011012 (2016) (cit. on pp. 8, 15, 118).

[51] Eiles, M. T., Lee, H., Pérez-Ríos, J. & Greene, C. H. “Anisotropic blockade using pendular long-range Rydberg molecules”. Phys. Rev. A **95,** 052708 (2017) (cit. on pp. 8, 15, 118).

[52] Luukko, P. J. J. & Rost, J. M. “Polyatomic Trilobite Rydberg Molecules in a Dense Random Gas”. Phys. Rev. Lett. **119,** 203001 (2017) (cit. on pp. 8, 15).

[53] Amaldi, E. & Segrè, E. “Effect of pressure on high terms of alkaline spectra”. Nature **133,** 141 (1934) (cit. on pp. 8, 16, 40).

[54] Füchtbauer, C. & Gössler, F. “Shift and asymmetrical broadening of absorption lines by foreign gases”. Z. Phys. **87,** 89 (1934) (cit. on pp. 8, 16, 40).

[55] Fermi, E. “Sopra lo spostamento per pressione delle righe elevate delle serie spettrali”. Nuovo Cimento **11** (1934) (cit. on pp. 8, 16, 40, 43).

[56] Balewski, J. B., Krupp, A. T., Gaj, A., Peter, D., Büchler, H. P., Löw, R., Hofferberth, S. & Pfau, T. “Coupling a single electron to a Bose-Einstein condensate”. Nature **502,** 664 (2013) (cit. on pp. 9, 16, 104, 105).

[57] Camargo, F., Schmidt, R., Whalen, J. D., Ding, R., Woehl, G., Yoshida, S., Burgdörfer, J., Dunning, F. B., Sadeghpour, H. R., Demler, E. & Killian, T. C. “Creation of Rydberg Polarons in a Bose Gas”. Phys. Rev. Lett. **120,** 083401 (2018) (cit. on pp. 9, 16, 104).

[58] Idziaszek, Z., Calarco, T., Julienne, P. S. & Simoni, A. “Quantum theory of ultracold atom-ion collisions”. Phys. Rev. A **79,** 010702 (2009) (cit. on pp. 9, 17, 118).

[59] Schmid, T., Veit, C., Zuber, N., Löw, R., Pfau, T., Tarana, M. & Tomza, M. “Rydberg Molecules for Ion-Atom Scattering in the Ultracold Regime”. Phys. Rev. Lett. **120,** 153401 (2018) (cit. on pp. 9, 17, 118, 119).

[60] Chin, C., Grimm, R., Julienne, P. & Tiesinga, E. “Feshbach resonances in ultracold gases”. Rev. Mod. Phys. **82,** 1225 (2010) (cit. on pp. 9, 17, 118).

[61] Grier, A. T., Cetina, M., Orucevic, F. & Vuletić, V. “Observation of Cold Collisions between Trapped Ions and Trapped Atoms”. Phys. Rev. Lett **102,** 223201 (2009) (cit. on pp. 9, 10, 17, 97, 118).

[62] Jachymski, K., Krych, M., Julienne, P. S. & Idziaszek, Z. “Quantum Theory of Reactive Collisions for $1/r^n$ Potentials”. Phys. Rev. Lett. **110,** 213202 (2013) (cit. on pp. 9, 17, 118).

[63] Hall, F. H. J., Eberle, P., Hegi, G., Raoult, M., Aymar, M., Dulieu, O. & Willitsch, S. “Ion-neutral chemistry at ultralow energies: dynamics of reactive collisions between laser-cooled Ca+ ions and Rb atoms in an ion-atom hybrid trap”. Mol. Phys. **111,** 2020 (2013) (cit. on pp. 9, 17, 118).

[64] Ratschbacher, L., Zipkes, C., Sias, C. & Köhl, M. “Controlling chemical reactions of a single particle”. Nat. Phys. **8,** 649 (2012) (cit. on pp. 9, 10, 17, 97, 118).

[65] Côté, R., Kharchenko, V. & Lukin, M. D. “Mesoscopic Molecular Ions in Bose-Einstein Condensates”. Phys. Rev. Lett. **89,** 093001 (2002) (cit. on pp. 9, 17, 37, 118).

[66] Schurer, J. M., Negretti, A. & Schmelcher, P. “Unraveling the Structure of Ultracold Mesoscopic Collinear Molecular Ions”. Phys. Rev. Lett. **119,** 063001 (2017) (cit. on pp. 9, 17, 118).

[67] Casteels, W., Tempere, J. & Devreese, J. T. “Polaronic Properties of an Ion in a Bose-Einstein Condensate in the Strong-Coupling Limit”. J. Low Temp. Phys. **162,** 266 (2011) (cit. on pp. 9, 17, 118).

[68] Doerk, H., Idziaszek, Z. & Calarco, T. “Atom-ion quantum gate”. Phys. Rev. A **81,** 012708 (2010) (cit. on pp. 9, 17, 118).

[69] Gerritsma, R., Negretti, A., Doerk, H., Idziaszek, Z., Calarco, T. & Schmidt-Kaler, F. “Bosonic Josephson Junction Controlled by a Single Trapped Ion”. Phys. Rev. Lett. **109,** 080402 (2012) (cit. on pp. 9, 17, 118).

[70] Bissbort, U., Cocks, D., Negretti, A., Idziaszek, Z., Calarco, T., Schmidt-Kaler, F., Hofstetter, W. & Gerritsma, R. “Emulating Solid-State Physics with a Hybrid System of Ultracold Ions and Atoms”. Phys. Rev. Lett. **111,** 080501 (2013) (cit. on pp. 9, 17, 118).

[71] Krükow, A., Mohammadi, A., Härter, A., Hecker Denschlag, J., Pérez-Ríos, J. & Greene, C. H. "Energy Scaling of Cold Atom-Atom-Ion Three-Body Recombination". Phys. Rev. Lett. **116,** 193201 (2016) (cit. on pp. 10, 17, 97, 118).

[72] Hall, F. H. J. & Willitsch, S. "Millikelvin Reactive Collisions between Sympathetically Cooled Molecular Ions and Laser-Cooled Atoms in an Ion-Atom Hybrid Trap". Phys. Rev. Lett. **109,** 233202 (2012) (cit. on pp. 10, 17, 97, 118).

[73] Zipkes, C., Palzer, S., Sias, C. & Köhl, M. "A trapped single ion inside a Bose-Einstein condensate". Nature **464,** 388 (2010) (cit. on pp. 10, 17, 97, 118).

[74] Cetina, M., Grier, A. T. & Vuletić, V. "Micromotion-Induced Limit to Atom-Ion Sympathetic Cooling in Paul Traps". Phys. Rev. Lett. **109,** 253201 (2012) (cit. on pp. 10, 17, 97).

[75] Schneider, C., Enderlein, M., Huber, T. & Schaetz, T. "Optical trapping of an ion". Nat. Phot. **4,** 772 (2010) (cit. on pp. 10, 17, 97).

[76] Lambrecht, A., Schmidt, J., Weckesser, P., Debatin, M., Karpa, L. & Schaetz, T. "Long lifetimes and effective isolation of ions in optical and electrostatic traps". Nat. Phot. **11,** 704 (2017) (cit. on pp. 10, 17, 97).

[77] Balmer, J. J. "Notiz über die Spectrallinien des Wasserstoffs". Ann. Phys. **25,** 80 (1885) (cit. on p. 20).

[78] Rydberg, J. R. "On the structure of the line spectra of the chemical elements". Philos. Mag. **29,** 331 (1890) (cit. on p. 20).

[79] Steck, D. A. "Rubidium 87 D Line Data (revision 2.1.5)" (2015) (cit. on pp. 21, 22, 30, 74, 77).

[80] Mack, M., Karlewski, F., Hattermann, H., Höckh, S., Jessen, F., Cano, D. & Fortágh, J. "Measurement of absolute transition frequencies of ^{87}Rb to nS and nD Rydberg states by means of electromagnetically induced transparency". Phys. Rev. A **83,** 052515 (2011) (cit. on pp. 22, 23).

[81] Li, W., Mourachko, I., Noel, M. W. & Gallagher, T. F. "Millimeter-wave spectroscopy of cold Rb Rydberg atoms in a magneto-optical trap: Quantum defects of the ns, np, and nd series". Phys. Rev. A **67,** 052502 (2003) (cit. on pp. 22, 23).

[82] Han, J., Jamil, Y., Norum, D. V. L., Tanner, P. J. & Gallagher, T. F. “Rb nf quantum defects from millimeter-wave spectroscopy of cold ^{85}Rb Rydberg atoms”. Phys. Rev. A **74,** 054502 (2006) (cit. on pp. 22, 23).

[83] Civiš, S., Ferus, M., Kubelík, P., Chernov, V. E. & Zanozina, E. M. “Fourier transform infrared emission spectra of atomic rubidium: G- and h-states”. J. Phys. B **45** (2012) (cit. on p. 22).

[84] Sansonetti, J. E. “Wavelengths, transition probabilities, and energy levels for the spectra of rubidium (Rb i through Rb XXXVII)”. J. Phys. Chem. Ref. Data **35,** 301 (2006) (cit. on p. 22).

[85] Saffman, M. “Atomic physics: structure, interactions, and entanglement (revision December 12,2017)” (2016) (cit. on pp. 23, 24).

[86] Gallagher, T. F. “Rydberg Atoms”. *Cambridge Monographs on Atomic, Molecular and Chemical Physics* (1994) (cit. on pp. 23, 25, 29, 30, 111).

[87] Marinescu, M., Sadeghpour, H. R. & Dalgarno, A. “Dispersion coefficients for alkali-metal dimers”. Phys. Rev. A **49,** 982 (1994) (cit. on pp. 23, 25).

[88] Cohen-Tannoudji, C., Diu, B. & Laloë, F. *Quantum Mechanics Vol. II,* 613 (1994) (cit. on pp. 24, 34, 36).

[89] Zimmerman, M. L., Littman, M. G., Kash, M. M. & Kleppner, D. “Stark structure of the Rydberg states of alkali-metal atoms”. Phys. Rev. A **20,** 2251 (1979) (cit. on p. 25).

[90] Browaeys, A., Barredo, D. & Lahaye, T. “Experimental investigations of dipole-dipole interactions between a few Rydberg atoms”. J. Phys. B **49** (2016) (cit. on p. 31).

[91] Boisseau, C., Simbotin, I. & Côté, R. “Macrodimers: Ultralong Range Rydberg Molecules”. Phys. Rev. Lett. **88,** 133004 (2002) (cit. on p. 32).

[92] Walker, T. G. & Saffman, M. “Zeros of Rydberg-Rydberg Föster interactions”. J. Phys. B **38,** S309 (2005) (cit. on p. 32).

[93] Niederprüm, T. “Rydberg-ground state interaction in ultracold quantum gases”. PhD Thesis, Universität Kaiserslautern (2016) (cit. on pp. 34, 127, 128).

[94] Sakurai, J. J. “Modern Quantum Mechanics, Revised Edition”. Am. J. Phys. **63,** 93 (1995) (cit. on pp. 34, 36).

[95] Crubellier, A. & Luc-Koenig, E. “Threshold effects in the photoassociation of cold atoms: R^{-6} model in the Milne formalism”. J. Phys. B **39,** 1417 (2006) (cit. on p. 36).

[96] Holmgren, W. F., Revelle, M. C., Lonij, V. P. A. & Cronin, A. D. “Absolute and ratio measurements of the polarizability of Na, K, and Rb with an atom interferometer”. Phys. Rev. A **81,** 053607 (2010) (cit. on p. 37).

[97] Jraij, A., Allouche, A. R., Korek, M. & Aubert-Frécon, M. “Theoretical electronic structure of the alkali-dimer cation Rb_2^+”. Chemical Physics **290,** 129 (2003) (cit. on p. 38).

[98] Fabrikant, I. I. “Interaction of Rydberg atoms and thermal electrons with K, Rb and Cs atoms”. J. Phys. B **19,** 1527 (1986) (cit. on pp. 42, 57).

[99] Smith, K. “Resonant scattering of electrons by atomic systems”. Rep. Prog. Phys. **29,** 373 (1966) (cit. on p. 42).

[100] Omont, A. “Theory of collisions of atome in Rydberg states with neutral particles”. Journal de Physique **38,** 1343 (1977) (cit. on pp. 43, 49).

[101] Bahrim, C., Thumm, U. & Fabrikant, I. I. “^3S_e and ^1S_e scattering lengths for $e^- +$ Rb, Cs and Fr collisions”. J. Phys. B **34,** L195 (2001) (cit. on p. 43).

[102] Tallant, J., Rittenhouse, S. T., Booth, D., Sadeghpour, H. R. & Shaffer, J. P. “Observation of Blueshifted Ultralong-Range Cs_2 Rydberg Molecules”. Phys. Rev. Lett. **109,** 173202 (2012) (cit. on p. 47).

[103] Krupp, A. T., Gaj, A., Balewski, J. B., Ilzhöfer, P., Hofferberth, S., Löw, R., Pfau, T., Kurz, M. & Schmelcher, P. “Alignment of *D*-State Rydberg Molecules”. Phys. Rev. Lett. **112,** 143008 (2014) (cit. on p. 47).

[104] DeSalvo, B. J., Aman, J. A., Dunning, F. B., Killian, T. C., Sadeghpour, H. R., Yoshida, S. & Burgdörfer, J. “Ultra-long-range Rydberg molecules in a divalent atomic system”. Phys. Rev. A **92,** 031403 (2015) (cit. on p. 47).

[105] Bellos, M. A., Carollo, R., Banerjee, J., Eyler, E. E., Gould, P. L. & Stwalley, W. C. “Excitation of Weakly Bound Molecules to Trilobite-like Rydberg States”. Phys. Rev. Lett. **111,** 053001 (2013) (cit. on p. 47).

[106] Kurz, M. “Ultralong-range Diatomic Molecules in External Electric and Magnetic Fields”. PhD Thesis, Universität Hamburg (2014) (cit. on pp. 48, 121).

[107] Markson, S., Rittenhouse, S. T., Schmidt, R., Shaffer, J. P. & Sadeghpour, H. R. “Theory of Ultralong-Range Rydberg Molecule Formation Incorporating Spin-Dependent Relativistic Effects: Cs(6s)-Cs(np) as Case Study”. ChemPhysChem **17,** 3683 (2016) (cit. on pp. 53, 109, 117, 135).

[108] Eiles, M. T. & Greene, C. H. “Hamiltonian for the inclusion of spin effects in long-range Rydberg molecules”. Phys. Rev. A **95,** 042515 (2017) (cit. on pp. 53, 56, 109, 117, 135).

[109] Fey, C., Kurz, M., Schmelcher, P., Rittenhouse, S. T. & Sadeghpour, H. R. “A comparative analysis of binding in ultralong-range Rydberg molecules”. New J. Phys. **17,** 055010 (2015) (cit. on p. 55).

[110] Schlagmüller, M. “A single Rydberg Atom interacting with a Dense and Ultracold Gas”. PhD Thesis, Universität Stuttgart (2016) (cit. on pp. 60, 64, 102, 111).

[111] Jennewein, S. “Building an Apparatus for Cold Rubidium Rydberg Atoms”. Diploma Thesis, Universität Stuttgart (2012) (cit. on p. 60).

[112] Tresp, C. “A Setup for Highly Precise Excitation and Detection of Rydberg Atoms”. Master Thesis, Universität Stuttgart (2012) (cit. on p. 60).

[113] Schmid, T. “High precision excitation, manipulation and detection of Rydberg atoms”. Master Thesis, Universität Stuttgart (2014) (cit. on pp. 60, 76).

[114] Böttcher, F. “Rydberg Molecules Bound By Mixed Singlet-Triplet Scattering”. Master Thesis, Universität Stuttgart (2015) (cit. on p. 60).

[115] Engel, F. “Ultracold chemistry of a Rydberg atom in a rubidium-87 BEC”. Master Thesis, Universität Stuttgart (2016) (cit. on pp. 60, 102).

[116] Black, E. D. “An introduction to Pound-Drever-Hall laser frequency stabilization”. Am. J. Phys. **69,** 79 (2001) (cit. on pp. 63, 68, 69).

[117] Drever, R. W. P., Hall, J. L., Kowalski, F. V., Hough, J., Ford, G. M., Munley, A. J. & Ward, H. “Laser phase and frequency stabilization using an optical resonator”. Appl. Phys. B-Photo **31,** 97 (1983) (cit. on pp. 63, 68, 69).

[118] Grimm, R., Weidemüller, M. & Ovchinnikov, Y. B. “Optical dipole traps for neutral atoms”. *Advances In Atomic Molecular and Optical Physics* **42,** 95 (2000) (cit. on p. 65).

[119] Safronova, M. S., Williams, C. J. & Clark, C. W. “Relativistic many-body calculations of electric-dipole matrix elements, lifetimes, and polarizabilities in rubidium”. Phys. Rev. A **69,** 022509 (2004) (cit. on p. 68).

[120] Ketterle, W., Durfee, D. S. & Stamper-Kurn, D. M. “Making, probing and understanding Bose-Einstein condensates”. arXiv:9904034 (1999) (cit. on p. 76).

[121] Sikorsky, T., Meir, Z., Ben-shlomi, R., Akerman, N. & Ozeri, R. “Spin-controlled atom-ion chemistry”. Nat. Comm. **9** (2018) (cit. on pp. 97, 118).

[122] Tomza, M., Koch, C. P. & Moszynski, R. “Cold interactions between an Yb^+ ion and a Li atom: Prospects for sympathetic cooling, radiative association, and Feshbach resonances”. Phys. Rev. A **91,** 042706 (2015) (cit. on p. 97).

[123] Joger, J., Fürst, H., Ewald, N., Feldker, T., Tomza, M. & Gerritsma, R. “Observation of collisions between cold Li atoms and Yb^+ ions”. Phys. Rev. A **96,** 030703 (2017) (cit. on p. 97).

[124] Meir, Z., Sikorsky, T., Ben-Shlomi, R., Akerman, N., Dallal, Y. & Ozeri, R. “Dynamics of a Ground-State Cooled Ion Colliding with Ultracold Atoms”. Phys. Rev. Lett. **117,** 243401 (2016) (cit. on p. 98).

[125] Härter, A., Krükow, A., Brunner, A., Schnitzler, W., Schmid, S. & Hecker Denschlag, J. “Single Ion as a Three-Body Reaction Center in an Ultracold Atomic Gas”. Phys. Rev. Lett. **109,** 123201 (2012) (cit. on p. 98).

[126] Wikipedia. *Retrieved May 02, 2018 from https://en.wikipedia.org/wiki/Complete_spatial_randomness* (cit. on p. 100).

[127] Schmidt, R., Whalen, J. D., Ding, R., Camargo, F., Woehl, G., Yoshida, S., Burgdörfer, J., Dunning, F. B., Demler, E., Sadeghpour, H. R. & Killian, T. C. “Theory of excitation of Rydberg polarons in an atomic quantum gas”. Phys. Rev. A **97,** 022707 (2018) (cit. on p. 104).

[128] Schmidt, R. “private communication” (2018) (cit. on p. 104).

[129] Ryabtsev, I. I., Beterov, I. I., Tretyakov, D. B., Entin, V. M. & Yakshina, E. A. "Doppler- and recoil-free laser excitation of Rydberg states via three-photon transitions". Phys. Rev. A **84,** 053409 (2011) (cit. on p. 119).

[130] Dunning, F. B., Reinhold, C. O., Yoshida, S. & Burgdörfer, J. "Steering quantum states toward classical Bohr-like orbits". Am. J. Phys. **78,** 796 (2010) (cit. on p. 119).

[131] Anderson, D. A., Schwarzkopf, A., Sapiro, R. E. & Raithel, G. "Production and trapping of cold circular Rydberg atoms". Phys. Rev. A **88,** 031401 (2013) (cit. on p. 119).

[132] Signoles, A., Dietsche, E. K., Facon, A., Grosso, D., Haroche, S., Raimond, J. M., Brune, M. & Gleyzes, S. "Coherent Transfer between Low-Angular-Momentum and Circular Rydberg States". Phys. Rev. Lett. **118,** 253603 (2017) (cit. on p. 119).

[133] Anderson, S. E., Younge, K. C. & Raithel, G. "Trapping Rydberg Atoms in an Optical Lattice". Phys. Rev. Lett. **107,** 263001 (2011) (cit. on p. 119).

[134] Wikipedia. *Retrieved April 13, 2018 from https://en.wikipedia.org/wiki/Clebsch%E2%80%93Gordan_coefficients#Special_cases* (cit. on p. 124).

Danksagung

Zuletzt möchte ich allen, die mich bei meiner Doktorarbeit unterstützt haben, herzlich danken! An ersten Stelle geht mein Dank an Prof. Tilman Pfau. Seitdem ich am PI5 arbeiten durfte, habe ich in zahlreichen Diskussionen und Meetings extrem viel von dir gelernt. Danke für die vielen wissenschaftlichen Ideen, die spürbare Begeisterung für die Physik und den Überblick. Danke aber auch dafür, dass dein Weg zwischen enger Betreuung der Doktorarbeit und der Freiheit für uns Dinge auszuprobieren zu einem so konzentrierten, produktiven und dabei angenehmen Arbeitsklima führt und sich durch die gute finanzielle Ausstattung des Instituts viele Möglichkeiten bieten.

Danke auch an Prof. Georg Raithel für die gute und erfolgreiche Zusammenarbeit beim Trilobite-Projekt. Des Weiteren möchte ich Prof. Peter Michler dafür danken, dass Sie den Mitbericht für meine Doktorarbeit übernehmen. Danke an Prof. Maria Daghofer für den Prüfungsvorsitz bei meiner Doktorprüfung.

Ein großer Dank geht an Robert, ohne den ich vielleicht nie am Institut gelandet wäre und von dem ich viel lernen durfte. Viele deiner “verrückten Einfälle” haben sich im Nachhinein doch als geniale Ideen erwiesen und unser Experiment voran gebracht. Danke auch an Sebastian für die fundierten Antworten auf meine zahlreichen Fragen, egal ob es um Rydberg-Physik, Matlab, Laser, Elektronik oder Vakuum ging.

Ein riesiges Dankeschön geht an das Team, mit dem ich die letzten beiden Jahre zusammenarbeiten durfte! Felix, ohne den der Umbau des Experiments nicht gelungen wäre und der unglaublich viel Energie in die Simulationen gesteckt hat. Danke, für die gute und produktive Zeit und die Unterstützung. Florian, dessen Begeisterungsfähigkeit und breites Wissen in Theorie und Labor unser Experiment weit voran gebracht haben. Danke, für die tolle

Unterstützung, die guten Diskussionen und das geduldige Korrekturlesen. Woo Jin, der viel mit den instabilen E-feldern gekämpft hat. Thomas, der sich super schnell ins Experiment eingearbeitet hat und Teile dieser Arbeit korrekturgelesen hat. Danke auch an unsere Masterstudenten Ai'Lan und Marian, die unser Team toll ergänzen. Ich wünsche euch allen noch viele spannende experimentelle Ergebnisse, neue wissenschaftliche Ideen und dass die Maschine noch lange und robust weiterläuft!

Natürlich geht ein großes Danke an alle, die mir geholfen haben, das Experiment kennen und verstehen zu lernen: Michael, von dem ich sehr viel Programmieren und so einiges über Elektronik gelernt habe. Die Experimentsteuerung mit Datenbank und Auswertesystem ist super und die Elektronikboxen werden noch einige Doktoranden zu schätzen wissen. Tara, Graham und Huan die mir den experimentellen Aufbau erklärt haben. Karl und Fabian, die viele Stunden mit mir im Labor verbracht haben, um gegen die technischen Probleme der Maschine zu kämpfen. Christoph, von dem ich vieles über Laser und Optik gelernt habe. Anita, für die Diskussionen über Rydbergmoleküle und die gemeinsame Zeit im Labor. Danke an Thomas, Stefan, Udo und alle anderen die zum Aufbau des Experiments beigetragen haben.

Ein großes Dankeschön geht an das gesamte PI5. Ich hatte eine gute Zeit am Institut und werde noch oft daran zurückdenken. Danke für die gute Atmosphäre und die Hilfsbereitschaft. Ganz besonders möchte ich dabei unseren Computeradministratoren Harald, Daniel und Nico danken. Ich habe vieles von euch gelernt und ich bin mir sicher, dass ohne euch hier Chaos ausbrechen würde. Genauso darf ich Astrid, Karin, Kati, Britta, Karin H., Oli und Nadine dafür danken, dass ihr uns so viel Verwaltungsarbeit abnehmt. Egal, ob die Abrechnung für ein teures Laborgerät das auf Ebay ersteigert wurde oder eine aufwändige Reisekostenabrechnung anstand - ihr wusstet immer einen Weg.

Danke an meine Familie, die von Anfang an meine Begeisterung für Wissenschaft und Technik gefördert hat. Und zuletzt geht ein riesiges Dankeschön an meinen Freund David, der alle Höhen und Tiefen dieser Doktorarbeit mitgemacht hat. Vielen, vielen Dank für deine Unterstützung und dein Verständnis!